# Fabrication of Carbon Nanotube Thin Films by Evaporation-Induced Self-Assembly

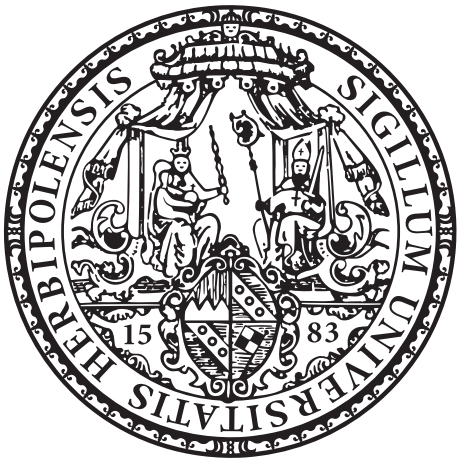


Dissertation zur Erlangung des naturwissenschaftlichen Doktorgrades
der
Julius-Maximilians-Universität Würzburg

vorgelegt von **Han Li**

Würzburg, 2015

Eingereicht bei der Fakultät für Chemie und Pharmazie am

.....

Gutachter der schriftlichen Arbeit

1. Gutachter:.....

2. Gutachter:.....

Prüfer des öffentlichen Promotionskolloquiums

1. Prüfer:.....

2. Prüfer:.....

3. Prüfer:.....

Datum des öffentlichen Promotionskolloquiums

.....

Doktorurkunde ausgehändigt am

.....

# Contents

# Acronyms

| | |
|---|---|
| 1D | one-dimensional |
| 2D | two-dimensional |
| 3D | three-dimensional |
| AFM | Atomic Force Microscope |
| CCD | Charge-Coupled Device |
| CL | Contact Line |
| CMC | Critical Micelle Concentration |
| CVD | Chemical Vapor Deposition |
| DFES | Dose-controlled Floating Evaporative Self-assembly |
| DGU | Density Gradient Ultracentrifugation |
| DOC | Sodium Deoxycholate |
| DOS | Density Of States |
| EET | Exciton Energy Transfer |
| EISA | Evaporation-Induced Self-Assembly |
| eV | electron Volt |
| fps | frames per second |
| FWHM | Full Width at Half Maximum |

| | |
|---|---|
| HMDS | Hexamethyldislizane |
| HPLC | High Performance Liquid Chromatography |
| InGaAs | Indium Gallium Arsenide |
| MWNTs | Multi-Wall Carbon Nanotubes |
| OD | Optical Density |
| PDMS | Polydimethylsiloxane |
| PFO | poly[(9,9-dioctylfluorenyl-2,7-diyl)] |
| PFO-BPy | poly[(9,9-dioctylfluorenyl-2,7-diyl)-alt-co-(6,6'-2,2'-bipyridine)] |
| PL | Photoluminescence |
| PLE | Photoluminescence Excitation |
| rpm | rounds per minute |
| SC | Sodium Cholate |
| SDS | Sodium Dodecyl Sulfate |
| SEM | Scanning Electron Microscope |
| SWNTs | Single-Wall Carbon Nanotubes |
| VTE | Vacuum Thermal Evaporation |

# 1 Introduction

In the last two decades, carbon nanotubes as an newly discovered allotrope of carbon with a cylindrical structure have attracted enormous interests in nanoscience and nanotechnology [1]. The structure of nanotubes can be considered as hollow cylindrical tubes with the walls rolled by sheets of graphene, a one-atom-thick layer of carbon in a hexagonal lattice. The number of graphene sheets defines two main categories of nanotubes, Single-Wall Carbon Nanotubes (SWNTs) with only single layer and Multi-Wall Carbon Nanotubes (MWNTs) with multilayer graphene. SWNTs, with their unique structures, show chirality-dependent electronic and vibrational properties. By changing the width and direction of the rolled-up graphene ribbons, SWNTs can be either metallic with a extremely high current-carrying capacity [2], or semiconducting with intrinsically direct bandgap [3]. Therefore, SWNTs offer potential for building a unified electronic and optoelectronic technology based on the same material. Moreover, the quasi-one-dimensional (1D) nature of nanotubes provides a unique model system to study basic optical and optoelectronic phenomena [4, 5].

Although SWNTs on a single nanostructure level have been theoretically and experimentally proved as one of the leading candidates to replace conventional semiconductors in future optoelectronic devices, as well as chemical sensors, photovoltaics and integrated circuits [6–10], implementing this exceptional material in large-area, functional and high-performance applications involving thin films or networks still has been difficult.

The first challenge comes from the purification and separation. Generally, the large scale production of SWNTs from the most promising method Chemical Vapor Deposition (CVD) always contains both metallic (m-) and semiconducting (s-) ones, with a ratio of 1:2, which will dramatically decrease the performance of SWNT devices [11]. Numerous efforts have been made on the one-step *in-situ* CVD growth for pure metallic or semiconducting tubes arrays. Even though there have been several strategies to improve the purification of s-SWNTs or m-SWNTs by altering the CVD conditions such as carbon feeds, catalysts, heating control and hydrogen ratio [12–14], the enrichment of s-SWNTs or m-SWNTs could only reach 80%-90% and the

mechanism is still ambiguous in most of cases. The semiconducting/metallic selective growth at present needs more investigation, not to mention the lack of breakthrough of the chirality control which is basically the ultimate target of structure controlled synthesis of SWNTs [11]. Fortunately a number of post-synthetic sorting methods have also been developed to separate s- and m-SWNTs and they are even able to selectively enrich one specific species [15]. Among them the first efficient and scalable method is Density Gradient Ultracentrifugation (DGU) by which the SWNTs are first dispersed in a mix of surfactants or DNA via sonication [16, 17]. The separation relies on the different buoyant densities of the SWNTs with various diameters which are highly sensitive to their chirality and semiconductivity [18]. With iterative application of the DGU technique, purities of semiconducting tubes approaching 99% have been achieved [19]. On the other hand, a more recent approach used conjugated polymers in organic solvents could effectively disperse and select semiconducting SWNTs with single chirality [20]. The specific species is selectively wrapped by the polymer chains to maximize the $\pi - \pi$ electron interaction between the polymer backbone and the nanotubes. After the sonication for sufficient debundling, a benchtop centrifuge then can easily and quickly separate the well-dispersed single species. On the basis of these predominant techniques of dispersion and purification, it is now possible to realize the full potential of thin film carbon nanotube devices that can be directly prepared from the suspensions.

The following challenge now is to design a bottom-up processing method by which SWNTs can be deposited via the solvent evaporation. Moreover, the solution-based processing technique should be able to provide controlled morphology. A well-ordered structure is very important for the device performance because the morphological defects and misalignment can block the ideally intrinsic properties like charge transport and thermal conductivity [21]. For that purpose, a fundamental technique called Evaporation-Induced Self-Assembly (EISA) has been presented and summarized as an extremely cost-effective and non-lithographic route to produce various two-dimensional (2D) structures with sorts of starting materials [22–26]. As for the near ambient conditions, or even commonly in daily life, a so-called "coffee ring effect" is one of the typical mundane phenomena with the EISA process. When a droplet coffee has dried on a table or some remaining sediment has deposited on the inner wall of a mug, the coffee solutes likely form a ring pattern rather than a homogeneous film. The mechanism of this common phenomenon with a sessile droplet model was first proposed by Deegan *et.al.* [27] who found that the suspended solutes were carried by a capillary flow towards the edge

of droplet due to the fact that the evaporative flux at the three-phase contract line (CL) is much larger than the top of the droplet. This flow-assisted self-assembly is able to produce homogeneous crystallization of different materials from meso-, nanoscale particles to molecules [28–30]. More interestingly the pinning and depinning motion of CL can be used to effectively control deposited regions [31]. Following this general strategy, several methods have been designed and adapted to produce thin films, networks or patterns of SWNTs [32–35].

Although solution processing has been hailed as a more industrially relevant route for the deposition of SWNTs in devices, the quality and performance of solution-deposited thin films have not been able to reach that of *in situ* grown SWNTs until recently [33, 36, 37]. However, the most methods at present are either too complicated to be scalable or too inefficient for the large-area fabrication. Furthermore, unlike normal mono-solute suspensions, SWNT colloids inevitably contain the surfactants or polymers as dispersants. Fundamental understanding of the physical principles underlying the process is to some extent ambiguous, especially in the relatively complicated system of SWNT colloids.

Based on the discussion above, this thesis includes two main aspects of research: the development of new methods that can effectively control the morphology of SWNT thin films as well as the fundamental understanding of the underlying mechanism. Additionally some optical properties of these patterns are preliminarily examined for the possible applications afterward.

The thesis starts with a review on several EISA-based techniques whose advantages and disadvantages are presented with specific examples respectively. After some fundamental concepts of self-assembly, we introduce a well-known theoretical model that is previously reported to describe the EISA process. The limitation of the simple model leads to our arguments some of which has already been mentioned before [38]. In the end of the chapter, a few basics of carbon nanotubes are introduced, especially in terms of the research concerning on self-assembly.

Chapter 3 provides all the experimental details including preparation of SWNT suspensions by DGU and polymer-sorting process, adapted or home-built fabrication setups, sorts of characterizations and data processing. Using the stable and thin liquid meniscus called capillary bridge [39], we produce a scalable two-plate setup which is suitable to implement and observe the EISA process with relatively high but controllable rates in room temperature. Based on the simple structure, a more sophisticated setup is built to precisely control the temperature and pressure instead of the ambient conditions. The *in situ*

observation is accomplished by the optic microscope and the detailed morphology of SWNT films by other common methods of characterization such as the Scanning Electron Microscope (SEM) and Atomic Force Microscope (AFM). Finally to study the optical properties of the special networks, the setups of fluorescence microscope and excitation spectroscope are introduced.

From chapter 4 to 6, the results and discussion focus on three different sorts of suspensions respectively: real coffee, surfactant-dispersed aqueous and polymer-sorting organic colloids. In the chapter 4, experiments on the real coffee suspensions first verify the effectiveness of the new setup we design. Some important conditions including the concentration of solutes and the height of capillary bridge can change the film morphologies in this simple and mundane case, which provides clues for the more complicated experiments with SWNTs.

The following chapter 5 presents the experimental results of SWNT aqueous colloids under the identical two-plate setup. We gradually alter both of the SWNT and surfactant concentrations and reveal that the typical striped pattern with aligned SWNTs can only be accomplished within a certain range. By achieving and suppressing the pinning/depinning motion, the pattern can transform from stripes to homogeneous film. Besides, two interesting and significant phenomena are identified by the *in situ* observation of CL dynamics. One of them called "breathing motion" describes a slightly reverse move of CL at the very pinning moment as the CL is taking a breathe after the jumping. It implies that the pinning could be a dynamical process instead of the conventional "stick" [40]. The other phenomenon called "kink" shows that the propagation of CL is not a direct jump or slip but usually follows a zipper-like motion horizontally along the CL. The kink is usually referred as the style of CL motion on super-hydrophobic or textured surfaces [41, 42] but seldom on the hydrophilic one. Combining with the dynamical pinning and kinked depinning from experimental analysis and theoretical simulation, we present a new model for the iterative coffee-stain phenomenon. In the final section of this chapter, similar experiments with thermally enhanced evaporation are performed in order to broaden the horizon of this method.

Likewise, we implement the fabrication of SWNT patterns in chapter 6 but this time SWNTs are dispersed by polymer conjugates in organic solvents. Chloroform is found to be the appropriate solvent for the controlled deposition due to its surface tension and evaporation rate in the ambient conditions. Similar results of striped pattern with much wider spacing is consistent with our model. Both the breathing motion for pinning and the kink for depinning reappear in the new system. The alignment of SWNTs and the critical effect

of ethanol are discussed as well. In the second section of this chapter, with the identical suspensions, a different strategy named Dose-controlled Floating Evaporative Self-assembly (DFES) is used to make the self-assembly of SWNTs on the water-air interface. The method is adapted from the work by Arnold *et al.* [43]. The whole process can be generally repeated nevertheless there are inevitable SWNTs networks between the regular stripes. Preliminary analysis shows that the coffee stain effect may dominate the whole process which can be explained by the same model under the geometry of capillary bridge. The last part of the chapter specifically focuses on the optical properties of these arrays containing well-aligned SWNTs made by the DFES method from the same suspensions. The characterization accomplished by fluorescence microscopy and excitation spectroscopy shows the preservation of semiconductor properties from single species of SWNTs and their special excitonic transition.

In the end, a concise summary of the most important results reported in this thesis will be stated and a short outlook provides some ideas on the further experiments and the possible applications of the solution-processed SWNT arrays in the future.

# 2 Solution-processed thin film deposition

For the past decades, solution-based deposition techniques have been widely recognized as more energy-efficient, cost-effective methods than the conventional top-down fabrication approaches [23, 44]. Furthermore, most of these techniques can be performed at near ambient conditions in contrast with some non-soluble materials depositions, like Vacuum Thermal Evaporation (VTE) or CVD [45–47], which typically require high vacuum and temperature.

In this chapter, we will first briefly introduce series of solution-based deposition techniques commonly used in the industry and in research on thin film fabrication (Figure 2.1). Both advantages and disadvantages of these exemplary methods will be compared and discussed according to the results from literatures.

Next, a specific mechanism of EISA method will be stated. Then fundamental physics of evaporation underlying various experimental setups and conditions will be discussed because it can provide insight into better controlled morphologies to achieve the optimized performance of thin film devices.

The final part includes some carbon nanotube basics which ensure the potential applications as transistors and solar cells. The separation and selection of SWNTs will be mentioned as the important preconditions for this work. Some previous attempts of solution-processed deposition will also be present as a necessary background to finally bring forward our ideas and experiments.

## 2.1 Review of several common deposition techniques

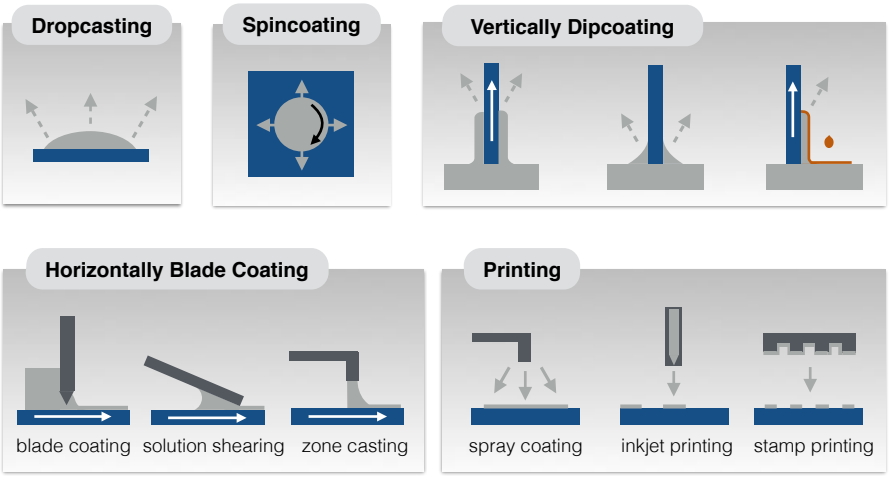


Figure 2.1: Schematic summary of solution-based deposition techniques. Adapted from ref. [44] by Diao *et al.*.

**Dropcasting**

Dropcasting is a facile and standard method which has been widely used in fabrication of thin films or patterns from carbon nanomaterials, organic or polymer solutions [48–50]. As shown in Figure 2.1, a droplet is casted on a substrate and then solvent evaporation drives the deposition to form either individual crystals or a thin film [44]. Naturally, the film thickness is proportional to the particle concentration. Although it is a very simple and cost-effective method without any waste of material, the shortcomings are obvious. It has limitation in large area coverage, unfavorable uniformity, inadequate performance and poor reproducibility [51]. A variety of modifications thus have been developed to improve the technique.

For example, Kim D.H.*et al.* poured the poly(3-hexylthiophene) (P3HT) diluted $CHCl_3$ solution onto the highly doped silicon substrates in a sealed chamber. The solvent was allowed to evaporate very slowly in the closed jar, giving rise to long, high-quality wire crystals [52].

In another experiment, the dropcasting solution was exposed to unidirectional 100 Hz sound waves when evaporation happened [53], where this vibration-assisted deposition was found to enhance the device performance.

Besides, improvement of deposition quality can also be achieved by using combination of solvents [54, 55], substrate heating [56, 57], surface treatment [58] and even a multi-step process followed by recrystallization [59, 60].

Another important sort of modified dropcasting makes use of the pinning of droplet on the three-phase Contact Line (CL) [61], which can be referred as the typical coffee-stain effect [27]. When the droplet is pinning on the solid substrate, nucleation events occur along the edge of the meniscus and the growth of crystallization is guided and well-aligned single-crystals form [62]. The related mechanism and physics will be carefully discussed in the Chapter 2.2.

**Spincoating**

As the most often employed method in the microelectronic industry for the production of photoresists, spincoating is a well-known batch process the outcome of which is a thin film of effectively uniform thickness on a rigid disk, plate or even slightly curved lens [63]. Likewise, the solution here is also dropped onto a substrate. But simultaneously the substrate is accelerated rapidly to desired angular velocity in oder to spread the liquid and evaporate the solvent (see Figure 2.1). The liquid flows outward radially due to centrifugal force and the excess fluid spins off the edges of the substrate until the required thickness of the film is achieved by viscous force and surface tension. Then the film further thins by the combination of outward fluid flow and evaporation [64]. Therefore the higher the angular speed of spinning, the thinner the film. Besides, the solution concentration and viscosity can also affect the film thickness [44] which ranges from micrometers to nanometers [65].

Spincoating as a mature and scalable technique has lots of advantages. Film thickness can be easily modulated by changing the spin speed and solution viscosity. The coating uniformity of spincoating is typically much better than the dropcasting process which also needs longer time for deposition.

However, the disadvantages still exist. First the material efficiency of spin coating is as low as 2-5%, which means that 95-98% material is flung off and wasted [64]. The coating area is still limited due to the requirement of very high speed spinning. Furthermore, because the film dries fast in most cases, there is less time for molecules or particles to crystallize or get ordered [66]. But some post-deposition method like thermal annealing may give rise to better performance [67].

**Dipcoating**

Dipcoating is one of the traditional meniscus-guided coating methods which typically include a linear translation of the substrate and a evolution of a solution meniscus. As the name suggests, ordinary dipcoating involves a vertical withdrawal of a dipped substrate in a bath or reservoir [63] (see Figure 2.1). When the solvent evaporated, the non-volatile dispersed solute can be homogeneously distributed or organized into the final films on the substrate depending on the fluid flow within the meniscus [68]. For a good control of the film thickness, key parameters should be taken into account such as withdrawal velocity, solvent evaporation rate and solution surface tension.

Numerous modifications of the dipcoating method have been made to obtain better performance or special results. For example, a stationary silicon substrate was immersed in the SWNTs/SDS aqueous suspension and the evaporation happened in ambient conditions in order to make self-assemble well-aligned SWNTs stripes [33]. Combining with Langmuir-Blodgett film technique, a new method called Dose-controlled Floating Evaporative Self-assembly (DFES) was to let the droplets of suspension evaporate on the surface of water and the involving SWNTs-polymer conjugates could be deposited on the substrate through self-assembly at liquid-liquid interface [43]. Using an adapted method, some new results will also be discussed in Chapter 6 of this thesis.

**Blade coating**

The so-called blade coating technique actually has a variety of styles including doctor blading [69], solution shearing [70] and zone casting [71]. They all have a component like a knife's edge which passes over a solution reservoir and forms a homogeneous thin film by simultaneous and post evaporation (Figure 2.1). This method is suitable for the large-area deposition because of the flexibility on shape of blade, gap distance between blade and substrate, blade moving velocity and solvents [72].

Similar to spread a solution over a substrate, the blade coating has a much higher coating speed than the other techniques introduced above. So it can be further adapted to a continuous roll-to-roll technique to fabricate for example industrial-scale organic light-emitting diode or solar cell devices [73–75].

Diao Y.*et al.* designed and used a micropillar-patterned printing blade to enhance crystal growth and control crystal nucleation [76]. The idea that anchors nucleation at spots where the radius of curvature is the highest actually was also inspired by the fundamental coffee-ring effect.

**Printing**

Printing is a very general and loosely defined term that has been used in many different types of scientific research. Here, the printing method is specifically pointed to the process suitable for the large-area and high-efficient deposition. Differing from the meniscus-guided self-assembly, the printing primarily relies on the setup geometry and the way that the solution is injected to control the film morphology.

Spray coating is one of the common printing techniques. Similar to zone casting, the solution is ejected from a nozzle but aerosolized by an carrier gas to form droplets or very thin, contiguous wet films on a substrate. In this process, the solution can be rapidly spread over a large scale area. The relevant parameters not only include the typical ones like solution concentration, solvent surface tension and substrate temperature but also the controllable nozzle geometry, atomizing air pressure and distance between the nozzle and substrate [77–79].

Inkjet printing is a mature technique that already has wide commercial applications and also has been numerously used in different scientific research fields like light-emitting displays [80], thin film transistors [81], solar cells [82] and even tissue engineering [83]. A chamber is filled with the solution-based ink which can be ejected from a nozzle via a piezoelectric process (Figure 2.1). The ejected droplet then falls under competition between gravity and air resistance until it hits and spreads on the substrate. After spreading on the substrate, droplets follow the same behavior like normal dropcasting. Therefore it is more complicated to control the morphology of the whole arrays for example to form precisely ring-like or dot-like pattern [84].

Stamp printing, sometimes referred to as a "lithographic" process or nanoimprinting, spatially confines the solution within the elastomeric polymer protrusions to control evaporation and patterned array [44] (see Figure 2.1). Stamps usually made of Polydimethylsiloxane (PDMS) as the polymer mold can be designed and patterned to facilitate different types of arrays on the receiving substrate for example aligned conjugated polymers [85]. The kinetics of the adhesion process among stamps, solutions and receiving substrate need to be studied to yield optimized performance [86].

Table 2.1 summarizes the general advantages and disadvantages of those different deposition techniques discussed above. Regardless of the distinguished methods or other additional modifications, the biggest difficulty is to precisely control the thin film morphology. Evaporation always plays the key role during all of these solution-processed techniques. To understand and

develop distinct morphology control strategies, we will detailedly discuss the mechanism of EISA in the next section.

| **Methods** | **advantages** | **disadvantages** |
|---|---|---|
| Dropcasting | very simple<br>no waste of material | limitation in large area coating<br>thickness hard to control<br>poor film uniformity |
| Spincoating | film uniformity<br>thickness control<br>reproducibility | waste of material<br>limitation in large area<br>less time for ordering |
| Dipcoating | film uniformity<br>large area coverage | waste of material<br>time consuming |
| Blade coating | large area coverage<br>film uniformity<br>no waste of material | limited film thickness control |
| Printing | high efficient<br>large area coverage<br>film uniformity<br>reproducibility | setup complex<br>multistep process |

Table 2.1: Summary of advantages and disadvantages for different depostion techniques

## 2.2 Mechanism of evaporation-driven self-assembly

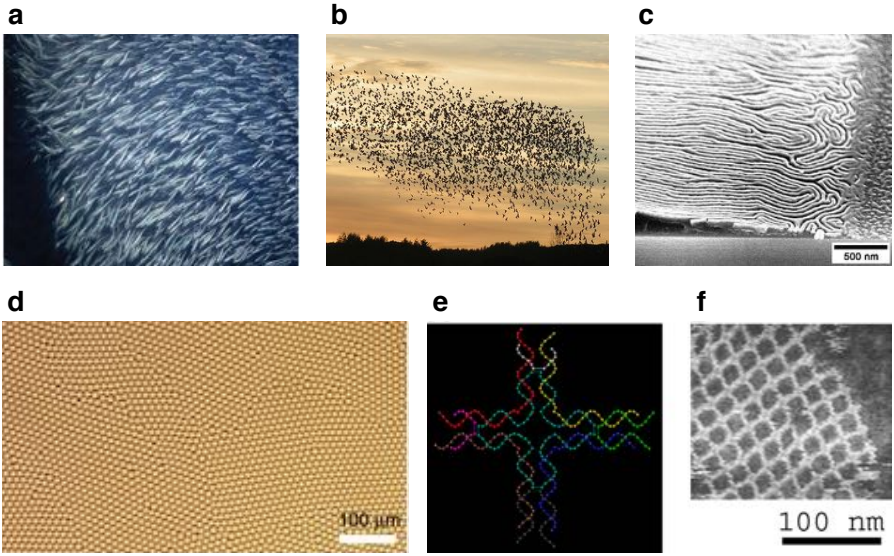


Figure 2.2: Examples of self-organization. (a) A school of fishes [87]. (b) A flock of birds. (c) Self-assembly of block copolymers from a well-aligned domain (left) to a randomly oriented domain (right) adapted from ref. [88] by Kim *et al.*. (d) An optical micrograph showing hexagonal ordering in dense arrays of liquid crystal colloids, with large-area crystallites separated by grain boundaries adapted from ref. [89] by Ackerman *et al.*. (e-f) DNA "tile" structure consisting of four branched junctions oriented at 90° intervals and an atomic force microscope image of a self-assembled DNA nanogrid adapted from ref. [90] by Strong *et al.*.

Self-organization or self-assembly refers to an autonomous process where the components of a system organize spontaneously to an ordered structure through direct interactions or indirectly driven by the environment [91]. It is a common phenomenon throughout nature and technology (see Figure 2.2). As summarized in the previous section, although there are so many solution processing techniques designed and invented for fabrication of thin film devices, a key challenge here is to precisely control the thin film morphology or

structure because it is crucial for the device to get desired performance [92,93]. Therefore, within these methodologies, understanding the mechanism of self-assembly becomes very important.

The dynamics of self-assembly are associated with thermodynamic equilibrium, characterized by a minimum in the system's free energy. This definition although it is too broad, can divide the self-assembly into two main types: static and dynamic [94]. As illustrated by Figure 2.3, the static self-assembly involves systems that are at global or local equilibrium without dissipation for example the thin film of liquid crystal colloids on an isotropic substrate (see Figure 2.2d). In contrast, the dynamic self-assembly, like the school of fishes in Figure 2.2a, typically happens in nature and biological systems which are dissipating energy when certain structures or patterns are formed (see Figure 2.3).

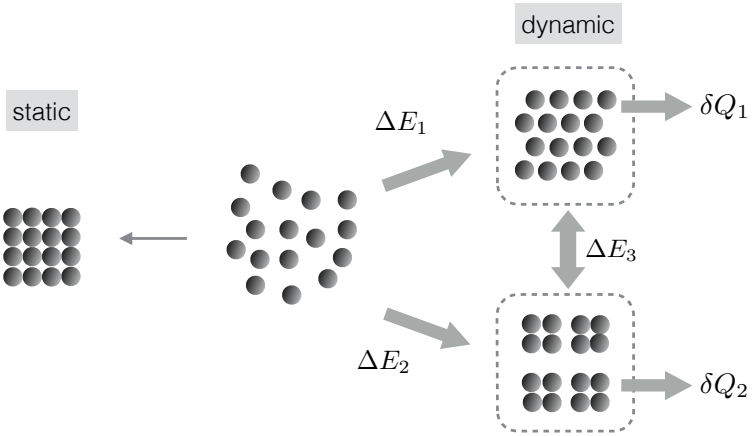


Figure 2.3: A schematic illustration for the difference between static (equilibrium) and dynamic (non-equilibrium) self-assembly. On the left, particles form a ordered state as a system approaches equilibrium. On the right, the flux of energy through the system induces different structures by different rates of energy input ($\Delta E_1$ and $\Delta E_2$) and dissipates as heat ($\delta Q_1$ and $\delta Q_2$).

However, when it comes to the technological applications of self-assembly especially with nanoparticles, an efficient scale-up and a high level of control will be required. The interaction between particles and thermodynamic driven force therefore need to be regulated, either by use of chemistry and

templating, or directed by means of external fields such as magnetic, electric or flow [95]. Given the breadth of the topic, in the present work, research and discussion will mainly focus on the flow directed self-assembly from a solution on solid substrates or liquid interfaces. The driving force here is very ordinary: evaporation.

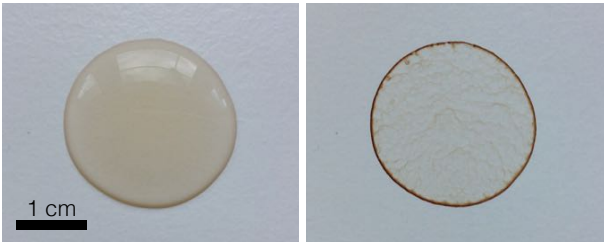


Figure 2.4: An example of the coffee ring effect. 0.5 mL volume suspension of espresso with 0.5 mg/mL concentration is casted on a office table.

Evaporation is a very fundamental physical phenomenon. It describes that a fraction of the molecules with enough heating energy escape from the surface of a liquid into a gaseous phase that is not saturated with the evaporation substance [96]. Although it happens everywhere in our daily lives, there are many interesting phenomena which are driven by it and inspire the scientists to study the physical complexity behind. For example, when a drop of coffee is spilled and dries on a table, it leaves a ring-like pattern which means the majority of coffee solutes do not homogeneously cover the drop area but pin and deposit on the edge of it [27, 97]. As shown by Figure 2.4, the initially well-dispersed coffee forms a concentrated ring after total evaporation, which is a typical evaporation-induced and flow-directed self-assembly process [94].

Now the question is: how does the evaporation make this self-assembly happen? A simple model treats a symmetric sessile (stationary) droplet as a spherical cap geometrically [98], whose shape is determined by the Young equation:

$$\cos(\theta) = \frac{\gamma_{\mathrm{SG}} - \gamma_{\mathrm{SL}}}{\gamma_{\mathrm{LG}}}, \tag{2.1}$$

where $\theta$ is the equilibrium contact angle, $\gamma_{\mathrm{SG}}$, $\gamma_{\mathrm{SL}}$ and $\gamma_{\mathrm{LG}}$ are respectively the interfacial energy between the solid-gas phase, the solid-liquid phase, and the liquid-gas phase. However, when the evaporation happens along the meniscus, we have to take non-equilibrium situation into account.

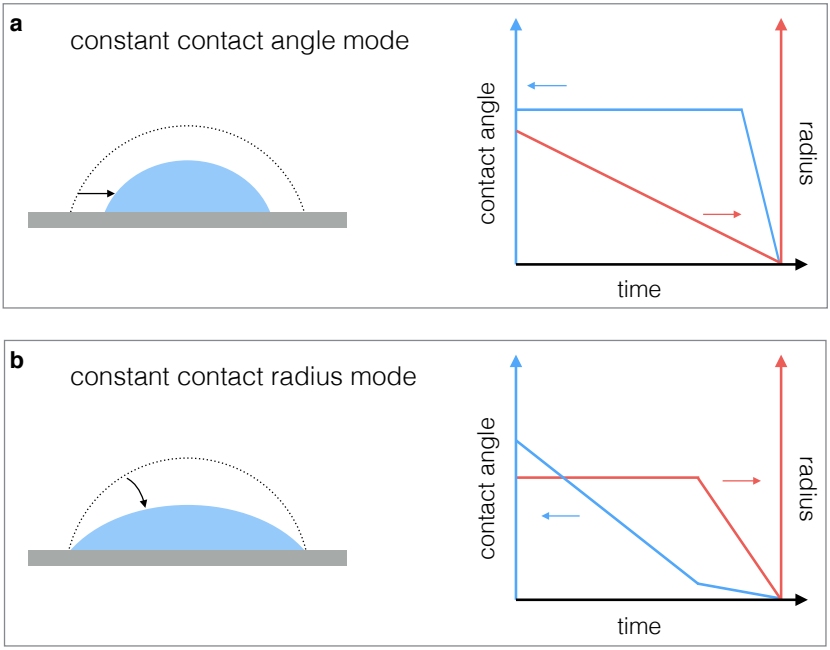


Figure 2.5: Schematics of two evaporation modes of sessile drops on the solid substrate: the change of the shape as a spherical cap (left) and the change of contact angle and radius during the drop lifetime (right).

As schematically illustrated in Figure 2.5, there could be two different modes of evaporation: constant contact angle or constant radius. The former one with continuously receding CL and persistent $\theta$ could be nearly treated like equilibrium state described by the Young Equation. But in the mode of constant contact radius (Figure 2.5b), the three-phase CL is pinned due to the presence of surface roughness or chemical heterogeneities [99] and can be further enhanced by the deposition of solutes. In this case, wetting hysteresis maintains the contact radius while $\theta$ decreases, until $\theta$ reaches a limiting value and then the contact line begins to recede [100].

For this mode of pinned CL, the evaporation is investigated experimentally [101, 102], by analytic theory [27, 103] and by computation using the finite element method (FEM) [98, 104]. On the basic assumption of the geometry as spherical cap, an axisymmetric drop is considered as shown in Figure 2.6a.

Deegan *et al.* pointed out the mechanism of coffee stain effect and presented a basic analytical solution [27]: for a ring-like morphology, the drying drop has to be first pinned at the CL and to keep the pinning, there must be a decrease of the contact angle and an outward capillary flow to replenish the liquid evaporating. This flow carries solutes to the CL and make the deposition happen there. However, in oder to get the analytic solution, here are several important assumptions.

First, the shape of a sessile droplet resting on a solid substrate is controlled by the Bond number ($Bo$) and the Capillary number ($Ca$):

$$Bo = \frac{gR^2(\rho_{\mathrm{L}} - \rho_{\mathrm{g}})}{\gamma} \tag{2.2}$$

$$Ca = \frac{\mu V}{\gamma} \tag{2.3}$$

where $g$ is the gravitational constant, $R$ is the contact-line radius, $\rho_{\mathrm{L}}$ and $\rho_{\mathrm{g}}$ are the liquid and gas density respectively, $\gamma$ is the liquid-air surface tension, $\mu$ is the liquid viscosity and $V$ is the fluid velocity induced by evaporation. In the situation of droplets, $Bo$ accounts for the balance of gravitational force and surface tension and $Ca$ represents the ratio of viscous force to surface tension [98]. Qualitatively speaking, both of gravitational and viscous forces tend to deform the spherical shape of the sessile droplet whereas the surface tension maintains it. Therefore, as for a small water sessile droplet with contact radius about 1 mm, height of about 0.3 mm and slow flow (1 µm/s), the Bond number is around $10^{-2}$ and the Capillary number around $10^{-8}$, so that the droplet shape can remain spherical during evaporation in this situation.

The second approximation is on the evaporation and diffusion process. For the time-dependent diffusion, we have the Fick's second law:

$$\frac{\partial c}{\partial t} = \nabla(D\nabla c) \tag{2.4}$$

where c is the mass of vapor per unit volume of air, t is the time and $D$ is the diffusion constant for vapor in air. When it comes to the surface of the sessile droplet, the time required for the vapor concentration to adjust to the change of the droplet shape is of the order of $R^2/D$, where $R$ as shown by Figure 2.6a is the initial radius of the droplet. Therefore if we have 1 mm contact radius of a water droplet, and $D$ for water to air in the ambient condition is 0.282 $\mathrm{cm}^2/\mathrm{s}$, the time will be about 0.03 s which is much shorter than the droplet

lifetime which is in the order of tens of minutes. The evaporation rapidly attains the steady state so that the diffusion equation reduces to Laplace's equation:

$$\nabla^2 c = 0 \tag{2.5}$$

A cylindrical coordinate system is presented by Figure 2.6a with r and z as radial and axial coordinate respectively. By using this coordinate system, the boundary conditions of eq 2.5 are:

$$\begin{aligned} &1.\ r < R, z = h(r) : c = c_v \\ &2.\ r > R, z = 0 : j = 0 \\ &3.\ r = \infty, z = \infty : c = Hc_v \end{aligned} \tag{2.6}$$

Here $h$ is the position of air-liquid interface, $c_v$ the saturated vapor concentration, $H$ the relative humidity of the ambient air and $j$ is the evaporation flux from the interface, which can be expressed like:

$$j(r) = -D\nabla c \tag{2.7}$$

Now it seems that $j$ might not be uniform along the air-liquid interface because the diffusive relaxation of the saturated vapor layer adjacent the interface is the rate-limiting step. Solving the Laplace's equation gives the analytic result. Deegan *et al.* [27] used the analogy between diffusive concentration fields and electronic potential fields. They found that the boundary value problem is also identical to that of charged conductor if $c$ is treated like the electrostatic potential and $j$ like the electric field [27]. Hence close to the CL

$$j(r) \propto (R - r)^{(\pi - 2\theta)/(2\pi - 2\theta)} \tag{2.8}$$

where $\theta$ is the contact angle, $(R - r)$ represents the distance from the CL. It is easy to calculate that when $\theta$ is relatively small (much smaller than 90°), $j$ is strongly enhanced toward the edge of the drop (see Figure 2.6b). This edge enhancement of evaporation can be observed when there is a curvature change along the CL as shown by Figure 2.6c. More coffee particles deposit on the corners with higher curvature than the side edges. The influence of CL curvature also has been numerically calculated before [105]. Then the mechanism that stated above is now more clarified: due to the nonisothermal conditions on the air-liquid interface, the evaporative flux is enhanced near

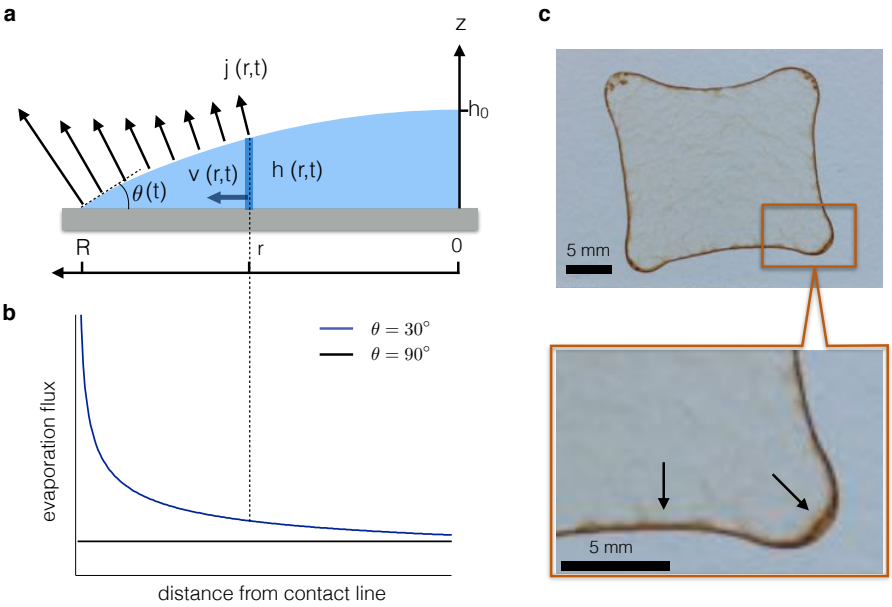


Figure 2.6: Mechanism of the coffee ring effect. (a) Schematic of relevant parameters for a sessile droplet with the shape of spherical cap in a cylindrical coordinate system: evaporative flux $j$, interface position $h$, contact angle $\theta$ and flow velocity $V$. (b) Evaporation flux along the droplet air-liquid interface with contact angle 30°(blue) and 90°(black). (c) A coffee stain with different curvatures of the edge on the table. Deposition is accentuated on the edge of high curvature.

the three-phase CL, which induces the capillary flow from the center to the edge where the deposition happens.

However, the story does not simply end here because the capillary flow that brings the solutes to the edge is not the only convective flow induced by evaporation in the sessile droplet situation. Due to the nonuniform cooling along the surface of a drying droplet that we discussed above, a temperature gradient is induced, which in turn, leads to a surface-tension gradient along the air-liquid interface. This gradient gives rise to the Marangoni flow which can carry solutes from the area of low surface tension to that of high surface tension [106,107]. Therefore, in the situation of sessile droplets, the Marangoni effect can generate the flow from the edge of the droplet toward the top

of it. The Marangoni flow hence can prevent the deposition at the drop perimeter [108] and if it is combined with the outward capillary flow, as shown by Figure 2.7b, there will be an "eddy" near the CL [109] and the coffee-ring deposition is suppressed in this case [108].

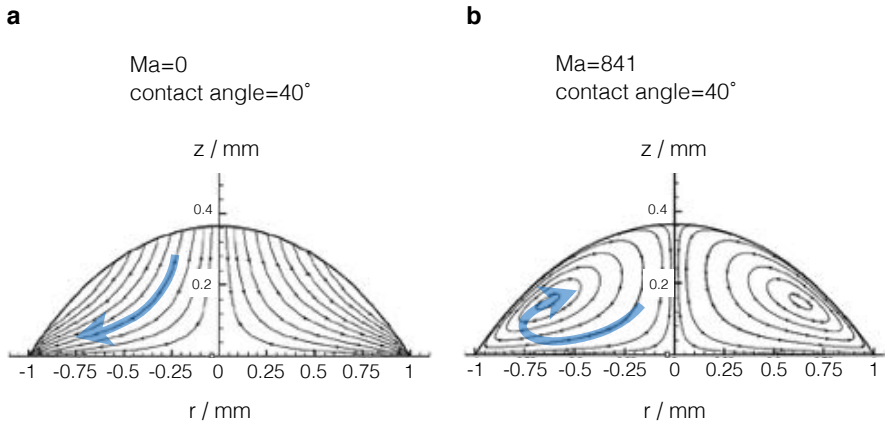


Figure 2.7: (a) A droplet with low Marangoni number has outward capillary flow. (b) A droplet with high Marangoni number has vortex near CL induced by both capillary and Marangoni flow. The simulation data is adapted from the reference [110].

Normally the solid substrate has the larger thermal conductivity than the liquid (e.g. 0.96 $Wm^{-1}K^{-1}$ for glass and 0.6 $Wm^{-1}K^{-1}$ for water), which means the larger contact angle can make the top of the droplet even colder than the edge and consequently the Marangoni effect can be enhanced [104, 110]. The Marangoni number ($Ma$) is a dimensionless number used to quantitatively describe this effect:

$$Ma = -\frac{\mathrm{d}\gamma}{\mathrm{d}T}\frac{R\Delta T}{\mu\alpha} \tag{2.9}$$

where $\gamma$ is the surface tension, $T$ the temperature, $R$ the droplet radius, $\mu$ the dynamic viscosity of the liquid and $\alpha$ the thermal diffusivity.

Besides temperature, the surface-tension gradient also can be induced by surfactants concentration [111]. Especially in our aqueous solution with SWNTs and SDS on the silicon wafer, the small contact angle (15-20°) can effectively suppress the temperature gradient and the SDS concentration gradient from

the CL to the top will dominate the whole process which will be discussed in Chapter 5.

So far a very simple and analytical mode has been briefly presented above for the question of the evaporation of a sessile droplet. Although the main factors have been discussed, there are still several approximations which are important in the fluid physics but have not been mentioned yet because typically they are negligible in this situation. For example, convective heat transfer within the droplet has been neglected because it is much smaller than the conductive heat transfer when temperature is not very high [109]. The ratio between convective and conductive heat transfer can be expressed by the dimensionless Rayleigh number ($Ra$). The inertia of flow is ignored because the ratio between it and viscosity, which is also called Reynolds number ($Re$), is very small here.

All the important dimensionless numbers discussed above are summarized in Table 2.2 along with their approximate range of values and effects in the case of the small water drop. The values of these numbers are estimated on the following:

droplet radius $R = 0.5 - 2$ mm;
liquid density $\rho_{\mathrm{L}} = 998$ kg/m$^3$, air density $\rho_{\mathrm{g}} = 1.225$ kg/m$^3$;
water surface tension $\gamma = 0.072$ N/m at 298 K;
the dynamic viscosity $\mu = 1.002 \times 10^{-3}$ kg/m·s;
capillary flow velocity $V = 10^{-1} - 10^{2}$ µm/s;
temperature induced surface tension gradient $\mathrm{d}\gamma/\,\mathrm{d}T \approx -10^{-4}$ N/m·K;
thermal diffusivity of water at room temperature $\alpha = 1.43 \times 10^{-7}\ m^2/s$;
thermal expansion coefficient $\beta = 2 \times 10^{-4}$ K$^{-1}$;
surface temperature $T_s = 298 - 300$ K, ambient temperature $T_\infty = 298$ K;
the kinematic viscosity $v = 1.004 \times 10^{-6}$ m$^2$/s;
the diffusion coefficient of water $D = 2.45 \times 10^{-5}$ m$^2$/s.

| number | equation | range | effect |
|---|---|---|---|
| Bond | $Bo = \frac{gR^2(\rho_L - \rho_g)}{\gamma}$ | $10^{-2} - 10^{-1}$ | the droplet shape can be treated like spherical cap |
| Capillary | $Ca = \frac{\mu V}{\gamma}$ | $10^{-8} - 10^{-5}$ | the droplet shape maintains spherical during evaporation |
| Marangoni | $Ma = -\frac{\mathrm{d}\gamma}{\mathrm{d}T}\frac{R\Delta T}{\mu\alpha}$ | $10^{-1} - 10^{3}$ | inward flow near the interface when there is surface-tension gradient |
| Rayleigh | $Ra = \frac{g\beta(T_s - T_\infty)R^3}{\alpha v}$ | $10^{-1} - 10$ | buoyancy driven flow can be neglected except at very high surface temperature |
| Reynolds | $Re = \frac{VR}{v}$ | $10^{-3} - 10^{-1}$ | the inertia force is negligible for given flow conditions |
| Péclet | $Pe = \frac{VR}{D}$ | $10^{-6} - 10^{-3}$ | the evaporation is dominated by the diffusion of liquid vapor into air |

Table 2.2: Summary of important dimensionless numbers for droplet evaporation.

## 2.3 CNTs for thin film fabrication

Leveraging these solution-processed large-area deposition techniques, carbon nanotubes are emerging as a multifunctional coating material which has great potential in many different kinds of applications like solar cells, transistors or displays [112, 113]. The structure of a SWNT can be considered like a wrapping graphene which is a one-atom thick layer of graphite as schematically illustrated by Figure 2.8. The honeycomb crystal lattice of graphene can be described by two vectors $\vec{a_1}$ and $\vec{a_2}$ (Figure 2.8). These two basic vectors combining with a pair of chiral indices (n,m) define the way the graphene sheet is wrapped and furthermore the structure of SWNTs:

$$\vec{C} = n \cdot \vec{a_1} + m \cdot \vec{a_2} \tag{2.10}$$

where the vector $\vec{C}$ represents the direction that the graphene sheet is rolled. The integers n and m denote the number of $\vec{a_1}$ and $\vec{a_2}$ respectively and divide the SWNTs into three different types: armchair (m=0), zigzag (n=m) and chiral (others) tube. In this study, we will particularly focus on the chiral tubes, especially on the (6,5) tube (see Figure 2.8) due to its semiconductor properties [114]. Although these chiral nanotubes with large aspect ratio, direct band gaps show promise for a wide range of applications due to a combination of their unusual structural, mechanical and electronic properties, the limited processing ability hinders them to reach their full potential.

To remove this obstacle, the DGU technique [16] and the recently developed polymer-selective method [20] provide single-chirality and well-dispersed SWNTs in water or certain organic solvents. Both of the two methods will have detailed descriptions in the next Chapter. Nevertheless, even with the homogeneous dispersion of nanotubes, to produce uniform and ordered assemblies remains a challenge. To achieve and understand this, the coffee-ring effect and other coating techniques we discussed above are not enough. We also have to take into account the unique structure of carbon nanotubes and their behavior in the liquid.

We can consider the carbon nanotubes here as extremely long rodlike molecules, with a length of L and a diameter D and L$\gg$D. The density of the rods in a system is $n$. When $n$ is relatively small, the rods should stay an isotropic distribution in orientation in order to maximize the orientational entropy [115]. However, when $n$ increases to a certain critical value ($n_c$), the geometric exclusion effects force the rods to line up parallel to one another, which is a typical phenomenon in liquid crystal research called isotropic-to-nematic

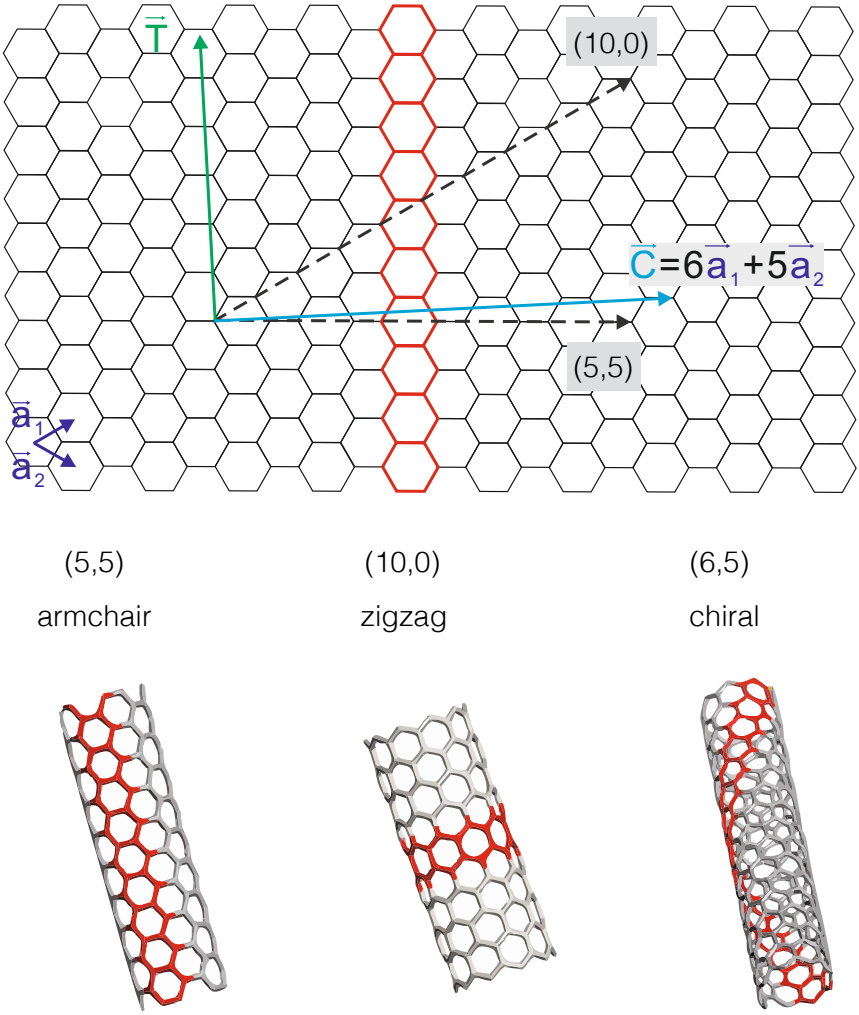


Figure 2.8: Basic structure and three types of SWNTs. $\vec{a_1}$ and $\vec{a_2}$ are two basic vectors. $\vec{C}$ is the symmetry axis for rolling up the graphene sheet. $\vec{T}$ points out the tube axis.

transition [116] as shown in Figure 2.9. If the aspect ratio of the rods (L/D) increases, $n_c$ will decrease [115]. A calculation of this transition was first done by Onsager [117] as early as 1949 on the basis of his excluded volume entropy model. Onsager's model asserts that although there is a loss of orientational entropy after this transition, a larger translational entropy can be gained and outweigh the loss in the parallel ordering of rods because the excluded volume between neighboring rods is minimized by making them parallel. In 2003, Windle *et al.* saw the similar formation of the liquid crystalline phase of multiwall carbon nanotubes in aqueous dispersion [118].

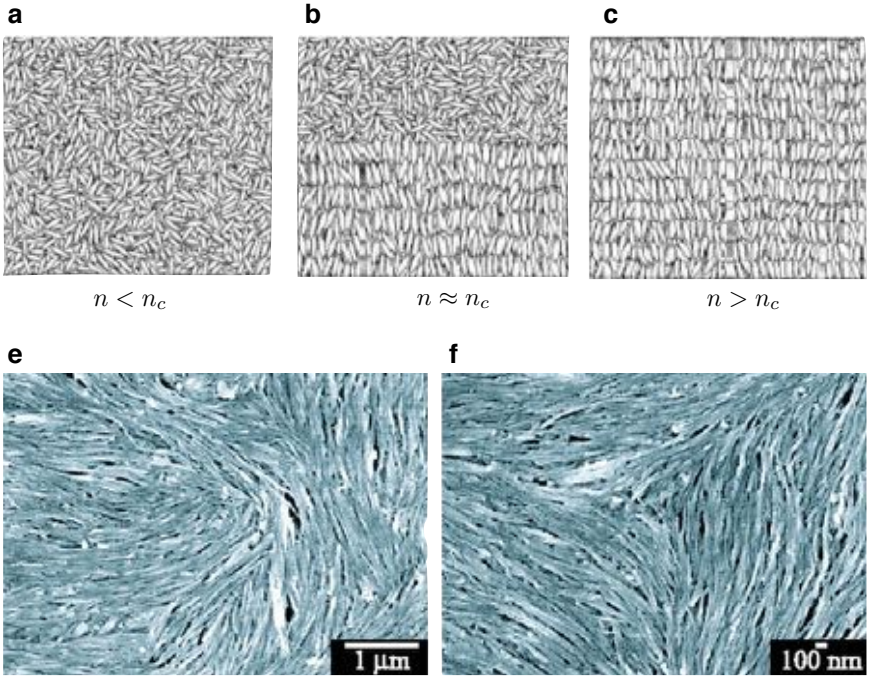


Figure 2.9: Snapshots taken from a simulation of rod shaped molecules, exhibiting (a) an isotropic phase ($n < n_c$) (b) a transition state when $n \approx n_c$ (c) an nematic phase ($n > n_c$). (e) and (f) are SEM images from the experiment of multiwall carbon nanotubes showing a Schlieren texture like a nematic liquid crystalline phase. Adapted from the ref. [118] by Song *et al.*.

Furthermore, this tendency of transition is favored even further if one includes the anisotropy of the attractive intermolecular interactions among nanotubes (e.g. Van der Waals forces), which also favor parallel alignment as in the Maier-Saupe mean field theories [33, 119].

Thanks to these techniques and theories, the well-dispersed semiconductor SWNTs have already been used for thin film fabrication including sorts of ordered patterns or arrays and their optoelectronic, electronic, transport and mechanical properties have been tested for device applications [33, 113, 120, 121].

Although the solution-processed methods are cost-efficient and suitable for large-scale fabrication of nanotubes, the patterns of the thin films and the alignment of CNTs, which could highly affect the performance of the device, are still hard to control. The traditional method for the EISA of SWNTs is typically time-consuming [33]. The experimental conditions including the concentrations of SWNTs and surfactants have to be further optimized and clarified. The mechanism is to some extent ambiguous and cannot fully explain some phenomenon observed during the process.

Therefore, we prepared single-chirality semiconductor (6,5) or (7,5) SWNTs which were dispersed by surfactants or polymers. The colloid of SWNTs was injected into different setups for the thin film fabrication by the EISA and the process was monitored and recorded respectively by optical microscope and camera. On the basis of these data, some new phenomena would be emphasized and a new physical model for the coffee-stain effect with carbon nanotube colloid would be presented and discussed in the thesis.

# 3 Experimental methods

## 3.1 Sample preparation

### 3.1.1 Density gradient ultracentrifugation

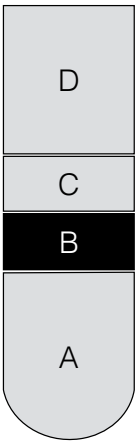


| | | | |
|---|---|---|---|
| D | 4 mL | 20 (w/V)% Iodixannol | 1:1 SC/SDS, 1.1 w% |
| C | 1.5 mL | 25 (w/V)% Iodixannol | 1:1 SC/SDS, 1 w% |
| B | 1.5 mL | 30 (w/V)% Iodixannol | 1:1 SC/SDS, 0.35 w% (1 w% DOC + SWNTs) |
| A | 4 mL | 40 (w/V)% Iodixannol | 1:1 SC/SDS, 0.75 w% |

Figure 3.1: DGU gradient: the bottom layer of the density gradient consisted of 4 mL 40% (w/v) iodixanol solution, above which were 1.5 mL 30%, 1.5 mL 25% and a top layer of 4 mL 20% iodixanol solution. The sonicated SWNT material with Sodium Deoxycholate (DOC) was added to the layer with 30% iodixanol solution.

Aqueous colloidal suspensions of Sodium Dodecyl Sulfate (SDS) stabilized SWNTs (CoMoCat SG65, *SWeNT SouthWest Nanotechnologies*) were obtained by dialysis from DGU method as described by Arnold *et al.* [16]. 12 mg raw CoMoCat material was first mixed with 6 mL 1 wt% DOC water solution and tip-sonicated with ice bath for 90 min in ultrasonication (Sonifier S-450A,*Branson*).

Then the solution was mixed with iodixanol (OptiPrep,*Sigma Aldrich*) and added in an ultracentrifugation vial with SDS and Sodium Cholate (SC) water solution in different ratios following the procedure described by Figure 3.1.

Before ultracentrifugation vials were aligned horizontally for 2 h to let steps in the density gradient blend diffusively. (6,5) SWNTs were separated after ultracentrifugation (Optima L-90K, SW 41 swinging bucket rotor, *Beckman Coulter*) for 18 hours at 41000 rounds per minute (rpm) and 21℃ as shown by Figure 3.2.

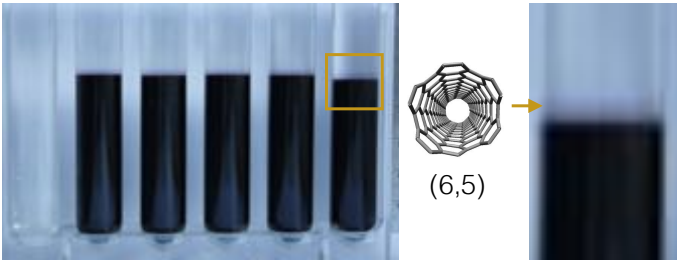


Figure 3.2: Separated layers of (6,5) SWNTs after 18 h ultracentrifugation by 41000 rpm at 21℃.

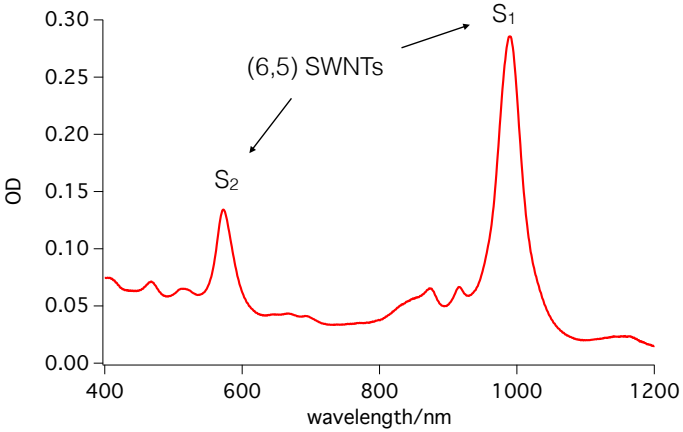


Figure 3.3: Absorption spectrum of (6,5) SWNTs from DGU process

Fractionation of the centrifuged samples was accomplished using upward

displacement with Fluorinert FC-40 (*Sigma Aldrich*) as density chase medium. Fluorinert was injected at the bottom of the vials with a syringe pump (*kd Scientific*) and about 200 $\mu$L of single chirality (6,5) SWNTs suspension was collected for further dialysis.

After dialysis with different concentration of SDS, absorption spectra and Optical Density (OD) value of the suspensions were measured using a Cary 5000-UV–VIS-NIR-spectrometer (*Varian*) (see Figure 3.3) in order to carefully control the concentrations of SWNTs for the next step film fabrication. $S_1$ and $S_2$ indicate the excitonic states in a (6,5) carbon nanotube. The details of exciton related optical properties of SWNT are introduced in Section 6.3.

### 3.1.2 Polymer-sorting SWNTs

The samples of dispersed SWNTs in $CHCl_3$ enriched in single chiralities were prepared by the use of a polyfluorene based polymers, for which the selective wrapping of certain semiconducting SWNT-species is known [20]. Two types of polymers were used, namely poly[(9,9-dioctylfluorenyl-2,7-diyl)] (PFO) and poly[(9,9-dioctylfluorenyl-2,7-diyl)-alt-co-(6,6'-2,2'-bipyridine)] (PFO-BPy).

20 mg of PFO or PFO-BPy and 10 mg of CoMoCat SWNT raw material were suspended in 30 mL of Toluene and ultrasonicated for 5 h (see Figure 3.4a). After that the solution was subjected to bench-top centrifugation (*Heraeus Sepatech*) at 14000 rpm for 5 min. The supernatant was collected and characterized by absorption spectroscopy (Figure 3.4b).

In order to get rid of the excess polymer, the supernatant was filtered over a nitrocellulose filter which was subsequently dissolved in acetone and the floating membranes of SWNTs/polymer conjugate were collected.The membrane was then rinsed by acetone for 3 times in order to wash residues of the filter away. After evaporation of the acetone, 1 mL of $CHCl_3$ was added to dissolve the membrane and the samples were then cup-sonicated for another 2 h.

Solutions were bath-sonicated until immediately before use for fabrication to prevent bundling and aggregation of SWNTs.

### 3.1.3 Preparation of coffee suspension

Espresso (*Poccino*), directly from supermarket, was dissolved and bath-sonicated in High Performance Liquid Chromatography (HPLC) water with concentration 1 mg/mL. The suspension then was centrifuged at 14000 rpm for 3 min to get rid of big aggregates. The supernatant was collected and diluted for further experiments.

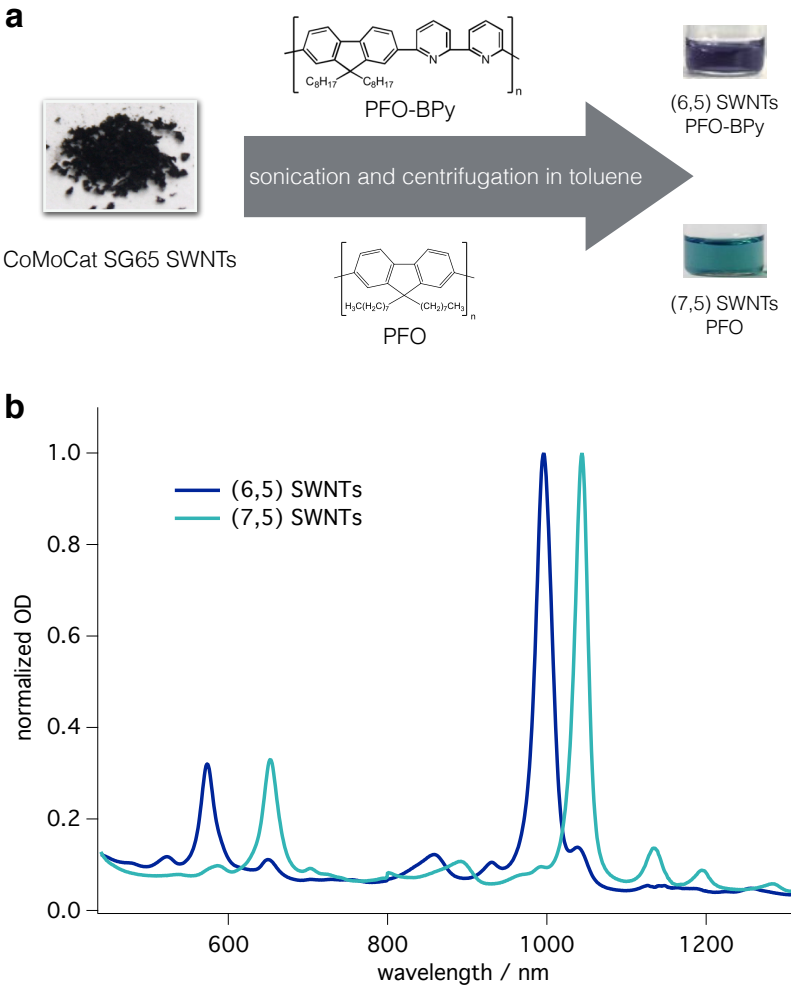


Figure 3.4: Polymer/SWNTs conjugates sample preparation. (a) Schematic diagram of conjugates preparation process. (b) Absorption spectrum of (7,5)SWNTs/PFO and (6,5)SWNTs/PFO-BPy in toluene.

## 3.2 Setups for thin film fabrication

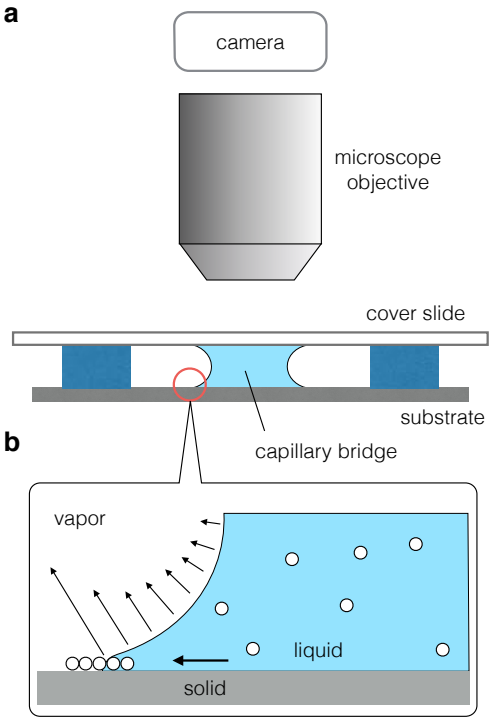


Figure 3.5: Schematic illustration of experimental setup. (a) Microscope setup with two-plate geometry and capillary bridge. (b) Meniscus geometry, including three phases CL, vapor flux and capillary flow.

A two-plate setup was used to fabricate SWNT and other sorts of thin films as schematically illustrated by Figure 3.5a. The setup provides superior stability and control of growth conditions during film formation if compared to evaporation from sessile (stationary) droplets or by vertical deposition [33, 35]. It is because the small gas-solvent surface area that constrained by the two plates increases the frequency of surface waves, which thereby decouples the system from low-frequency environmental perturbations. Therefore, the experiments can be implemented without the strict isolation of vibration and the *in situ* observation becomes possible.

The length of capillary bridge can be controlled by changing the distance between the two plates from 100 to 1200 µm in our experiments. 20-50 µL colloidal suspensions can be added in-between the two plates. Solvent evaporation proceeded at room temperature and atmospheric pressure except the controlled temperature experiments. Video sequences were taken from the CL on the bottom substrate by a microscope objective and a digital camera.

Silicon wafers (*MicroChemicals*) and glass cover slides (*Paul Marienfeld GmbH & Co. KG*) were cleaned with the piranha solution (3:1 mixture of 95% sulfuric acid and 30% hydrogen peroxide). After piranha treatment, wafers and slides were rinsed with HPLC water then blown dry with $N_2$. The glass cover slides were subsequently exposed to Hexamethyldislizane (HMDS) vapors to make the surface hydrophobic, which is especially for the dynamical pinning and breathing motion observation (see Section 5.2). The silicon wafer is also processed by the HMDS for the application in the dose-controlled floating evaporation self-assembly (DFES) experiment in Chapter 6. The Si wafers and glass slides were cut to proper size before use.

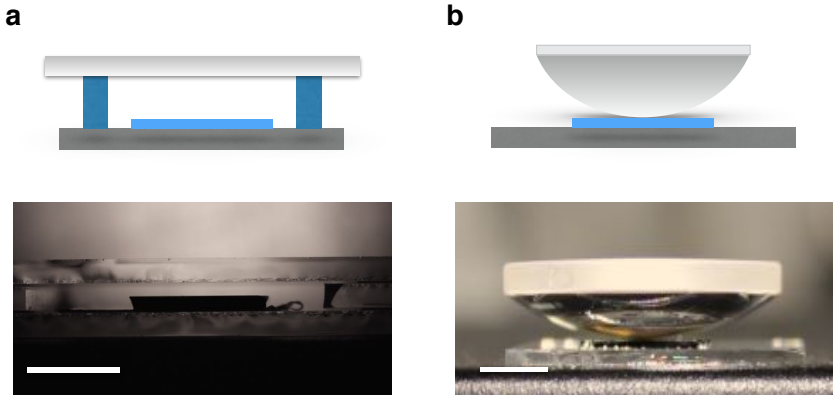


Figure 3.6: Schematics and images of experimental setup. (a) Two plates. (b) Lens. The scale bars are 5 mm.

In order to study the effect of capillary bridge length on evaporation and CL velocity, a lens setup was used (Figure 3.6b) because of its continuous decreasing of the meniscus height during evaporation.The uncoated N-BK7 Plano-Convex Lens was obtained from *Thorlabs*.

A home-built temperature control setup was used for temperature changing experiments as shown by Figure 3.7. The silicon wafer substrate is located

on the concave rectangular area and the glass cover slid is fixed upon it on the surface with a accurately designed gap 500 µm. The concave platform connected with a Peltier heating controller (*Quick-Ohm Küpper & Co. GmbH*) can raise the temperature from ambient to 100 ℃ and maintain stable in tens of seconds.

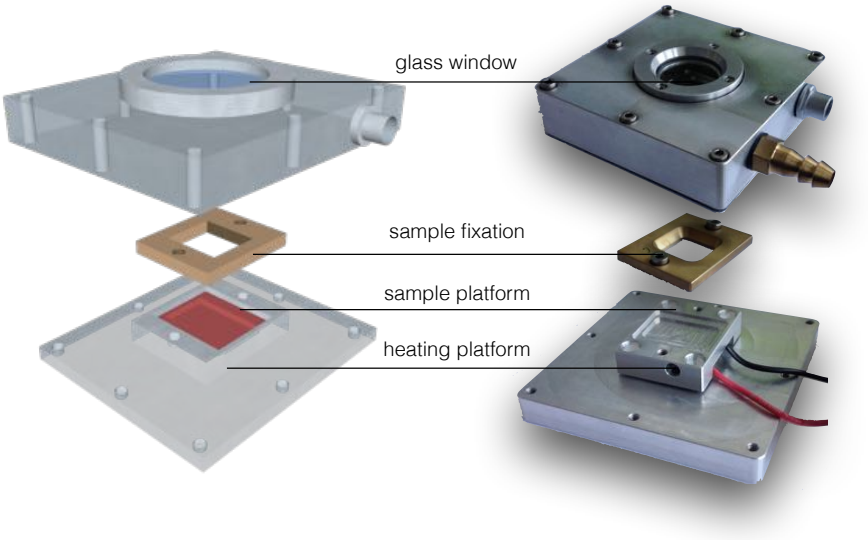


Figure 3.7: Temperature control setup.

As shown by Figure 3.8a, the Peltier controller, also called the heat pump, is a common thermoelectric device which is used for temperature stabilization on the basis of Peltier effect. Briefly speaking, when a current is made to flow through a junction between a P-doped and a N-doped semiconductor, heat can be generated or removed at the junction by simply changing the direction of the current. As schematically illustrated in Figure 3.8c, many couples of these P and N type semiconductors as Peltier elements are placed thermally in parallel to each other and electrically in series between two thermal foils. When the DC current flows through the device, the heat flow is taken from the cold side and transferred to the hot side of the element where a temperature sensor is used to give the feedback signal. The heatsink below keeps the devices running efficiently and prevents them from overheating. Figure 3.8b shows that the temperature can increase to 80 ℃ within several seconds and

become stable very soon. When the substrate and cover slide are fixed by a metal cover, the colloids can be injected between the two plates and the observation by the microscope is through the window on the top.

Another setup is built for special dose-controlled, floating evaporative self-

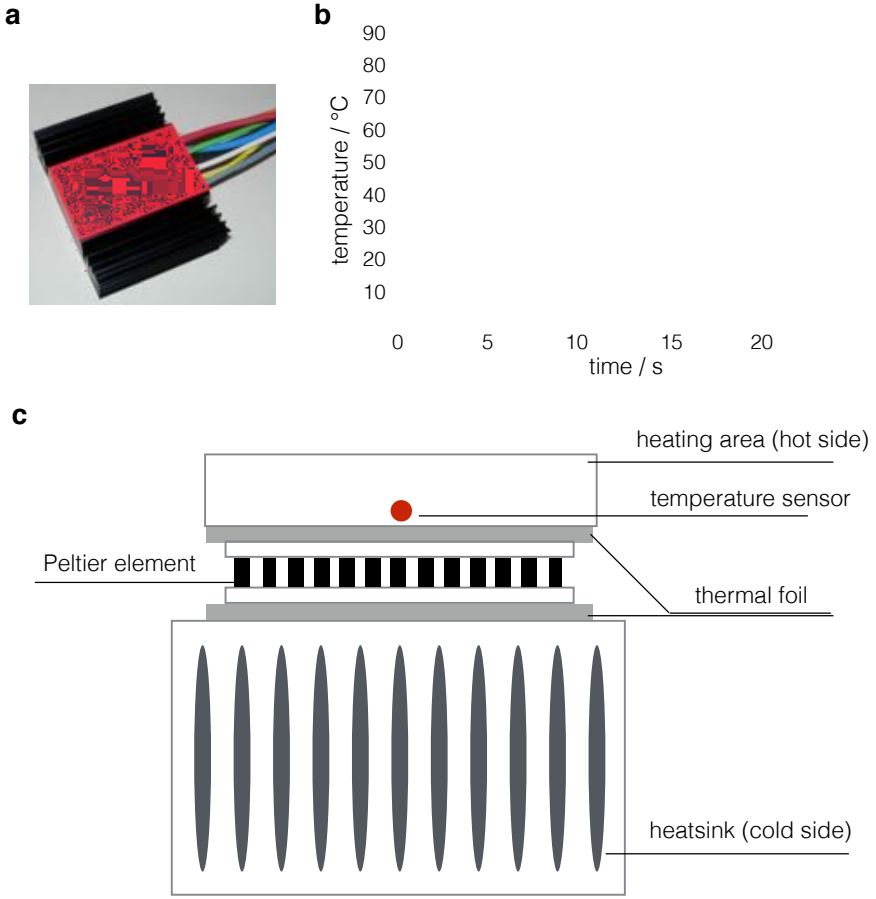


Figure 3.8: (a) A Peltier controller. (b) The rate of heating and temperature stabilization. The target temperature is set to 80 °CThe data is from the manufacturer. (c) The schematic illustration for the basic structure of a Peltier device.

assembly (DFES) experiments in Chapter 6. The general mechanism of DFES technique is on the basis of self-assembly on the air/water interface. Alike the schematic illustration in Figure 3.9a, a substrate connected by a dip-coating machine is immersed partly into the water (Milli Q, resistively ca. 18.2 MΩ·cm). A droplet of the solution which contains particles for the deposition is delivered in front of the substrate with the distance about 0.5 cm. A syringe pump is used to control the volume and speed of the droplets so that the deposition on the air/water interface can be transferred onto the substrate by spreading of the organic solution on the water surface. Meanwhile the substrate is pulled up by the dip-coating machine with a certain speed in order to control the deposition region and make regular striped patterns.

The substrate here is processed by the procedure that we introduced above in Section 3.3. The preparation of SWNT suspensions follows the same method described in Section 3.1.2 except that certain ratio of ethanol (1%-2%) is added just before the experiment. This effect, along with other crucial parameters such as the SWNT concentration, the pulling speed and the injection rate, will be detailedly discussed in Chapter 6.

## 3.3 Optical setups

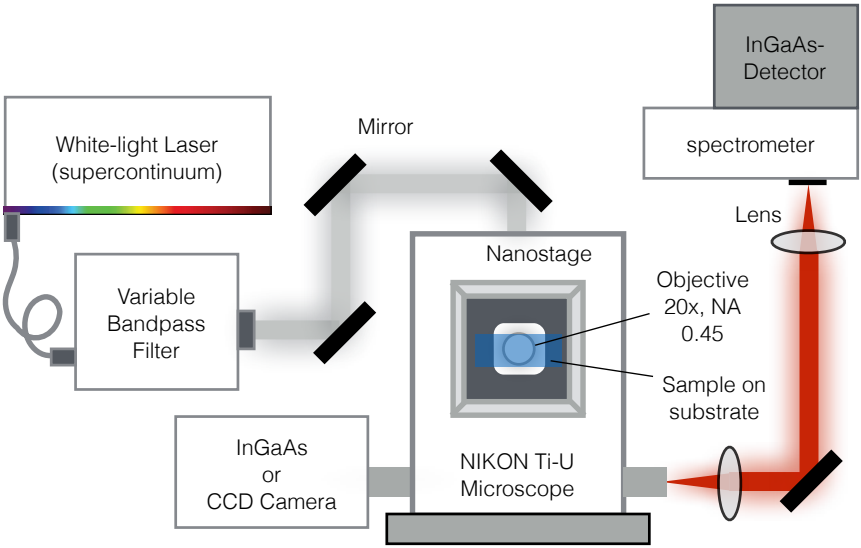


Figure 3.10: Schematic visualization of the optical part of the Photoluminescence Excitation (PLE) map setup.

Photoluminescence excitation (PLE) mapping was conducted on a home-built setup, based on a Shamrock spectrograph (SR-303i, *Andor*) and an Indium Gallium Arsenide (InGaAs) array detector (iDus, *Andor*). Excitation was accomplished by a supercontiuum light source, supplied with a variable bandpass filter (SuperK Extreme EXR-15 & SuperK Varia, *NKT Photonics*). As illustrated by Figure 3.10, samples were placed on a home-built Nanostage on the basis of a nanopositioner (PIMars P-563.3CD) and piezocontroller (E-712.3CDA) under which the excitation laser was through an objective (CFI S Plan Fluor ELWD 20×/0.45 N.A., *Nikon*). In order to obtain the PL image in the visible spectral window at the same time, either an interline Charge-Coupled Device (CCD) camera (Clara, *Andor*) or in the near infrared an InGaAs Camera (Xeva-1.7-320, *LOT-QuantumDesign*) were also used.

For Photoluminescence (PL) imaging, a continuous wave (CW) laser ($\lambda$=568 nm, *Coherent Inc.*) was applied to excite the second excitonic subband of SWNTs. The same InGaAs camera was used and attached to an inverted

epi-fluorescence microscope (Ti-U, *Nikon*) with a CFI Super Plan objective (100×/1.4 N.A., *Nikon*).

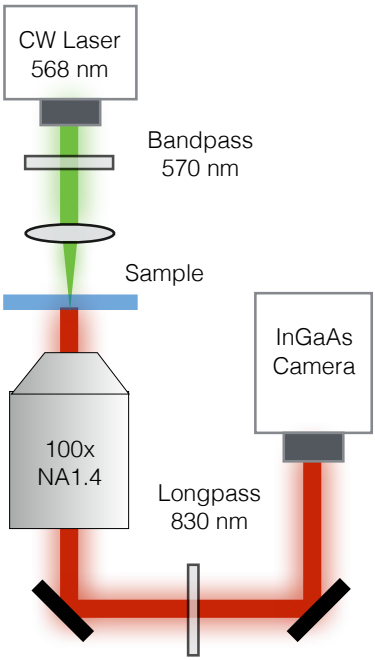


Figure 3.11: Schematic visualization of the optical part of the PL image setup.

## 3.4 Microscopic characterization

The dynamics of the CL were observed by optical microscopy (BX41, Olympus) using an Olympus objective (MPlan, 10×/0.25 N.A.). Video sequences were first recorded by a digital camera with 720x576 pixel resolution at 30 frames per second (fps) for the general observation. Then a *GoPro* camera (HERO3 Silver) with 1280×720 pixel resolution and 120 fps was applied especially for the dynamics research.

A field emission SEM (Ultra plus, *Carl Zeiss*) was used to investigate the microscopic structure of SWNT films. The operating voltages for the SWNTs from SDS suspensions were as low as 0.5 to 1.0 kV but for the polymer/SWNT conjugates they were raised to 5.0 kV.

AFM images were obtained with Nanosurf Easyscan 2 (*Nanosurf GmbH*) in the tapping mode using Tap190Al-G tips (*Budget Sensors*).

# 4 The real coffee-stain pattern

Before the experiment of carbon nanotubes, we tested the real coffee suspensions not only as the traditional dropcasting coffee-ring style but also under our two-plate and lens setups. All of these experiments are made in the ambient conditions and only the substrates on the bottom are analyzed. From the simple real-coffee tests, the important factors involving the EISA process can be demonstrated. As shown in Figure 4.1, the coffee suspension with three different concentrations (0.5, 1 and 2 mg/mL) but same volume (2 µL) were dropcasting on the surface of silicon wafer.

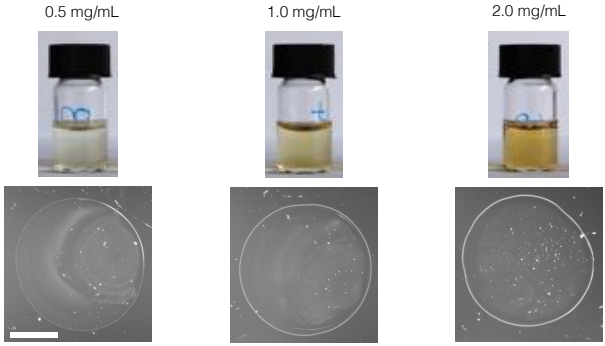


Figure 4.1: Ring patterns from the real coffee suspensions and dropcasting method on the silicon wafer surface. The scalebar here is 1 mm.

All of these suspensions can successfully form the single ring pattern on the surface and the thickness of the ring is evidently increased when it comes to the higher concentration. However, when we use about 20 µL the same solutions to repeat the EISA process under the two-plate setup, the situation changes. The distance between the two plates is fixed at about 550 µm for all of the three suspensions but not all of them follow the same repeated coffee-ring effect with the reservoir. Figure 4.2 shows that both the CL motion and deposition pattern are changed due to the difference of concentrations.

By analyzing the video sequence of the CL motion, we can trace the CL evolution when it is receding on the silicon wafer surface during the evaporation. When the concentration is as low as 0.5 mg/mL, it is obvious that the CL cannot pin like normal coffee-ring effect but move continuously as shown by the black straight line in Figure 4.2a. The corresponding deposition pattern is also irregular dots or short stripes perpendicular to the CL (the optical microscopic image in Figure 4.2b). But when the concentration increases to 1.0 mg/mL, the clear and regular stripe pattern arises and the motion of CL becomes like "steps" (the red curve in Figure 4.2a). It is because the CL gets pinned and depinned following the coffee-ring effect and due to the enough solutes from the reservoir, the process can be repeated on the wafer surface, which is similar with the multi-rings structure reported before [100, 122]. If we keep increasing the concentration to 2.0 mg/mL, the regular stripe pattern start vanishing. Then it can be confirmed that the solutes concentration plays an important role on the deposition pattern in the two-plate setup.

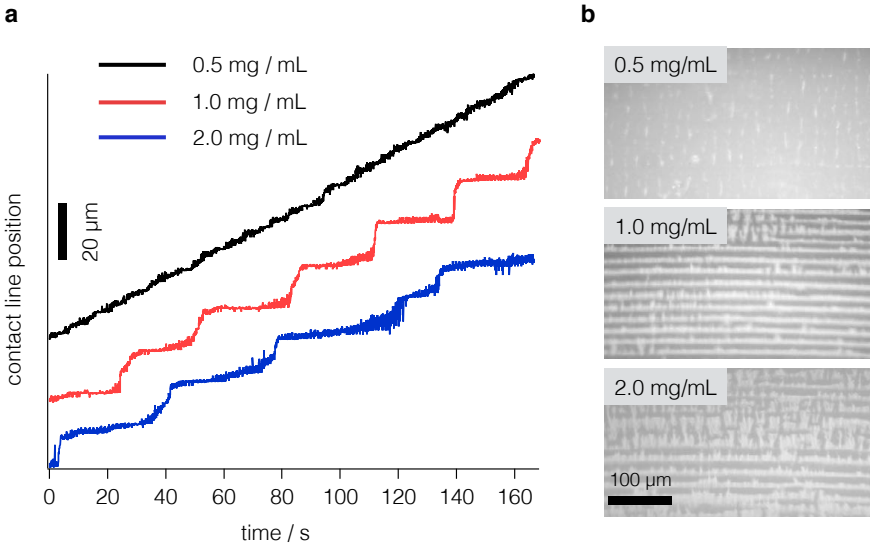


Figure 4.2: Observation of the CL motion from video sequence and deposition patterns from optical microscope. (a) The dynamics of receding CL of three different coffee concentrations obtained from analysis of video sequence. (b) Images from optical microscope show the change of patterns depending on the concentration.

Due to the scalable two-plate setup, the EISA method is improved with high coating efficiency and the evaporation rate can be further controlled by changing the capillary length of the meniscus which can be expressed as:

$$\kappa^{-1} = \sqrt{\frac{\gamma}{\rho g}} \tag{4.1}$$

where $\gamma$ is the surface tension, $\rho$ the density of the liquid and $g$ the gravitational acceleration. That means for the two-plate setup, when the distance $h$ between the substrate and cover slide is smaller than this length, the liquid can be constrained within the two plates. With the surface tension of pure water at 25℃ $\gamma = 72$ mN/m, $\rho = 1 \times 10^3$ kg/m$^3$, $g = 9.8$ m/s$^2$, we can easily estimate that the maximal distance for making capillary bridge between the two plates is about 2.7 mm. The distance range ($h < 2.7$ mm) gives us more flexibility on the two-plate setup for the EISA and provide us the opportunity to study the effect of capillary length on the process. Plano convex lenses with one flat and one outward curved face should be the ideal setup to study the distance effect because they can continuously change the capillary lengths [123].

As shown by Figure 4.3a, from the center of lens to the edge, the height of capillary bridge ranges from 0 to more than 600 µm. Due to this change of heights, the average CL velocities are measured for both pure water and 2 mg/mL coffee suspension (Figure 4.3b). They basically show a same trend that the velocity becomes higher with the smaller height. If we take the last five points of coffee suspension as an example, Figure 4.4a shows that the height decreases from 65 to 14 µm and the velocity, in turn, gradually increases as presented by the slopes of the evolution diagrams from the analysis of video sequences. Besides that, the evolution diagrams also show the change of the dynamics of CL. The regular coffee-ring effect can only happen within a certain range of the CL velocities which are further verified by the images from the optical microscope in Figure 4.4b. When the average height is around 65 µm and the corresponding velocity is 0.51 µm/s, the deposition pattern is the discontinuous stripes perpendicular to the CL (Figure 4.4b) similar with the low concentration sample in the two-plate setup (Figure 4.2b). When the velocity increases to 0.6-0.7 µm/s, the stripe pattern appears. That means the evolution of CL follows the pinning and depinning process. The red and green curves in Figure 4.2b show the typical "step" evolution but the widths of the steps become smaller when it comes to higher velocity and finally result in the straight line with the height around 10-20 µm. On the relative optical images, the pattern of deposition with high velocities is almost entirely vanished and

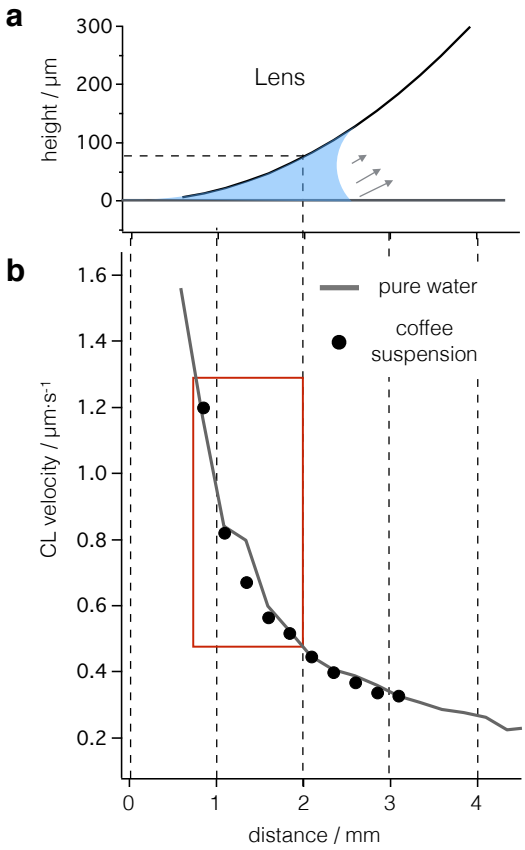


Figure 4.3: The velocity of the CL under the lens setup. (a) The curve of lens edge. The height values are calculated by the distance from the center and the known curvature radius of the lens. (b) The measured velocities of the CL dramatically increase at small bridge heights.

only a homogeneous film remains (Figure 4.4b).

It is now obvious that the EISA deposition here is very sensitive to both particle concentration and CL velocity. To make the repeated coffee-ring effect happen and regular stripe pattern arise, the concentration should be within a certain range around 1-2 mg/mL and the CL velocity 0.6-0.7 µm/s. But the question is why that happens? There is a traditional and simple

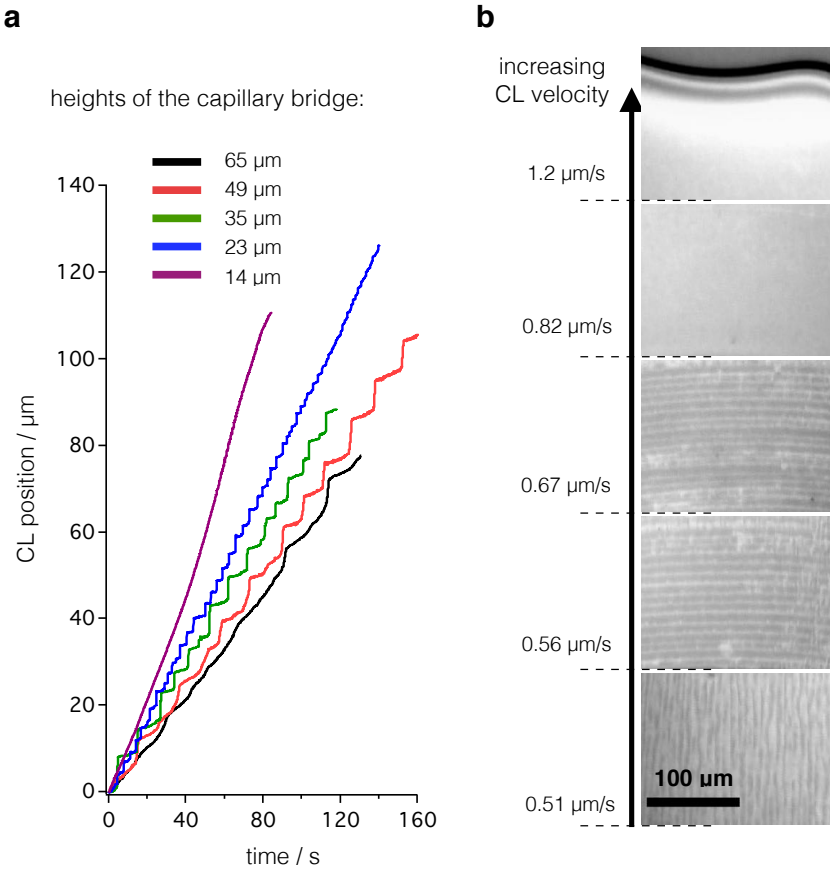


Figure 4.4: (a) The *in situ* observation of the CL motion by optical microscope from the last five stages marked in Figure 4.3b. (b) The optical micrographs of the five different stages with increasing average CL velocities from bottom to top.

explanation for this particular phenomenon which is called the "stick-slip" model [40, 124, 125].

In contrast to the equilibrium contact angle ($\theta_0$) from the Young's equation (see eq 2.1), the contact angle concerning the wetting hysteresis here should be considered as dynamic. If we measure the contact angle while the volume of the drop is increasing and the contact line (CL) is still pinned, we get

the advancing contact angle $\theta_a$, which means the CL has the trend to move advance. On the other hand, when it comes to the evaporation situation and the CL get pinned, what we measure should be the so called receding contact angle $\theta_r$. As illustrated schematically by Figure 4.5, an analogy of this situation is that when the solid substrate tilts slightly, gravity causes the contact angle on the downhill side to increase while the contact angle on the uphill side decreases. Before the drop rolls off, the two pinning contact lines show the advancing and receding contact angles respectively and obviously $\theta_r < \theta_0 < \theta_a$.


Figure 4.5: The schematic of equilibrium contact angle ($\theta_0$) on a flat substrate, advancing ($\theta_a$)and receding ($\theta_r$) contact angles on an inclined substrate.

The drop, as a spherical cap depicted in Figure 4.6a, is first at equilibrium state in accordance with the Young equation (eq.2.1) but keeps losing the liquid due to the evaporation. As long as the CL get pinned, the initial radius remains $R_0$ and the equilibrium contact angle $\theta_0$ decreases as well as the height of the drop h (Figure 4.6b). The capillary force, which pulls the liquid inward, builds up and eventually becomes larger than the pinning force. The equilibrium now is broken. $\theta_0$ has decreased to $\theta_r$ and the CL jumps to a new position where it subsequently gets pinned again due to the friction force from the surface roughness that is probably enhanced by the sufficient deposition.

In terms of the thermodynamics [126], the Gibbs free energy of the drop, G, only due to interfacial free energy [40, 127], could be written as

$$G = \gamma_{\mathrm{LG}} \cdot \frac{2\pi R^2}{1+\cos\theta} + \pi R^2 \left(\gamma_{\mathrm{SL}} - \gamma_{\mathrm{SG}}\right) \tag{4.2}$$

If we use the Young equation here, it yields:

$$G = \gamma_{\mathrm{LG}} \cdot \pi R^2 \left(\frac{2}{1+\cos\theta} - \cos\theta_0\right) \tag{4.3}$$

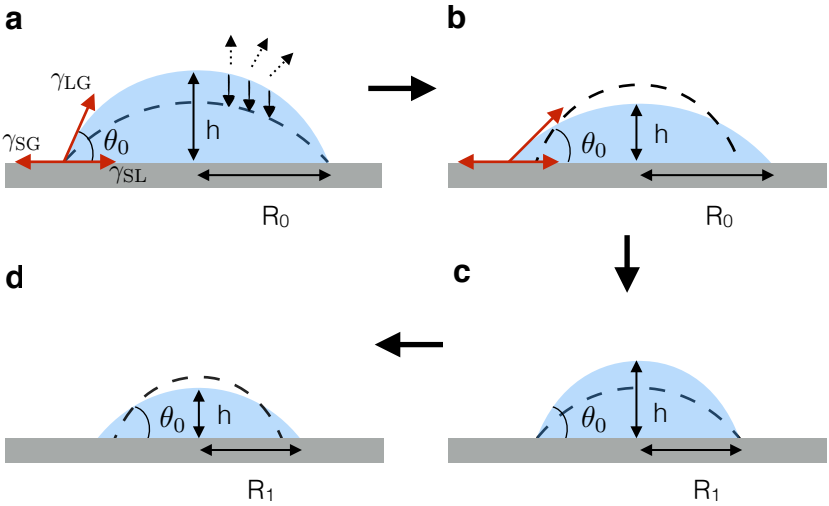


Figure 4.6: Schematic representation of "stick-slip" behavior of a drop during the evaporation. The solid light blue color shows the shape of drop at the moment and the dash lines depict the trend of the shape toward next steps. (a) is the initial state when the evaporation begins. (b) The drop volume and contact angle diminishes but the radius remains. (c) When a lower limit of contact angle is obtained, the CL jumps to a new position because the capillary force outweighs the pinning force. Then drop returns to the equilibrium state as (a) with same $\theta_0$ but shorter radius. (d) The process of (b) is repeated.

If it is assumed that the jump occurs sufficiently rapidly, the volume of these two states can be considered as constant. Therefore, for a given volume, there is a $R_0$ corresponding to $\theta_0$, but just before this thermodynamic equilibrium state, there exists a situation with $R = R_0 + \Delta R$ and $\theta = \theta_0 + \Delta\theta$ when the CL is going to jump immediately (for the evaporation here, the $\Delta R$ is positive and $\Delta\theta$ is negative).

By Taylors theorem, the excess free energy $\Delta G = G(R) - G(R_0)$ is given by

$$\Delta G = \Delta R \left[\frac{\partial G}{\partial R}\right]_{R=R_0} + \frac{(\Delta R)^2}{2}\left[\frac{\partial^2 G}{\partial R^2}\right]_{R=R_0} + O\left[(\Delta R)^3\right] \qquad (4.4)$$

as described by the ref [40], where $[\partial G/\partial R]_{R=R_0} = 0$ due to the equilibrium

state. From the eq 4.3, we can get [124]:

$$\Delta G \approx \gamma_{\mathrm{LG}} \pi \sin^2 \theta_0 (2 + \cos\theta_0)(\Delta R)^2 \tag{4.5}$$

If we consider the length of the CL, the average excess free energy per unit length is

$$\Delta \tilde{G} \approx \frac{\gamma_{\mathrm{LG}} \sin^2 \theta_0 (2 + \cos\theta_0)(\Delta R)^2}{2R} \tag{4.6}$$

Now it is clear that if there is no pinning along the CL, $\Delta G$ will keep zero, as well as the $\Delta R$ which means the CL is moving continuously. But when the CL is pinned and $\Delta R$ is larger enough to overcome a potential energy barrier $U$ per unit length of the CL, the "slip" happens. For the constant drop volume ($W_c$) :

$$W_c = \frac{\pi R^3}{3 \sin^3 \theta} (1 - \cos\theta)^2 (2 + \cos\theta) \tag{4.7}$$

where by derivative, $\theta$ and $R$ can be associated as [40]

$$\frac{\mathrm{d}\theta}{\mathrm{d}R} = \frac{-\sin\theta(2 + \cos\theta)}{R} \tag{4.8}$$

So finally, the equation 4.6 could also been written with the $\Delta\theta$:

$$\Delta \tilde{G} \approx \frac{\gamma_{\mathrm{LG}} R (\Delta\theta)^2}{2(2 + \cos\theta_0)} \tag{4.9}$$

It is obvious that when the CL gets pinned, the system is not in equilibrium and an energy barrier prevents the continuous movement of the CL. During the evaporation ($\Delta\theta < 0$), when the value of $\Delta\theta$ decreases and make the $\Delta\tilde{G}$ exceeds the energy barrier, depinning happens. Hence there is a critical contact angle value that determines the depinning moment. Now if we review the patterns made by the real coffee, it seems clear that the stripe pattern is formed by the repeated "stick-slip" process at appropriate coffee concentration. But when the concentration is too low to pin the CL, it moves smoothly and continuously (see Figure 4.2a). In contrast, if the concentration is too high, the probability of re-pinning will increase and the stripe spacing decrease [33], which finally can transform the regular stripe pattern to the continuous film.

As for the velocity of the CL, it changes the time interval to reach the critical contact angle because the high velocity means the enhancement of

evaporation near the CL, which is also consistence with Deegan's theory in eq.2.8. As shown by Figure 4.4a, both the jump distance and time interval between two subsequent pinnings become smaller when the velocity increases. With the same initial contact angle, a higher evaporation rate can reach the $\Delta\theta$ more quickly and consequently make pinning more frequently.

Although "stick-slip" seems to be useful to describe the process, this simple model inevitably has limitations and even fails to explain some specific phenomenon. For example, they have assumed $\theta_0$ after a jump to be the new balanced angle, but it is more likely that a metastable value of contact angle exists [40], which will be discussed quantitatively in the next section. In addition, the calculation is difficult to explain the stripe pattern on completely wetting surface ($\theta_r \sim 0$) [128] and seems to have a bad prediction for the space between the two adjacent jump lines, which also has been questioned before [38]. Most importantly, the model describes only the thermodynamics before the depinning but almost nothing about the pinning process that could be the key point to effectively control the deposition pattern. Like Deegan's analytical solution [27], pinning here is explained as "anchoring" [40] on the basis of the sessile drop geometry and thus it has been naturally considered as a precondition of the theoretical model. But according to our experimental results, we find that this assumption seems to be misleading. To further clarify all of these issues, we need more experimental data from not only careful *in situ* observation but also new angles of measurements. These refinements will be presented and discussed below with carbon nanotube suspensions and our capillary-bridge setups.

# 5 Self-assembled SWNTs thin films from aqueous suspensions

The discussion in this chapter is essentially based on our previously published paper [129]. The SWNTs/SDS suspensions are used to repeat the coffee-ring deposition as described above. Except the experiments on heating substrate, all of others, likewise, are under ambient conditions and the two-plate setup. The setup as mentioned before can evidently accelerate the evaporation rate and is suitable for the *in situ* observation to analyze the CL dynamics during the receding process by a normal optical microscope system (see Figure 5.1).

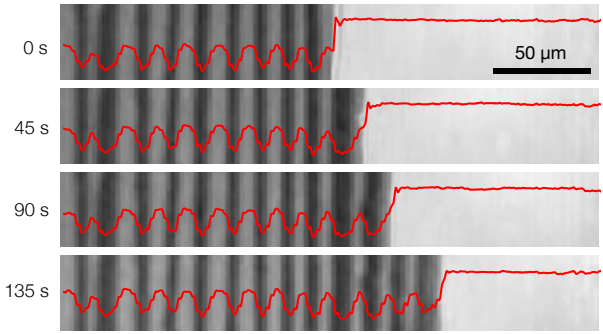


Figure 5.1: Video sequence of the advancing CL with a stripe pattern clearly emerging to the left. Adapted from publication ref. [129] by Li *et al.*

Furthermore, similar with the lens experiments, the velocity of CL can be modulated by simply changing the spacer distances between the two plates (see Figure 5.2) because of the aforementioned divergence of the evaporating flux along the meniscus. For the smallest spacer distance this leads to a CL velocity of over 2 µm/s, roughly 2 orders of magnitude higher than CL velocities reported previously [33,35] and allows the simultaneous observation and analysis in an appropriate time range.

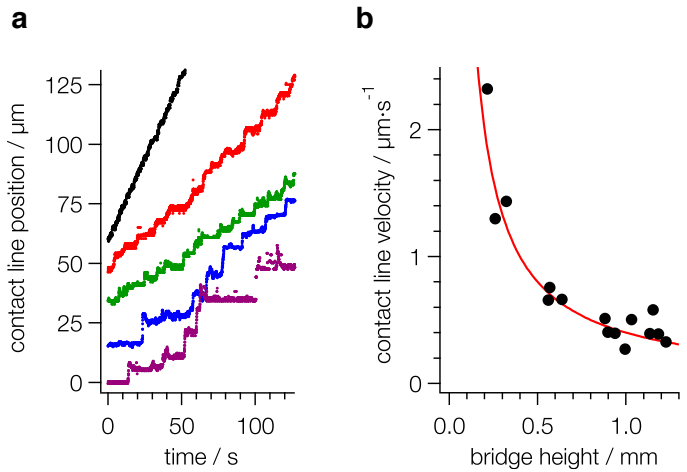


Figure 5.2: (a) CL dynamics for different capillary bridge heights indicate tat the average CL velocity increases for small capillary bridge heights (top to bottom: 0.3 mm, 0.5 mm, 0.8 mm, 1.0 mm, and 1.2 mm) (b) Measured CL velocities increase at small bridge heights due to the diverging vapor flux at the CL whose trend is similar with the results from lens setup (see Figure 4.3) Adapted from publication ref. [129] by Li *et al.*

In the first section, the concentrations of both SWNTs and surfactants are carefully changed in order to obtain different kinds of thin film patterns and meanwhile optimize the quality of the regular stripe pattern. Then the mechanism of the pinning and depinning process is elaborated and discussed from a brand-new angle. The second part will focus on two interesting phenomenon from the observations of stripe formation, breathing motion and kink behavior of the CL which reversely support our mechanism and simulation. The last section here will mainly show the results from a heating substrate to find the temperature effects on the pattern formation.

## 5.1 Structure of thin SWNTs films under ambient conditions

Well-dispersed SWNT colloids are used for the film fabrication under the two-plate setup in this section. The laboratory ambient conditions here actually are measured and recorded before each experiment. The normal room temperature is 18- 22℃, the humidity ranges from 30 % to 40 %, and the pressure is 101.3 kPa. Because the evaporation rate is sensitive to this factors, only the results within these range of conditions are shown in this section except the special comparison of the velocities of the contact line under different evaporation rates.

Direct experience from the real coffee experiment is that the concentration of solute matters during the deposition. Using the same setup (two plates with height of capillary bridge 550 µm), we first examine the effect of concentration on the fabrication. But in this suspension, there is an additional component, the SDS, which is used to disperse SWNTs in the colloid. Furthermore, the SDS concentration is highly associated with the surface tension ($\gamma$) of the solution in ambient conditions. The surface tension here, also called liquid-gas interfacial energy ($\gamma_{LG}$) in the Young equation, is basically a key factor during the "stick-slip" process because it varies the equilibrium contact angle $\theta_0$. As shown by Figure 5.3a, the surface tension of the water solution decreases when the SDS concentration increases. The CMC of SDS in pure water at 25 °C is around 8.2 mM (around 0.23 wt%). In addition, we have to consider the effect of carbon nanotubes on the surface tension in this case. Vijoya *et al.* [130] found that the surface tension isotherm almost maintains the same when the SWNT concentration is below 0.75 mg/mL (see Figure 5.3b). In all of our experiments, the highest concentration of SWNT is definitely below 0.1 mg/mL (around 4 OD) so that their effect on the surface tension can be almost neglected.

Therefore, we make the concentration gradients for both SWNTs and SDS by dialysis after the DGU process but within a certain range that SWNTs do not aggregate and SDS concentration is not far beyond the Critical Micelle Concentration (CMC). In Figure 5.4, the concentration matrix is shown with increasing [SWNTs] from bottom to top and increasing [SDS] from left to right. The SWNT concentration is here calculated from the optical density (OD) at the first exciton subband transition. The OD values then are transformed to the wt% by the the equation from Schöppler *et al.* [131]

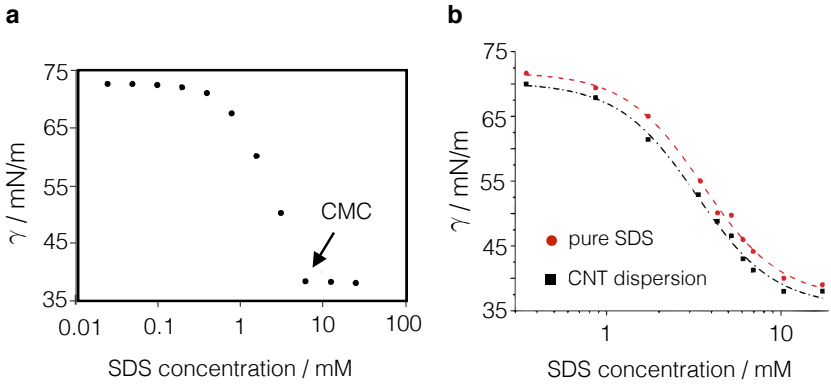


Figure 5.3: (a) Surface tension of SDS in water as a function of concentration. (b) Surface tension isotherms in water without or with 0.75 mg/mL carbon nanotubes adapted from ref. [130] by Vijoya *et al.*.

$$C_c = \frac{\Delta \cdot \mathrm{OD}}{f \cdot d} \cdot 5.1 \times 10^{-8}\ \mathrm{cm \cdot mol \cdot L^{-1} \cdot nm^{-1}} \tag{5.1}$$

where $C_c$ is the carbon atom concentration in mol/L, $\Delta$ is the Full Width at Half Maximum (FWHM) of the exciton transition in nm, $f$ is the oscillator strength of the first subband transition and $d$ is the optical path length. With a FWHM of the first subband exciton of 39 nm and oscillator strength of 0.01 per carbon atom, we thus obtain the simple relationship between the carbon atom concentration and the OD of our suspensions at 982 nm in mol/L:

$$C_c = \mathrm{OD} \cdot 0.2 \times 10^{-3}\ \mathrm{mol/L} \tag{5.2}$$

and in wt%

$$C_c = \mathrm{OD} \cdot 2.4 \times 10^{-4}\ \mathrm{wt\%} \tag{5.3}$$

As shown by Figure 5.4, the regular stripe pattern only happens within a very small range of SWNT and SDS concentrations, which means that both of them can effectively change the fabrication process and surface morphology. The SWNT films have thickness between 5 and 10 nm as determined by atomic force microscopy (AFM) (see Figure 5.5), which indicates that the film composition is a mixture of individual and bundled SWNTs. This is consistent with the scale of patterns seen in other EISA deposition [33, 132].

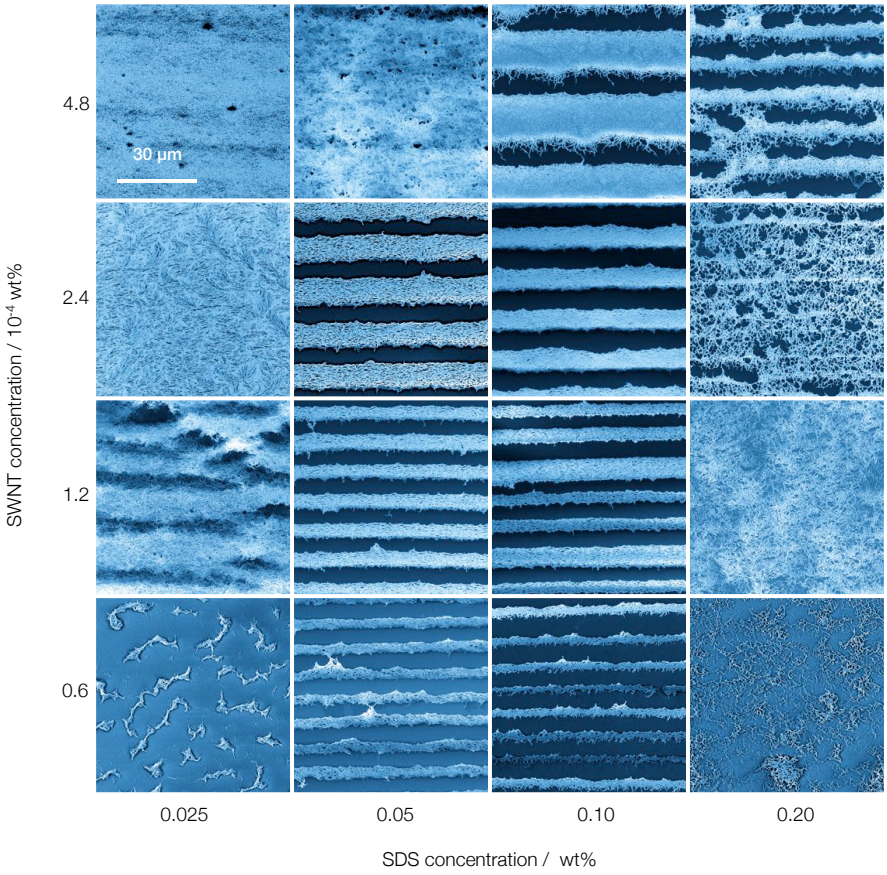


Figure 5.4: Series of SEM images for different SWNT and SDS concentrations. SWNT concentrations are given in terms of the optical density of an SWNT suspension at 982 nm for a 1 cm spectroscopy cell (the corresponding OD values from bottom to top are: 0.25, 0.5, 1.0, 2.0.). The electron beam energy used here was 0.5 kV. Adapted from publication ref. [129] by Li *et al.*.

Almost all of the samples within this concentration range have similar film thickness. A typical example and the comparison of stripes from different SWNT concentrations are given by Figure 5.5.

The degree of local ordering within these films and stripes is expected to depend primarily on the rate at which SWNTs are deposited. Local order should improve if deposition rates are low [35]. We have already discussed in the Chapter 2 that the rodlike particles like SWNT favor the parallel alignment because a larger translational entropy can be obtained [117]. Experiments by Yunker *et al.* moreover suggest that the formation of continuous films may be facilitated by capillary interactions between anisotropically shaped particles [133], which is also in accordance with the Maier-Saupe mean field theories [33,119]. General scaling arguments [66] suggest that ordering of SWNTs can be expected if rotational and hydrodynamic time scales $\tau_r = (6D_r)^{-1}$ and $\tau_h = Lv^{-1}$ become similar. Here $D_r$ is the rotational diffusion coefficient, $L$ is the average particle distance in the suspension, and $v$ is the velocity at which particles are swept to the CL. With a hydrodynamic radius of 5 nm [134,135], $D_r$ for 200 nm long SWNTs is on the order of 1 kHz, resulting in a critical hydrodynamic time scale of 0.16 ms. This imposes a limit of roughly 5 kHz on the rate at which SWNTs may self-align during deposition. Hydrodynamic forces near the CL may also facilitate self-organization. A regular stripe pattern made from $2.4 \times 10^{-4}$ wt% SWNT and 0.1 wt% SDS is shown by Figure 5.6. Both the width of stripes and the stripe spacing are about 8 µm. With 10000×magnification, we can see the alignment of tubes within a stripe. Most of the tubes lie within 10-20° of each other along the whole stripe, which is no doubt better than the spinning coating methods (71% tubes lying within 20° of one another [136]) but not as good as the similar vertically EISA methods (all tubes lying within 5° of one another) [33]. That can be explained by the discussion we have above. With approximately 1 µm/s CL velocity in our setup and conditions, we can make the as large as 1 $cm^2$ deposition region within 3 h, but the vertical one in a desiccator needs nearly 3 days for the entire evaporation. The high evaporation rate concerning on the particle moving velocity could be the main reason for the inadequate alignment.

With an extended concentration range shown by Figure 5.7, we further divided the surface morphologies into four major types: continuous, holey, striped and spotty (see Figure 5.7a from left to right). In Figure 5.7b, we draw a schematic map indicating the ranges of concentrations for these four different morphological types. No stripes are observed for SDS concentrations exceeding the CMC of 0.23 wt %.

The striped structure is found only for deposition from SWNT suspension

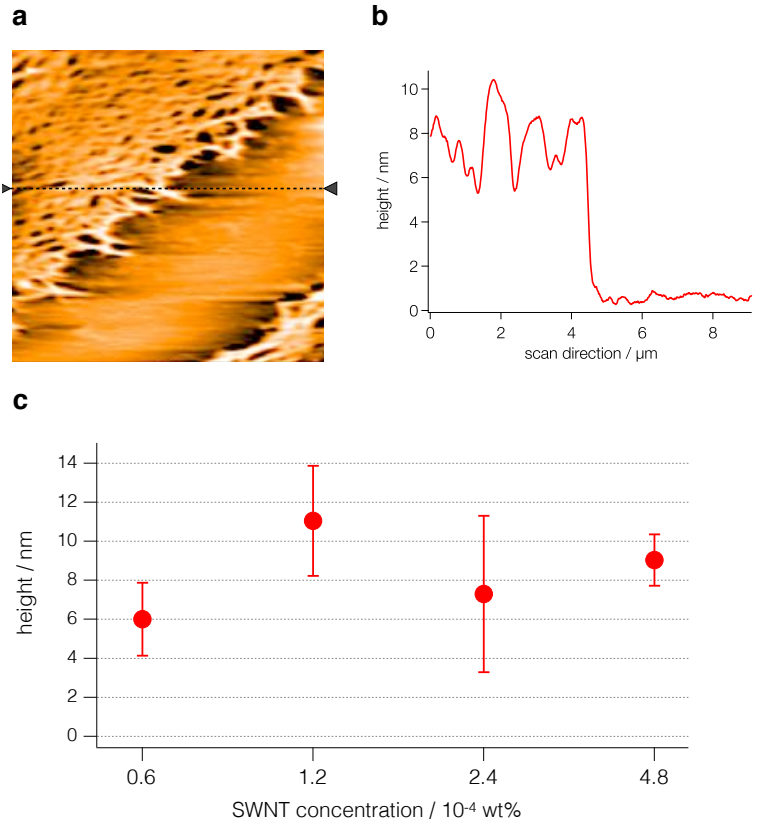


Figure 5.5: (a) A typical AFM image and (b) cross sectional profile of a stripe edge from the sample [SWNT] = $2.4 \times 10^{-4}$ wt% (1 OD) and [SDS] = 0.1 wt%. (c) The average stripe thickness with increasing [SWNT] from 0.6 to $4.8 \times 10^{-4}$ wt% but a fixed [SDS]=0.1 wt%. Adapted from publication ref. [129] by Li *et al.*

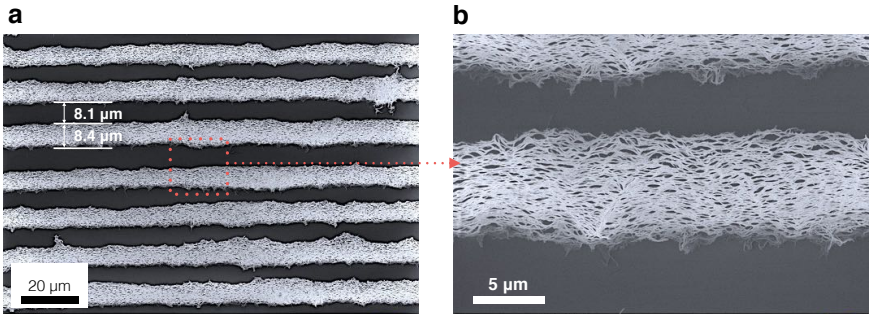


Figure 5.6: (a) SEM image of the nanotube stripe pattern from [SWNT] = $2.4\times10^{-4}$ wt% and [SDS] = 0.1 wt%. (b) SEM image of nanotubes within a stripe zoomed in from (a).

with concentrations exceeding $\sim 0.3 \times 10^{-4}$ wt% (0.12 OD). The range of SDS concentrations over which striped phases are observed is likewise limited to values between 0.05 and 0.15 wt %, shifting to slightly higher SDS concentrations as the SWNT concentration increases.

With relatively low SDS but high SWNT concentrations, homogeneous thin films can be fabricated. However, if the SWNT concentrations are lower than 0.12 OD, the contact line will hardly get pinned and the random "islands" pattern appears. On the other hand, slightly more SDS will make the stripe pattern blur at first by inserting many entangled tubes between them. If the SDS concentration keeps increasing, with enough SWNTs, the film will be formed but not as homogeneous as that in the low SDS range. Moreover, when the SWNTs concentration is also low, tubes are not be able to gather as "islands" but spread more loosely on the surface.

Then in order to further clarify the effects of the SDS, we maintain the SWNT concentration as $2.4\times10^{-4}$ wt% and change SDS concentration gradually. The mechanism of stripe formation is further investigated by comparison of SEM images (Figure 5.8a) with automated video analysis of CL dynamics as obtained from optical images (Figure 5.8b).

The dynamics shown in Figure 5.8b at different surfactant concentrations, for example, show continuous CL movement at the lowest SDS concentration of 0.025 wt %, in agreement with the homogeneous films observed in SEM images. At intermediate SDS concentrations the CL dynamics feature steps that are characteristic of the striped phase. At the highest SDS concentration of 0.20 wt % the CL dynamics in Figure 5.8b suggest that CL jumps still occur

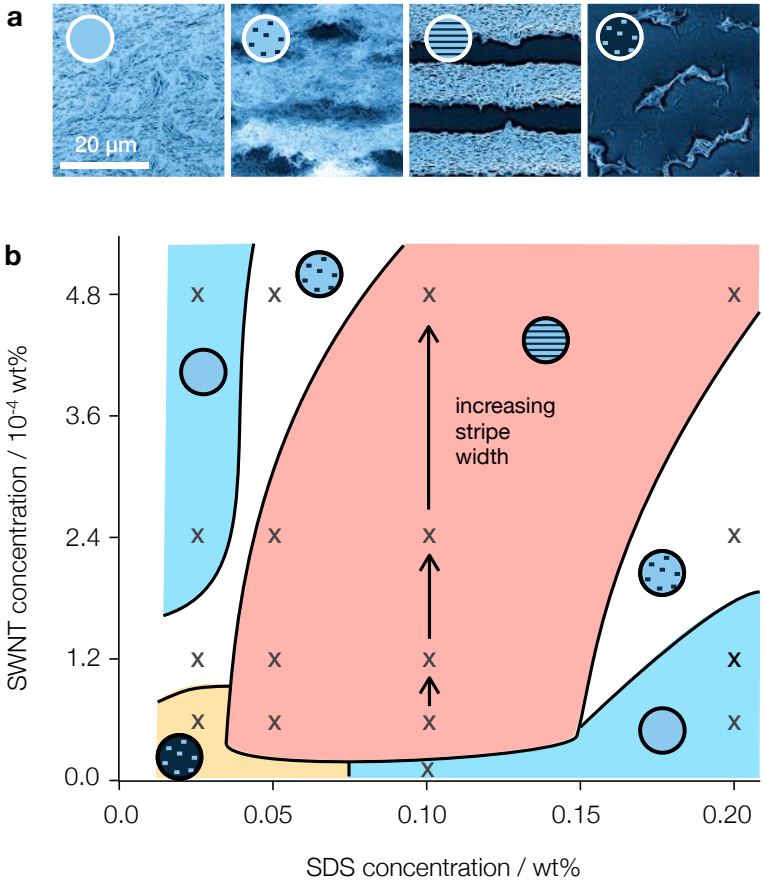


Figure 5.7: Structural phases observed during self-assembly of SWNT coffee stains. (a) SEM images with overview of observed phases: continuous, holey, striped, and spotty. (b) Schematic structural diagram as a function of SWNT and SDS concentrations obtained for a capillary bridge height of 550 µm and an average CL velocity of around 0.8 µm/s. Crosses mark conditions for which SEM images have been shown by Figure 5.4. Adapted from publication ref. [129] by Li *et al.*

but become more frequent and less regular. The latter effect is practically impossible to discover from SEM images alone because randomly entangled SWNTs start to fill the spacing of stripes.

Within the stripe phases, like the results of the real coffee ring from the dropcasting (see Figure 4.1), the most obvious trend is a gradual increase of the pitch from 9.5 µm to 24 µm, a concomitant increase of the stripe width from 2 µm to 15 µm and a increase of average pinning time from 10 s to 48 s with increasing SWNT concentration. The spacing between lines of 8 µm on the other hand remains roughly constant.

The combination of SEM images and video analysis of CL dynamics is shown in Figure 5.9 for an SDS concentration of 0.10 wt %. The dependence of stripe pitch, width, spacing and pinning time on SWNT concentration is summarized in Figure 5.10.

If one follows the traditional "stick-slip", a smaller spacing between stripes would be naturally predicted when it comes to high SWNT concentration because more SWNTs implies easier pinning, leading to closely spaced nanotube rows [33,35]. However, our experiments show the roughly constant "slip" distance with different SWNT concentration and the similar phenomenon was also verified by Watanabe *et al.* [38] who used the similar convective assembly method but with silica spheres and deposition on completely solvophilic substrates. Here, we are going to use the spacing of stripes as the starting point to build our own model including the geometry of meniscus and the mechanism of the stripe formation.

The spacing between stripes can be analyzed by assuming that the advancement of the CL is sudden (within about 0.5 s, from the CL dynamics observation) and not associated with any significant change of volume of the capillary bridge under our two-plate geometry. So we can calculate the CL position relative to its position at 90° contact angle using a circular meniscus cross section between the plates (see Figure 5.11). For the parallel plate geometry with spacing distance $d$, this yields

$$x = \frac{d}{4\cos^2\theta}\left(\frac{\pi}{2} - \theta - \sin\theta\cos\theta\right) \tag{5.4}$$

As schematically illustrated by Figure 5.11, the contact angle increases when the CL moves from in our case, relatively high energy surface (SWNT covered) to the low energy surface (bare silicon wafer), the contact angle changes from $\theta_-$ into $\theta_+$. $\Delta\theta$ hence can be directly related to the CL slip distance $\Delta x$

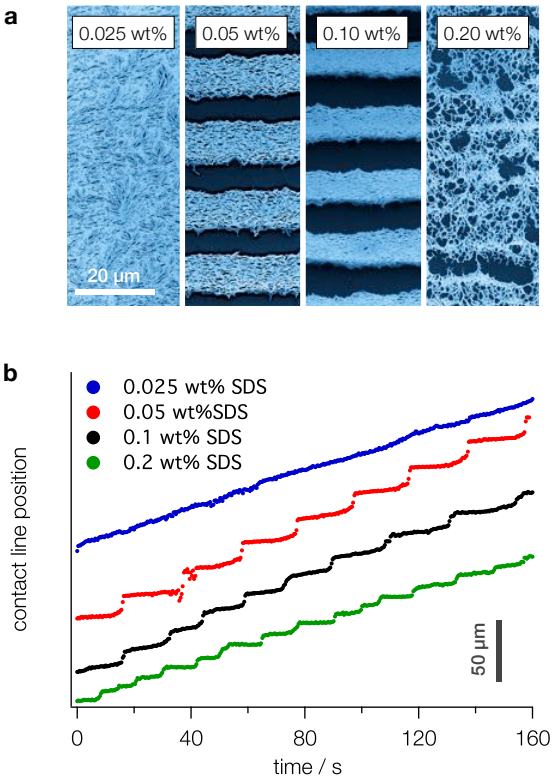


Figure 5.8: Dependence of SDS concentration from SEM images and video sequences. (a) Dependence of the film character on the SDS concentration for a fixed SWNT concentration ([SWNT] = $2.4\times10^{-4}$ wt %) as observed by SEM. (b) CL dynamics for films grown under the same conditions as those in (a) as obtained from analysis of video sequences taken during film growth. Adapted from publication ref. [129] by Li *et al.*

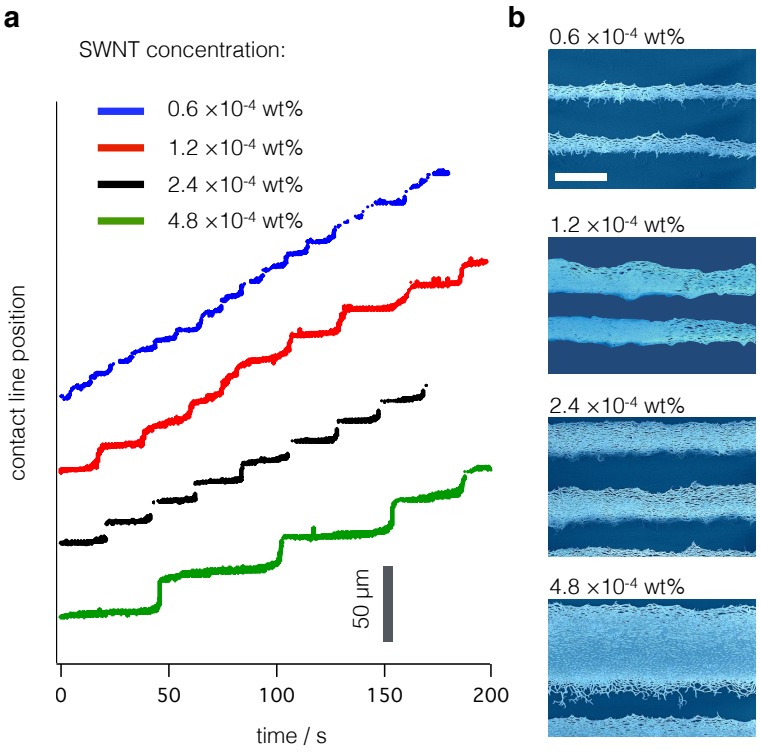


Figure 5.9: Dependence of SWNT concentration from SEM images and video sequences. (a) CL dynamics for films grown for a fixed SDS concentration ([SDS] = 0.10 wt %) but increasing [SWNT]. (b) The corresponding SEM images under the same conditions as those in (a). The scalebar here is 10 µm.

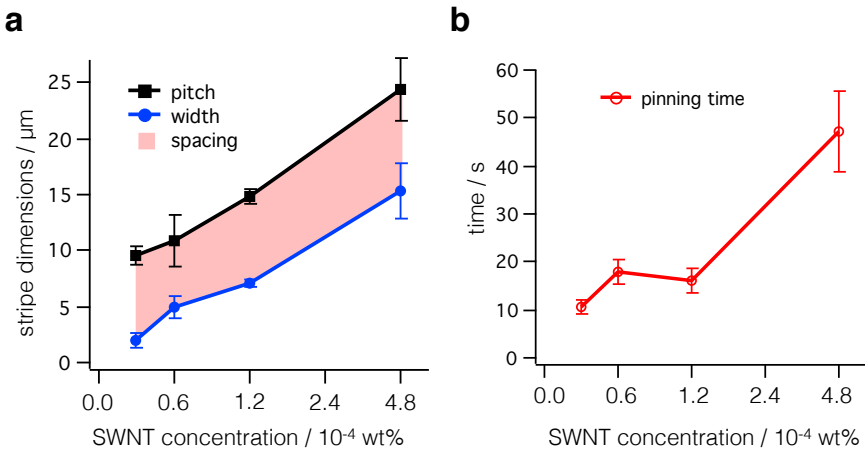


Figure 5.10: Stripe dimensions of constant SDS concentration (0.10 wt %). (a) Stripe width, pitch and spacing as a function of SWNT concentration. (b) The variation of pinning time for different SWNT concentrations.

$$\Delta x = \frac{d}{4}\frac{\partial}{\partial\theta}\left\{\frac{\pi/2 - \theta - \sin\theta\cos\theta}{cos^2\theta}\right\}\Delta\theta \tag{5.5}$$

$$\Delta x = -\frac{d\cdot[(\pi - 2\theta)\tan\theta - 2]\sec^2\theta}{4}\Delta\theta = d\cdot f(\theta)\Delta\theta \tag{5.6}$$

The function $f(\theta)$ here is shown in Figure 5.12. For the receding contact angle in the vicinity of 15° as measured for the bare substrate, this becomes

$$\Delta x = -d\times 0.0061\times\Delta\theta \tag{5.7}$$

where with the average slip distance of $\Delta x \approx 8\ \mu m$ and $d = 550\ \mu m$, the contact angle difference between the bare and SWNT-covered surfaces are only around 2.4°.

Now with the analysis here, it is clear that the slip distance depends on the change of contact angle which is due to the interfacial energy contrast between SWNT-covered and bare surface. If the $\Delta\theta$ is fixed, the slip distance will maintain roughly constant. A similar discussion was claimed by Xu *et al.* for a sphere-on-flat geometry [132] which is same with the lens setup we used for the measurement of CL velocity. Besides, another research found that the

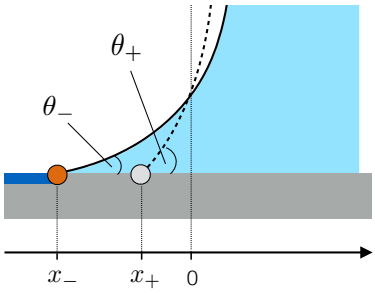


Figure 5.11: Schematic illustration of the geometry used for calculation of slip distances. The values $\theta_-$ and $\theta_+$ as well as the CL positions $x_-$ and $x_+$ refer to the contact angles and CL positions before and after and isochoric CL slip event.

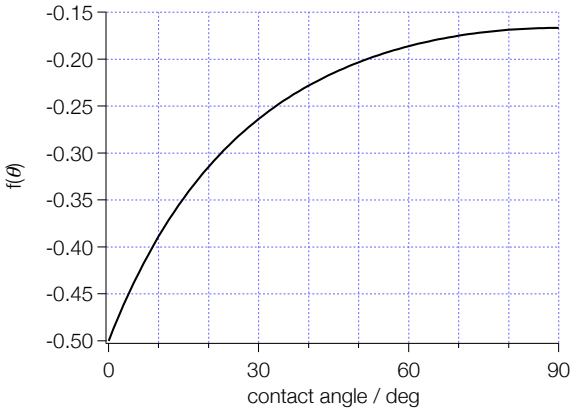


Figure 5.12: The function $f(\theta)$ for contact angle between 0 and 90°.

stripe spacing does not seem to depend directly on particle concentration but on the thickness of the stripes [38], which is still consistent with our results because according to the AFM measurements, the films and stripes of SWNTs from different concentrations have very similar thickness in our experimental conditions (see Figure 5.5c).

Furthermore, the same analysis can help us explain the range of SDS concentrations for which stripes exist. From the "stick-slip" model, the so-called pinning of the CL is generally considered to be a prerequisite for stripe formation and is assumed to be initiated by deposition of nanoparticles at the CL. The specific circumstances under which pinning may occur are simply attributed to the friction from surface roughness. Next, we will discuss the dynamical effect that SWNT deposition has on the contact angle and CL position.

The discussion of the slip distance has already shown that SWNT-covered surface areas must have a higher interfacial energy, which gives rise to a 2-3° smaller contact angle. In the schematic illustration of meniscus on Figure 5.11, it is clear that such a sudden decrease of the contact angle would push the CL further away from the capillary bridge. Evaporation on the other hand will simultaneously pull the CL toward the center of the capillary bridge. The onset of SWNT deposition is thus expected to lead to a dynamical interplay between decreasing contact angle and evaporation, both driving the CL in opposite directions. If the decrease of the contact angle due to SWNT deposition is sufficiently fast, it can offset the effect of solvent evaporation and decrease the CL velocity to zero.

Therefore, what is commonly referred to as pinning should be thought of as a dynamical process. The critical rate $\mathrm{d}\theta/\,\mathrm{d}t$ at which the contact angle must decrease to stop the receding CL motion can be well described under the two-plate geometry as illustrated by Figure 5.13. In Figure 5.13a, we can easily calculate the volume change ($\Delta V_{\text{evaporation}}$) due to the contact angle decrease (from $\theta_+$ to $\theta_-$) by its cross section:

$$\Delta V_{\text{evaporation}} = \frac{d^2}{4} \cdot \frac{(\pi - 2\theta)\tan\theta - 2}{\cos^2\theta} \cdot \Delta\theta \cdot L \tag{5.8}$$

where $L$ is the length of the CL. As illustrated by Figure 5.13b, the evaporated volume could also be expressed by the average velocity ($V_{av}$) of CL from the slope of the step diagram and the time interval:

$$\Delta V_{\text{evaporation}} = V_{av} \cdot d \cdot \Delta t \cdot L \tag{5.9}$$

Then within relatively small $\Delta\theta$, from the two equations above we obtain the critical rate:

$$\frac{\mathrm{d}\theta}{\mathrm{d}t} \leq \frac{57.3^\circ}{g(\theta)} \cdot \frac{V_{av}}{d} \tag{5.10}$$

where $g(\theta) = (2\cos^2\theta)^{-1}\{(\pi/2 - \theta)\tan\theta - 1\}$ is a geometric function with a value of *ca.* -0.35 for the range of contact angle relevant to this study. 57.3° is only used to transfer the unit of contact angle value from rad to degree. If we bring in $d = 550$ µm and $V_{av} = 0.8$ µm/s, $\mathrm{d}\theta/\mathrm{d}t$ will be around -0.24°/s, which means the contact angle decrease should at least reach this rate for a pinning state of CL.

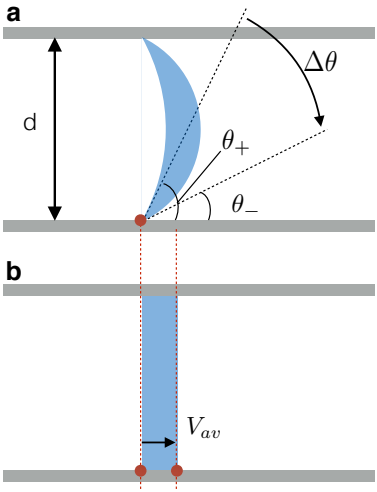


Figure 5.13: Schematics for contact angle dynamics of pinning. (a) The volume change by evaporation from the geometry of pinning state when the contact angle decreases from $\theta_+$ to $\theta_-$. (b) The corresponding isovolumetric process for the continuously moving CL calculated from the average CL velocity.

Now dynamical pinning and the associated formation of stripes can be directly related to the rate of change of the contact angle on SWNT-covered regions. Therefore for this rate to be sufficiently large, there must be a sufficiently high SWNT concentration as well as a sufficiently high contrast of interfacial tensions between bare and SWNT-covered interface regions. Ex-

perimentally, the critical SWNT concentration for which the above criterion is fulfilled was found to be approximately $0.3 \times 10^{-4}$ wt% (see Figure 5.7b). Besides, the results of real coffee experiments under lens setup in the last chapter can also be interpreted here. At a constant coffee concentration, the contrast of interfacial tension remains. When the capillary bridge becomes further smaller after the stripe pattern emerges, the evaporation rate increases, the slip distance at first decreases evidently and finally disappears (see Figure 4.4) due to the competition between the rates of evaporation and contact angle decreasing.

In addition, the model could further help us explain the effect of SDS, especially the absence of stripes at higher and at lower SDS concentrations. As illustrated in Figure 5.14a, we expect that a larger concentration of SDS should cover on the SWNT surface due to its hydrophobic character, irrespective of the bulk SDS concentration. A small number of SDS molecules will also assemble onto the hydrophilic substrate whereas the concentration is expected to be lower than that on the SWNT surface. In Figure 5.14b, we qualitatively illustrate the difference of interfacial tensions between the bare and SWNT-covered surface and their dependency on the change of SDS concentration. We speculate that an initial increase of the contrast between the interfacial tensions defines the minimum value for the SDS concentration where the stripe pattern can be observed. Then eventually a decrease of this contrast at high SDS concentration determines the other boundary. From the discussion of the dynamical contact angle in equation 5.10, we know that this concentration range of SDS could also enlarge or shrink depending on the evaporation rate, capillary length and CL velocity. But no change in the contrast of interfacial tensions is expected for SDS concentration beyond the CMC where the formation of stripe pattern is supposed to be suppressed.

To further explore the characteristics of stripe formation, we focus on CL dynamics as obtained from simple total energy calculations. This discussion is based on the simulation of the dependence of the total interfacial energy $E_{\text{interfaces}}$ on time $t$ and CL position $x$.

$$E_{\text{interfaces}}(x) = E_{\text{GS}} + E_{\text{SL}} + E_{\text{LG}} \tag{5.11}$$

The three contributions of different interfacial energies to equation 5.11 are gas-solid ($E_{\text{GS}}$), solid-liquid ($E_{\text{SL}}$) and liquid-gas ($E_{\text{LG}}$) respectively, which can be calculated using the difference of contact angles on bare and SWNT-covered substrate regions. As for the gas-solid component, we have:

$$E_{\text{GS}} \propto \gamma_{\text{GS}} \cdot x \tag{5.12}$$

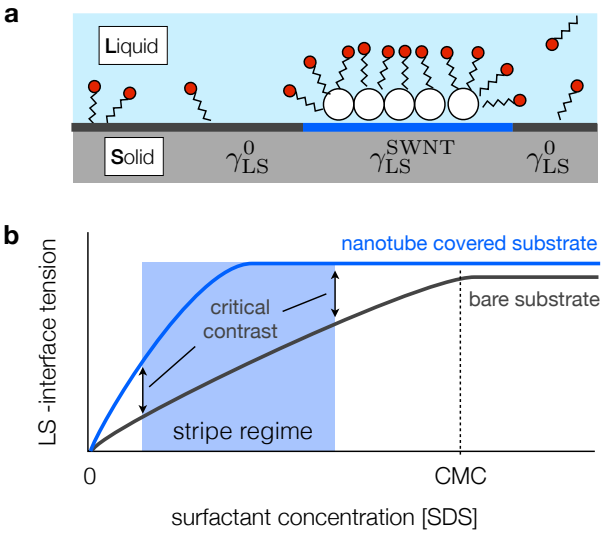


Figure 5.14: (a) Schematic illustration of surfactant coverages on bare and SWNT-covered surface respectively. (b) Schematic illustration of SDS-induced changes of interfacial tensions for bare and SWNT-covered regions. Adapted from publication ref. [129] by Li *et al.*

where $\gamma_{GS}$ is the gas-solid interfacial tension.

The contribution of the liquid-gas interface ($E_{LG}$) can be calculated using the length of half of the curved meniscus between the plates and the liquid-gas interfacial tension ($\gamma_{LG}$):

$$E_{LG} \propto \frac{\pi/2 - \theta}{2\cos\theta} \cdot d \cdot \gamma_{LG} \tag{5.13}$$

where we can use the $\theta$ related function $S(\theta)$ to simplify the equation 5.13 into

$$E_{LG} \propto S(\theta) \cdot d \cdot \gamma_{LG} \tag{5.14}$$

As for the $E_{SL}$ part, the solid-liquid interfacial tension ($\gamma_{SL}$) is not homogeneous due to the formation of the particles deposits and the integration yields

$$E_{\mathrm{SL}} \propto \int_{x_0}^{l} \gamma_{\mathrm{SL}}(x)\,\mathrm{d}x \tag{5.15}$$

Next, in order to build a new function to describe the solid-liquid interfacial interaction with $x$ and $\theta$, we have to simply modify the Young equation( $\gamma_{\mathrm{SG}} - \gamma_{\mathrm{SL}} - \gamma_{\mathrm{LG}}\cos\theta = 0$, see also equation 2.1):

$$\gamma_{\mathrm{SL}} = \gamma_{\mathrm{SG}} + \gamma_{\mathrm{LG}} - \Gamma \tag{5.16}$$

where $\Gamma/\gamma_{\mathrm{LG}} = (1+\cos\theta)$ and it is implied that we have $\theta < \pi/2$ for $\Gamma/\gamma_{\mathrm{LG}} > 1$ (wetting) and $\theta \geq \pi/2$ for $\Gamma/\gamma_{\mathrm{LG}} \leq 1$ (non-wetting). $\Gamma/\gamma_{\mathrm{LG}}$ here can be used to describe the adhesion force of the liquid on the solid substrate. For an inhomogeneous solid-liquid interface $\Gamma$ naturally becomes a function of position on the substrate near the contact line $\Gamma = \Gamma(x)$.

The dependence of interfacial energies on contact angle $\theta$ and time $t$ is then given by

$$\begin{aligned} E_{\mathrm{interfaces}}(x) \propto K(\theta)\cdot\frac{d}{4}\cdot\gamma_{\mathrm{SG}} + S(\theta)\cdot d\cdot\gamma_{\mathrm{LG}} \\ + \int_{0}^{(V_{av}t - \frac{d}{4}K(\theta))} [\gamma_{\mathrm{SG}} + \gamma_{\mathrm{LG}} - \Gamma(x)]\,\mathrm{d}x \end{aligned} \tag{5.17}$$

Here $V_{av}$ is the average velocity of the CL, $S(\theta)$ has been introduced by equation 5.14 and the function $K(\theta)$ is modified from equation 5.4 as

$$K(\theta) = \frac{1}{\cos^2\theta}\left(\frac{\pi}{2} - \theta - \sin\theta\cos\theta\right) \tag{5.18}$$

Finally, we should establish the relationship between $\Gamma(x)$ and time $t$. Here we use the following differential equation:

$$\frac{\mathrm{d}\Gamma(x)}{\mathrm{d}t} = k\cdot s(x)(\Gamma_{\mathrm{SWNT}} - \Gamma(x))[\mathrm{SWNT}] \tag{5.19}$$

where $k$ is a fixed rate constant and $s(x)$ is a sticking function. The term $(\Gamma_{\mathrm{SWNT}} - \Gamma(x))$ allows the SWNT coverage to saturate at a value associated with the interfacial tension $\Gamma_{\mathrm{SWNT}}$. The equation above determines the rate at which the interfacial tension at the position of the contact line grows from its bare surface value $\Gamma_0$ towards the saturation value of the SWNT-covered surface $\Gamma_{\mathrm{SWNT}}$.

During the simulation, we set the dependence of $s(x)$ on $x$ as:

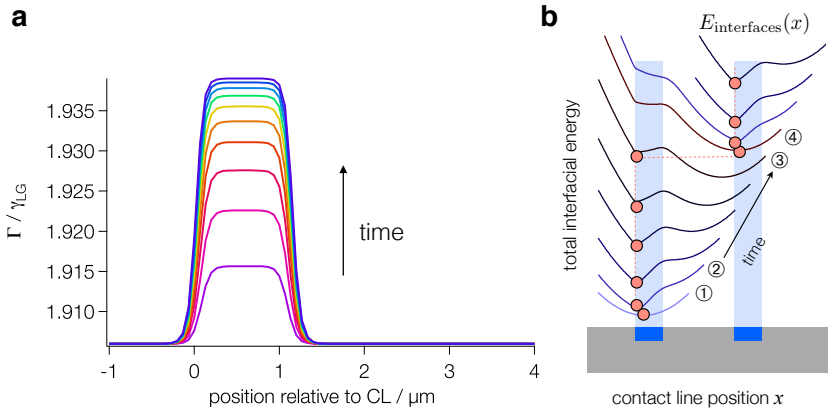


Figure 5.15: Simulation for the interfacial energy and CL dynamics. (a) Schematic evolution of the value of $\Gamma(x)/\gamma_{\text{LG}}$ as a function of time for a pinned CL. (b) Waterfall plot of calculated CL dynamics obtained from the development of interfacial energy contributions during film growth. Adapted from publication ref. [129] by Li *et al.*

$$s(x) = \begin{cases} 1 & x_{\text{CL}} < x < x_{\text{CL}} + w \\ 0 & \text{elsewhere} \end{cases} \tag{5.20}$$

which means that the simulation only focus on the deposition of SWNTs in a region of width $w$ to the liquid side of the CL. Here the width of the deposition between 1 and 2 µm is obtained from the smallest stripe widths observed in our experiments. In Figure 5.15a, schematic evolution of the $\Gamma(x)/\gamma_{\text{LG}}$ for a pinned CL indicates the change of the interfacial tension within the range of $w$ as a function of time. Here the contact angle on the bare and fully SWNT-covered surface were assumed to be 20° and 25° respectively. A similar sticking function with slightly broadened edges is used then for the normal CL dynamics comparable with our experimental results.

In Figure 5.15b, the local minimum of the interfacial energy $E_{\text{interfaces}}(x)$ qualitatively shows the behavior of CL dynamics as the function of time. During the early deposition of SWNT, the $E_{\text{interfaces}}$ develops a local minimum at the region close to the edge of a stripe. But the minimum soon moves a little outward (point 1 and 2 in Figure 5.15b) and maintains there as a stable pinning contact line. While the deposition of SWNT continues and capillary

force increases, the local energy minimum becomes metastable and the CL slips to an new position (point 3 and 4 in Figure 5.15b). From there the process repeats itself.

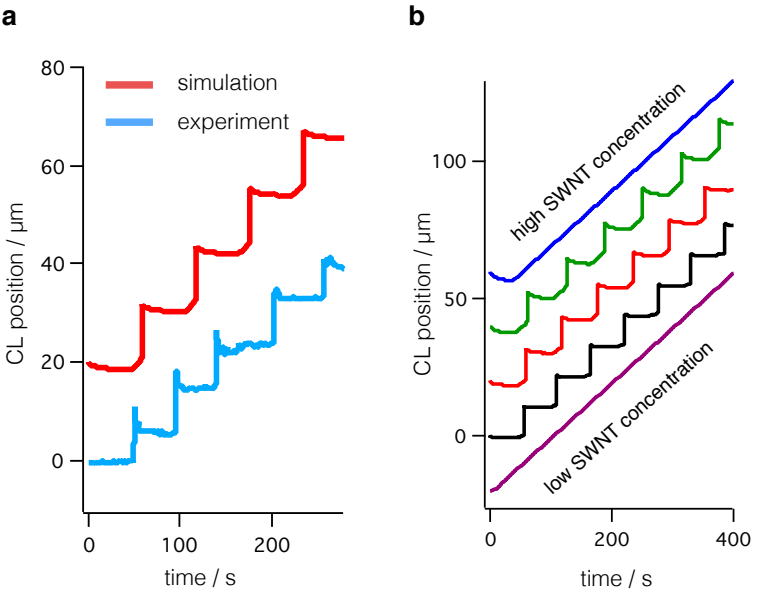


Figure 5.16: (a) Comparison between the simulation and experimental results of the CL dynamics. The experimental curve is obtained from the suspension with [SWNT]=2.4 $\times$ $10^{-4}$ wt% and [SDS]=0.1 wt% under two-plate setup with 1000 µm capillary bridge. (b) Waterfall plot. CL dynamics obtained from simulations at low, intermediate, and high SWNT concentrations qualitatively reproduce experimental observations.

The complete simulation results are shown by Figure 5.16. The simulation shows a constant slip distance which is comparable with the experimental result on the similar scale. Moreover, by modulating the SWNT concentrations, we obtain the same trend with the experimental observations (see Figure 5.16b). However, the magnitude of the increase in stripe widths routinely falls short of experimental observations irrespective of the parameters used in the simulation. It suggests that the strains from capillary force do not appear to rise as quickly as predicated by the simulation.

What's more, there are several very interesting phenomenon in our obser-

vations. One of them is a subtle breathing motion of the CL which is shown by Figure 5.15b as the movement from point 1 to 2 and 3 to 4. It seems that at the early stage of pinning, the CL may even reverse its direction of motion and become an advancing CL under some conditions. Besides simulation, the same phenomenon also can be clearly identified in some experimental results (see Figure 5.16a). From the analytical solution from equation 5.10, the breathing motion could be from an extra contact angle decrease due to a larger contrast of bare and SWNT-covered surface. But we need more details and evidence to further verify this conclusion. The specific discussion will be in the next section.

Another important observation is that contact lines on striped surfaces generally do not advance by slippage [40,124,125] but rather by a zipper-type propagation of a kink defect. We have observed this type of movement in almost all sorts of suspensions from the real coffee to SWNT colloids, which could be another argument for the traditional "stick-slip" mode and will be carefully analyzed in next section.

## 5.2 Observation of new phenomena in CL dynamics

### 5.2.1 "Breathing motion" of the contact line

In the previous section, we have discussed the formation of SWNT stripe pattern and thin film under the two-plate setup. The dynamical pinning of the CL has been discussed in the SWNT/SDS system instead of "stick-slip" model under our two-pate setup and ambient conditions. Both simulation and experimental results show a subtle breathing motion nearly at the CL pinning moment (see Figure 5.16). The contact angle dynamics provide a reasonable explanation as well as the trend of simulation results with increasing SWNT concentrations. However, the specific experimental certification is crucial here because the type of breathing motion does not appear all the time as a regular phenomenon.

In order to obtain more substantial experimental evidence, we on one hand improve the two-plate setup by using the hydrophobic cover glass (HMDS-covered surface, see Figure 5.17a and Section 3.3 for details). It has two advantages for recording the dynamical pinning. First it doubles the effective length of capillary bridge $d$ with the same spacer distance according to the geometry (see Figure 5.13) and calculation (equation 5.10) which clearly shows that if the value of $d$ increases and the CL velocity remains, the threshold for the $\Delta\theta$ will decrease. In this situation, the CL not only gets pinned more easily but also has more extra contact angle change for a more evident breathing motion. In addition, the hydrophobic surface also effectively suppresses the pinning of CL on the cover slide due to the nearly 90° receding contact angle so that the coupling motions of the contact lines on the upper and lower surfaces can be ruled out. On the other hand, it is also possible that the breathing motion is too quick to be captured by the camera in use. We replace it with a new GoPro camera having 120 fps instead of the 30 fps old one. We thus have more details on the very pinning moment.

The black curve in Figure 5.17b shows the ordinary CL movement with hydrophilic cover slide, SWNT $1.2 \times 10^{-4}$ wt % and SDS 0.1 wt % exactly as presented in the previous section. Now using the same suspension, we repeat the experiment under the new setup. In Figure 5.17b, despite of a slightly slower velocity of the CL, the breathing motion at the pinning moment (the red curve) becomes more evident under the new setup and there are also much more data points within the same time interval recorded by the new camera.

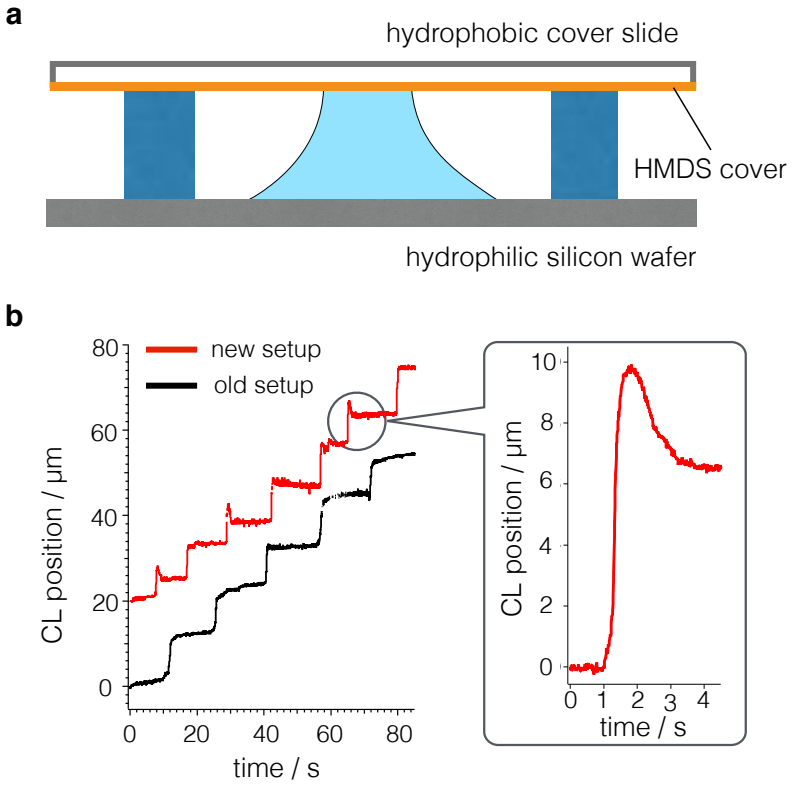


Figure 5.17: (a) Schematic of the new two-plate setup with hydrophobic glass cover slide and hydrophilic silicon substrate. (b) CL dynamics from the video sequence analysis (left) with $d = 550\ \mu m$, [SWNT]=$1.2 \times 10^{-4}$ wt % and [SDS]=0.1 wt %. The black line is from the previous setup and the red one is recorded from the setup described in (a) as well as the new camera. One typical breathing motion on the right side is zoomed in from the red curve.

By analyzing the video sequence (120 fps), we show a typical dynamical motion of CL in one depinning and pinning process (Figure 5.18). The CL (marked by red dashes) jumps about 10 µm to a new position at 2 s, then starts to retreat and finally gets pinned again on 6.5 µm position at 4 s.

The schematic illustration in Figure 5.18b shows geometrical changes of

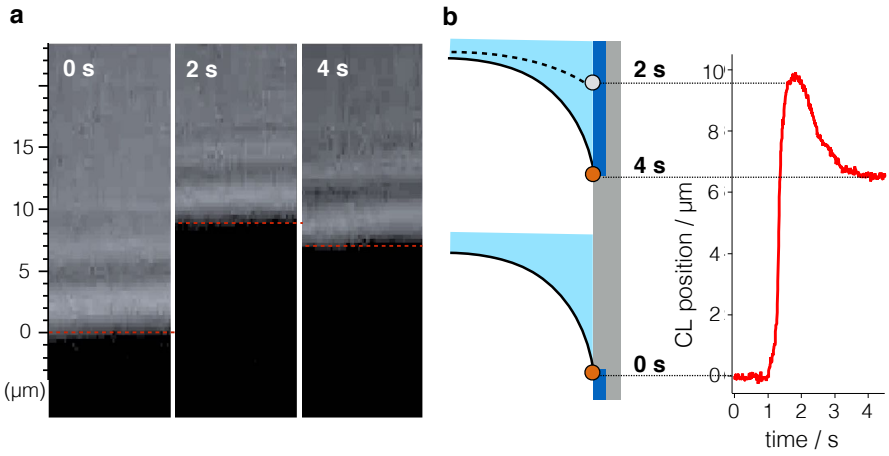


Figure 5.18: Video analysis of one dynamical pinning and depinning process. (a) Image sequence of the movement of CL. (b) CL geometry and movement during one pinning process schematic illustration (left) and the analysis of video sequence (right).

meniscus during the process. As we have already discussed in the previous section, the SWNT/SDS-covered surface regions have a higher interfacial tension, which gives rise to a smaller contact angle. When depinning starts at about 1 s, the CL touches bare silicon surface, therefore a sudden and isochoric increase of the contact angle $\Delta\theta$ makes the CL jump to 10 µm. This jump distance can be directly related to around 2° $\Delta\theta$ for the two-plate geometry by the equation 5.5.

After the CL jumps to the new position, it will get pinned immediately because the capillary flow induced by the evaporation keeps bringing SWNTs from the center to the edge. The deposition of SWNTs can again lead to a decrease of contact angle, which might then result in the retreating of the CL. But at meantime, evaporation keeps pulling the CL toward the advancing direction so that there is a dynamical interplay between decreasing contact angle and evaporation. That means, only when the $\Delta\theta$ is fast enough to offset the rate of solvent evaporation, the CL can be pinned or even retreat toward the reversed direction.

Here the expression of the critical rate $\mathrm{d}\theta/\mathrm{d}t$ can be slightly modified from equation 5.10 with the new effective $d$:

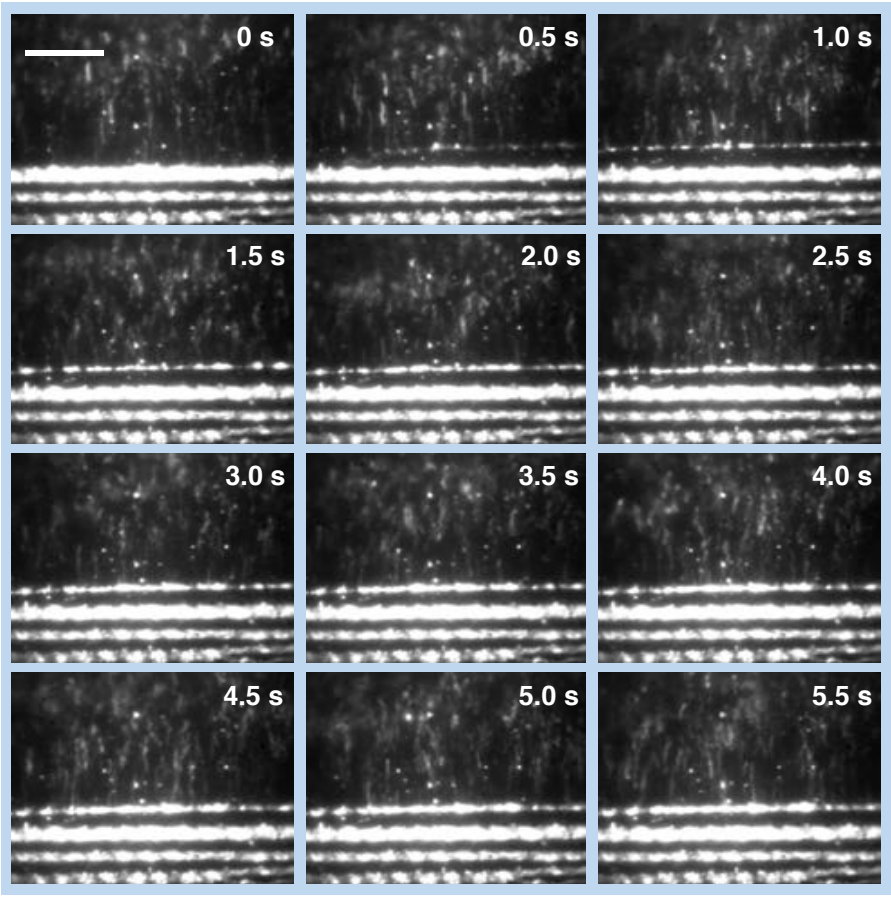


Figure 5.19: Photoluminescence (PL) image sequence of the formation of a new stripe. The scale bar here is 20 µm.

$$\frac{\mathrm{d}\theta}{\mathrm{d}t} \leq \frac{57.3^\circ}{g(\theta)} \cdot \frac{V_{av}}{2d} \tag{5.21}$$

If we bring in $d = 550$ µm and $V_{av} = 0.8$ µm/s, the threshold of $\mathrm{d}\theta/\,\mathrm{d}t$ will be around -0.12°/s. Obviously, now there becomes more extra contact angle change with the similar interfacial tension contrast so that the reverse CL can be observed more easily.

To further verify this phenomenon, we repeat the experiment under a photoluminescence (PL) microscope which can help to clearly identify the movement of SWNT particles and the growth of a single stripe. The sample is excited by 568 nm irradiation from a supercontinuum light source and PL images of the formation of stripe pattern are recorded for emission from the first subband exciton by an InGaAs camera at about 998 nm.

As shown by Figure 5.19, a series of PL images with 0.5 s intervals provide details for the movement of SWNTs near the CL (the bright dots) and the deposition process (the bright stripes). A new stripe appears at 0.5 s and its formation spreads from the right side to the left like a zipper. Then its width gradually increases because more SWNTs reach the CL. In Figure 5.20, a typical region for the stripe formation is zoomed in for a rough estimation of the CL position. The red strait lines which approximately indicate the

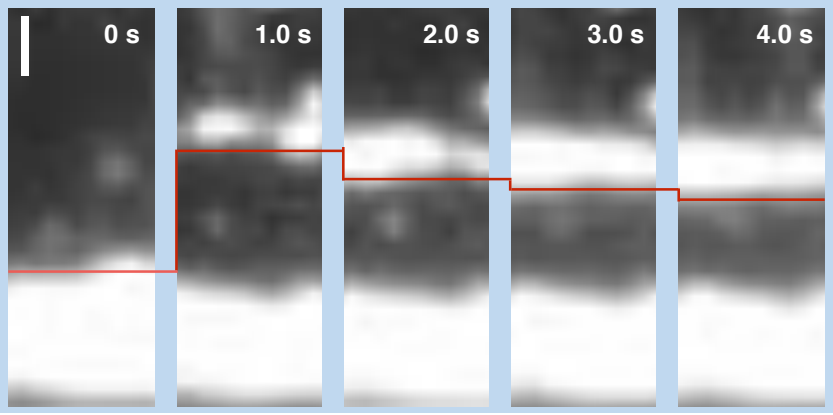


Figure 5.20: PL image sequence of the formation of a new stripe zoomed in from Figure 5.19. Red lines are used to approximately mark the front of the forming stripe. The scale bar here is 2 µm.

CL position by the PL signal of SWNTs aggregation are gradually moving reversely after the jump at 1 s.

In order to fully analyze the PL images, we apply a line profile analysis by extracting the pixel values along the cross sections of the images as shown in Figure 5.21a. Along the red strait line on a PL image, the relative intensities of each pixel are plotted against the relatively stripe position and the Gaussian function is then used to simply fit all of the peaks from the stripe pattern. A constant baseline is determined and fixed based on the region without deposition on the left side of the image. Around 20 pixels width along the

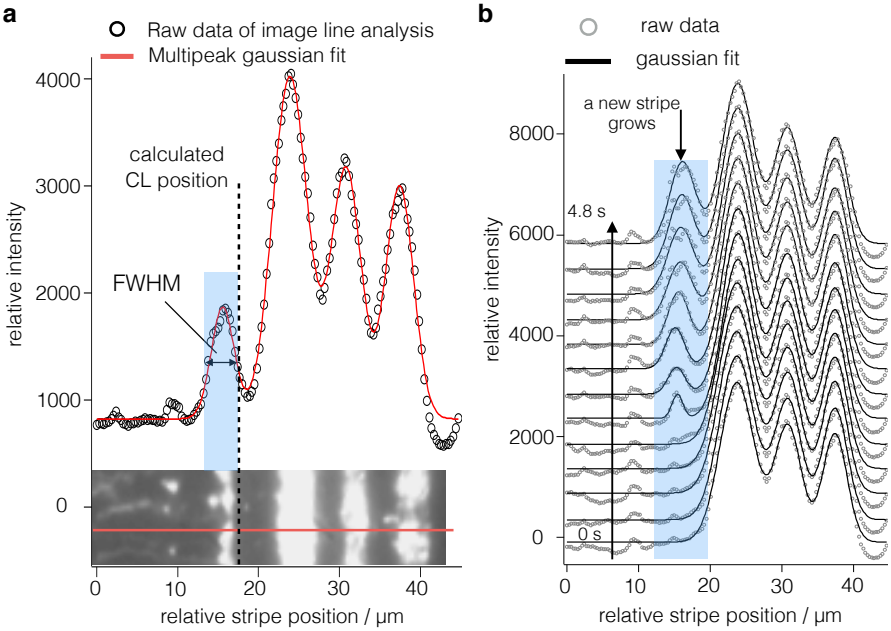


Figure 5.21: Image line analysis for the PL video sequence. (a) An example for the analysis of one PL image. All the pixel intensities along the red strait line on a PL image (at the bottom) are plotted against their relative positions on the substrate. FWHMs of the peaks of the new formed stripe are recorded to calculated the relative CL position when the stripe becomes broaden. (b) Waterfall plot of raw data and Gaussian fit curves during the growth of a stripe (in the blue area) from 0 s to 4.8 s.

stripes are chosen for the analysis of each image and the twenty curves then are averaged before the fitting. As for tracing the CL position, FWHM of the peak is used to determine the front edge of the stripe as a constant fraction. We consider this edge of the growing stripe here as the CL position. In Figure 5.21b, by combining the line analysis of several subsequent images, a waterfall plot shows the growth of a stripe within 5 s. As we discussed above, the right side of the peak should be the front line of deposition. When the intensity increases due to more SWNTs aggregation, we use the FWHM from Gaussian fitting as the constant fraction to mark the estimated CL position for each peak. The region that shows one newly growing stripe is zoomed in Figure 5.22a. Only the fitting curves are shown here. The red solid circles are the points on the curves at which the FWHM is found.

With the red solid circles as the indicator for the CL position, the reverse motion is so obvious that the CL firstly pins at about 6 µm on 2 s after a new jump and subsequently retreats beyond 8 µm on 4.8 s. This result is almost identical with the previous observation under the optic microscope.

Likewise, we collect all the calculated data points and draw the similar CL dynamics with three typical PL images in Figure 5.22b which shows that the typical CL dynamics with breathing motions on each pinning moment repeat exactly under the PL observations.

Furthermore, on the basis of the mechanism and simulation, the SWNT concentrations are supposed to affect the breathing motion by altering the interfacial energy contrast between the bare and deposited surface. The experimental results with increasing SWNT concentrations but fixed SDS content (0.1 wt %) in Figure 5.23a prove this point. In comparison with the simulation, the CL dynamics with relatively high SWNT concentrations show the enhanced breathing motions.

The last but not the least, the average velocity of the CL could also influence its dynamics according to equation 5.21. Therefore we measure the CL movement with two different average velocities whereas the other conditions remain. A relatively low concentration of SWNT ($0.5 \times 10^{-4}$ wt %) is used here to prevent the breathing motion at normal evaporation rate (CL velocity around 0.8 µm.) as shown by the blue curve in Figure 5.24. Then the same experiment is repeated under different ambient conditions (15 ℃ and 51 % humidity) which can effectively slow down the evaporation by the low temperature and high humidity. The decrease of the evaporation rate will directly give rise to a slower of average CL velocity $V_{av}$ (see the red curve in Figure 5.24) and simultaneously decrease the threshold for the rate of contact angle change (see equation 5.21). It eventually causes the possibility for the

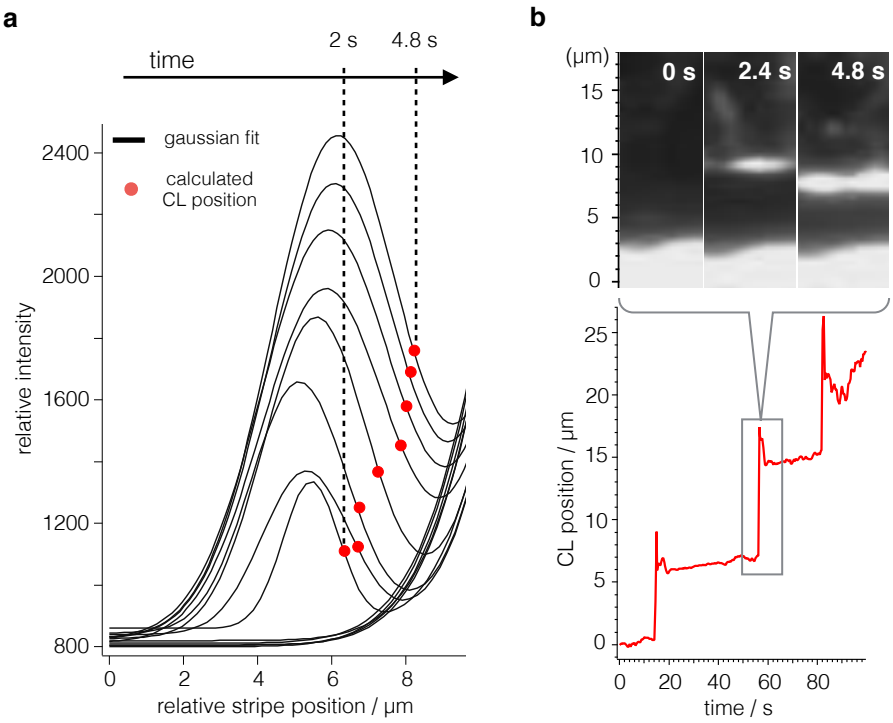


Figure 5.22: The breathing motion on the basis of the PL observation. (a) Waterfall plot traces the growth of the new stripe zoomed in from the Gaussian fitting curves in Figure 5.21a. The red solid circles indicate the calculated CL position from 2 s to 4.8 s. (b) All of the calculated points from the PL images for the CL position are collected for plotting the CL dynamics against the time. The result here is identical with the observations under the optic microscope.

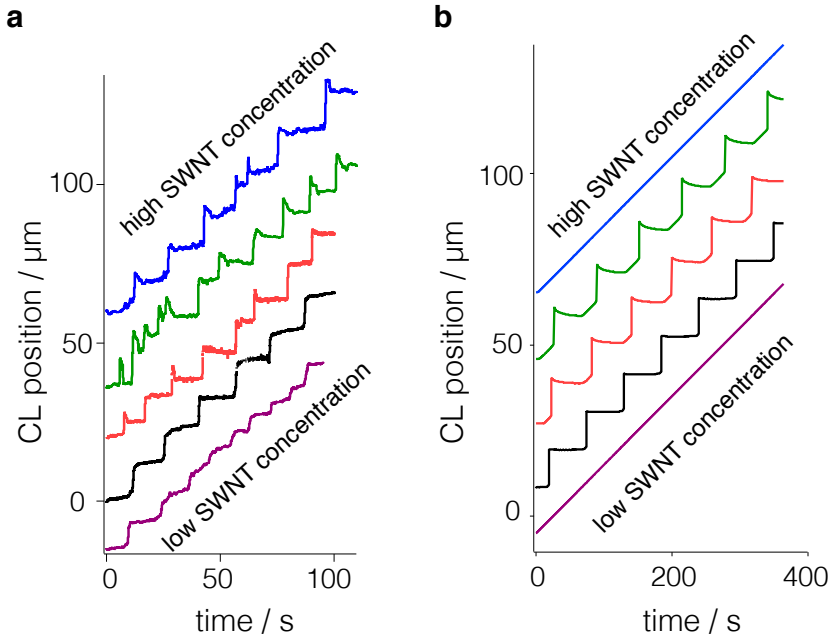


Figure 5.23: Observation of CL breathing motion on the dependence of SWNT concentration for a fixed [SDS]=0.1 wt %). (a) Experiment, concentration from top to bottom: $4.8 \times 10^{-4}$ wt %, $2.4 \times 10^{-4}$ wt %, $1.2 \times 10^{-4}$ wt %, $0.6 \times 10^{-4}$ wt %, $0.3 \times 10^{-4}$ wt %. (b) Simulation results of CL dynamics at low, intermediate and high SWNT concentrations show the similar enhancement trend of breathing motion.

breathing motion on the maintained interfacial energy contrast. Comparing the results from the high and low velocities respectively, we can easily find that breathing motion becomes evident when it comes to small CL velocity (see Figure 5.24), which is consistent with the prediction from the mechanism.

So far, clear evidence of the breathing motion has been seen in both optic and PL observations, which further certificate the mechanism of dynamical pinning. In contrast with the traditional "stick-slip" model, the contact line is not really "stick" at the edge of the meniscus. Its position however depends on the interplay between the interfacial tension contrast and the evaporation rate. This competition induces the dynamical process.

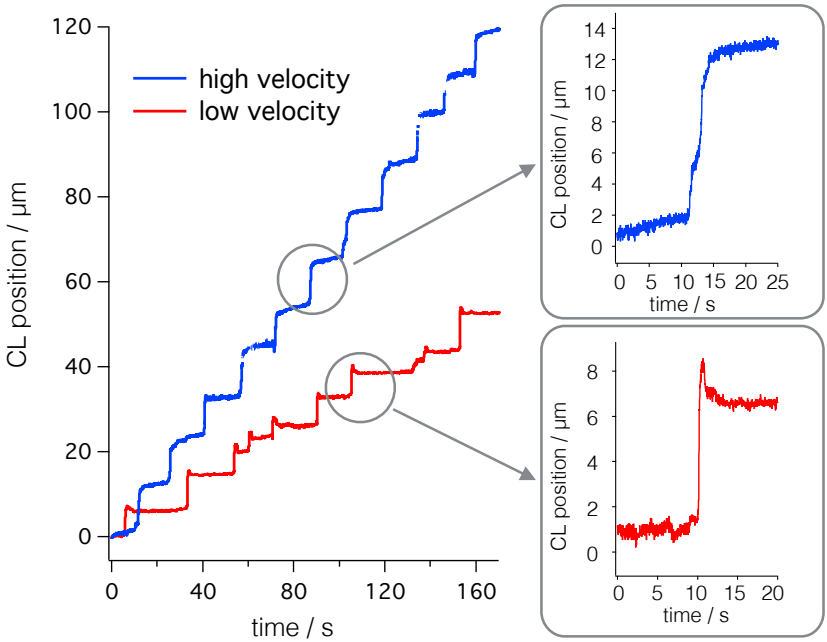


Figure 5.24: Optic microscopic observation of CL breathing motions depending on average CL velocity. The CL dynamics are from the same sample ([SWNT]= $0.5 \times 10^{-4}$ wt % and [SDS]=0.1 wt %) but different ambient conditions. High velocity (blue), 0.71 µm/s is recored under the normal 21 ℃ and 34 % humidity. Low velocity (red), 0.32 µm/s is recorded under 15 ℃ and 51 % humidity.

### 5.2.2 Contact line depinning by kink propagation

Besides the argument we have for the "stick" part, another interesting phenomenon that we discovered during the CL movement is the zipper-like propagation of the CL when it has the conventional "slip" move. The process has been simply mentioned and introduced above by the PL image sequence in Figure 5.19. Using the similar PL images, Figure 5.25 shows more details on the kink propagation.

It is clear that when a new stripe is forming, the whole CL is not slipping to a new position at the same time. In contrast, it starts at some point first and then propagates horizontally toward the whole line. Given that the suspension

is homogeneous and the deposition also proves to be uniform along the CL from PL observation and the eventually identical stripe width, this zipper-type propagation can be considered as the intrinsic characterization for the CL dynamics instead of the "slip" mechanism [40, 124]. In Figure 5.26, the typical kinks can be found in both real coffee and SWNTs depinning process under the same two-plate setup and ambient conditions.

The previous research on the kink of contact lines was primarily concerning droplets on superhydrophobic or texture surfaces [41, 137–139]. However, in the experiments here on the hydrophilic surface with a partial wetting contact angle less than 20°, we find that the kinks still account for the CL movement with the coffee stain effect.

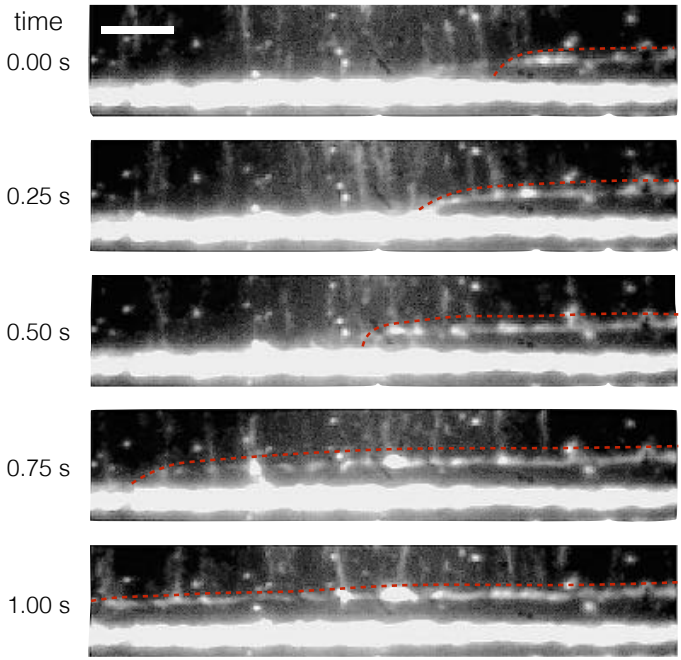


Figure 5.25: PL image sequence for kink propagation. The bright pixels indicate the SWNTs from the PL signal. A new stripe is clear forming and spreading from the right side to the left. The red dashed lines mark approximately the edge of the new stripe and its propagation distance. The scale bar here is 10 µm.

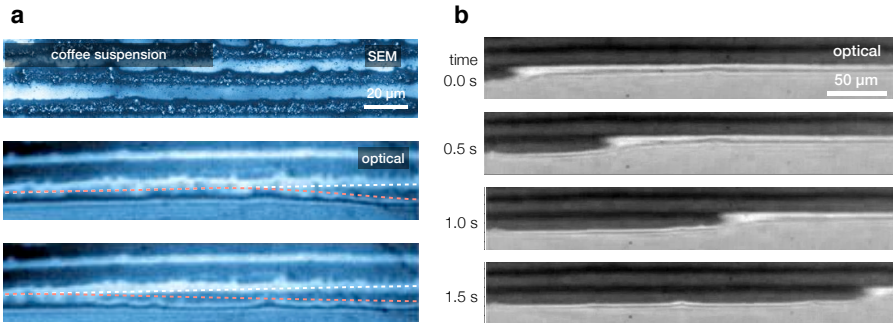


Figure 5.26: Kink propagation from coffee and SWNT suspensions under optic microscope and SEM observation. (a) Stripe formation from coffee suspensions. The SEM image shows the scale of the stripes as well as the unevenness on and between the stripes. A kink starts from the right to the left on the optical images. (b) Video sequence shows the zipper-like movement of a kink from left to right in a very short time range. Adapted from publication ref. [129] by Li *et al.*

The zipper-like kink process can be directly associated with the relief of capillary strains on other sections of the CL, which is similar to the Peierls-Nabarro mechanism for dislocations in discrete lattices [140–142]. We can however simply explain it in terms of kinematics concerning on the contact angle and work of adhesion. This discussion is an analogy from the experimental and simulation results on the hydrophobic surface with anisotropic periodic textures [41] and closely linked with our dynamical pinning mechanism above.

As shown in Figure 5.27, when the kinematics is kink-determined, the receding contact line can propagate in both x and y directions where x is along the CL and y is the reverse propagating direction. According to the discussion of pinning mechanism in the last section and the related theoretical research [143,144], the work of adhesion can be expressed as: $\Gamma = (1+\cos\theta)\gamma_{\mathrm{LG}}$ where the $\theta$ is the contact angle and $\gamma_{\mathrm{LG}}$ is the surface tension of the liquid. In the direct jumping model (Figure 5.27a), the CL only has the motion in y direction and the contact angle from bare silicon to SWNT-covered surface will decrease at the same time. However, when the kink is introduced in the line (Figure 5.27b), the CL have more time stay on the low energy surface (the bare silicon wafer here) and the effective receding contact angle actually increases, which gives rise to decrease of the adhesion work $\Gamma$. According

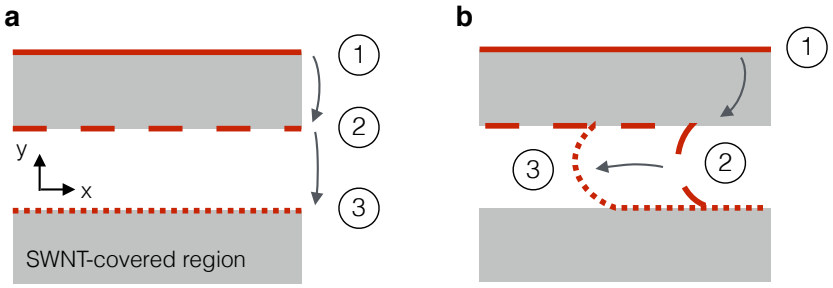


Figure 5.27: Schematics of two types of contact line receding. (a) Direct jumping as a straight segment. (b) As a kink. The gray regions indicate the SWNT-covered surface. The sequence of lines 1, 2 and 3 suggests the kinematics of the CL depinning for each configuration.

to the simulation results on the surface textured with stripes from Gauthier *et al.* [41], the threshold of depinning with a kink is about 2/3 lower than that for a straight line. In addition, it is also evidenced experimentally and numerically that the receding contact angle can maintain isotropic even on strongly anisotropic surfaces [41,138]. That means when a kink happens, contact angles from x and y directions are nearly identical despite that they are on different surfaces.

For this isotropic contact angle, our experiments also show the related evidence. On the basis of our discussion about the dynamical pinning, the unique breathing motion happens when the CL get pinned, especially at relatively high SWNT concentration.

From the observation of the kink and the subsequent breathing motion, we however notice that there is typically a time interval between the depinning and the reverse breathing motion as shown by Figure 5.28 (the image 3 and 4 particularly). The delay of the breathing motion is very short, maximum 0.4-0.5 s just like the time scale of a depinning process. During this time interval, the CL has already jumped to a new position in the region we observed (the whole CL length about 230 µm) and seems to stop there waiting for the end of the entire kink instead of a direct reverse motion. With the video sequence analysis (120 fps), a platform of the holding CL is clearly showed by Figure 5.28b between the points 3 and 4. It shows that during the propagation of the kink, the newly pinned CL does not change evidently and the breathing motion also does not start immediately, which means that the corresponding contact angle still keeps more or less the same value at least within the 0.4 s

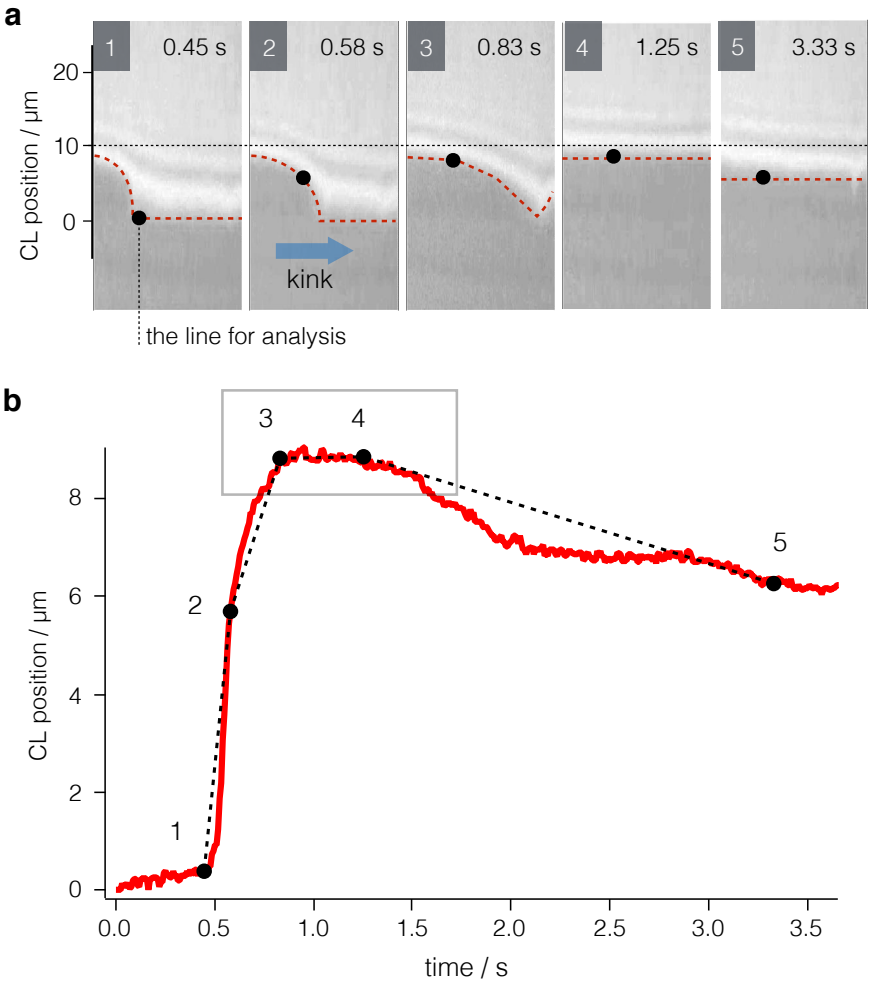


Figure 5.28: A kink before a breathing motion. (a) Five optical microscopic images show the kink and the subsequent breathing motion. The red dashed lines mark the shape of the CL during the process. The horizontal black dashed line is the 10 µm position as a reference. The vertical black dashed line and the solid black circles are the line for the image analysis and the position on the CL respectively. (b) The CL dynamics for the whole process within 4 s. The solid black circles here are the data points corresponding to the five images above. [SWNT]= $1.2 \times 10^{-4}$ wt % and [SDS]=0.1 wt %.

interval. If we measure the velocity of kink, the range is from 80 µm/s to 300 µm/s (see Figure 5.29a). Kinks with these velocities can propagate through the whole CL we observed within 1 s which is in consistence with the time intervals we measured. Now combining with the discussion on kinematics above (Figure 5.27), we can find that the contact angle of the freshly pinned CL (y direction) and that on the moving meniscus of the kink (x direction) are similar before the whole kink movement finishes along the CL. In brief, the kink-induced isotropic contact angle reduces the threshold for depinning of the CL in the dewetting process as we discussed before.

Naturally this zipper-like motion extends the time for which the CL stays on a maturing stripe and allows the stripe widths to continue to increase to the widths observed experimentally (see Figure 5.9). The capillary strain relief by kinks in the CL can thus provide a simple explanation fo the observation of broader stripe widths than predicted by simulations. As shown by Figure 5.29a, the velocity of kink propagation is found to be inversely proportional to the SWNT concentrations which can effectively change the widths of the stripes at certain SDS concentration (Figure 5.9). In this case, a slower kink at high SWNT concentration can further broaden the stripe width.

In addition, the video sequences feature several examples that show the origin of kink propagation. Within the field of view, kinks sometimes appear to originate from an impurity site as shown by Figure 5.29b-d. In the SEM images (Figure 5.29e and f), the similar phenomenon can be confirmed by the bell- or hat-shaped void on stripe and continuous film patterns. Obviously, the initial role of big impurities here is to provide local relief from capillary strains on the CL as the impurity starts to puncture the approaching liquid-gas interface.

In some cases the video sequences nevertheless show the formation of multiple kinks on the same line within the field of view. At other times the origin of kinks appears to be a seemingly featureless stripe region with the optical resolution. However, even without any visible impurities, many SEM and AFM images show that the surface of SWNT stripes is not perfectly homogeneous and uniform. Consequently any stripe must feature some degree of heterogeneity of interfacial tension. Possible origins of kink are therefore either surface region with sudden increase of capillary strains like defects or regions with higher interfacial energies which give rise to a faster local evaporation. This implies that kinks do control the formation for the stripe and are difficult to avoid.

In summary, we have investigated two special phenomena of the CL during the coffee stain effect of SWNT colloid under our two-plate setup and ambient

conditions: the kink and the breathing motion. With these two fundamental features, we actually reinterpret the conventional "stick-slip" model by treating the "stick" as the dynamical process with a reverse breathing motion

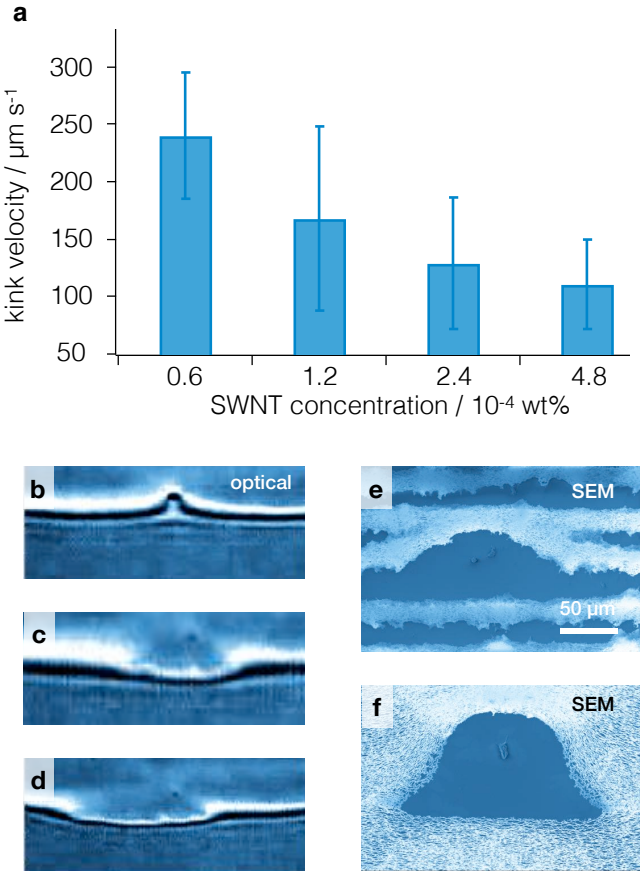


Figure 5.29: (a) Kink velocities from different SWNT concentrations with a fixed SDS concentration (0.1 wt %). The data analysis is from the same experiments of the breathing motion above. (b-d) Birth of two propagating kinks at an impurity. (e-f) SEM images of SWNT deposits near an impurity for striped and continuous film, respectively. Adapted from publication ref. [129] by Li *et al.*

and "slip" as the kink-controlled movement instead of the direct jumping. Both of these common features of CL are consistent with our interpretation of mechanism and will be important for people to further understand and control the film fabrication by EISA. In the next section, the experiment in ambient conditions will be changed into a temperature-controlled one in order to study the effect of the temperature and the possibility of higher efficiency of deposition.

## 5.3 Thermally enhanced evaporation-induced self-assembly

In the previous discussion, almost all of the experiments for deposition were accomplished in the ambient conditions (room temperature 18-22 ℃ and humidity 30-40 % ). By changing the capillary length of the meniscus between the two plates, the velocity of contact line can increase up to nearly 2 µm/s due to the inhomogeneity of evaporation along the meniscus (see Figure 5.2). As for a regular stripe pattern by coffee stain effect, the efficiency of fabrication here is much higher than the traditionally stationary and vertical evaporation. However, it is still unclear that how high the velocity can be for the stripe fabrication if we accelerate the deposition rate by increasing the temperature. Besides, it is also interesting to see the change of the concentration matrix (Figure 5.4) induced by the change of temperature because the surface tension of the suspension which is the key factor during the pinning and depinning process can be altered by the temperature.

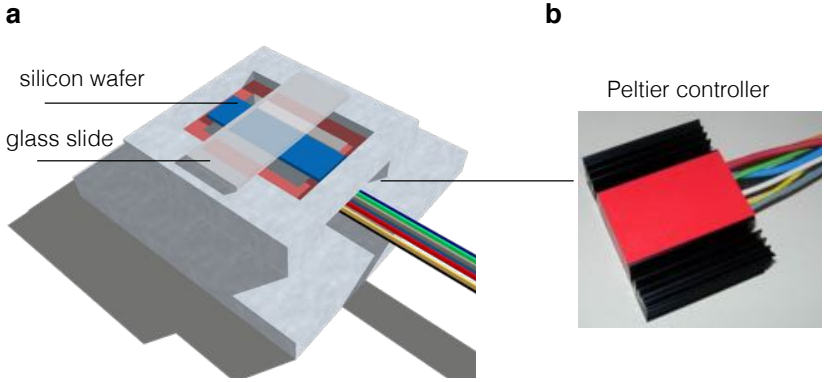


Figure 5.30: (a) Schematic of the setup with heating platform. (b) The Peltier controller on the bottom for increasing and maintaining the temperature.

In this section, we investigate the same SDS-dispersed SWNT colloids which evaporate on a heating substrate. The temperature range is from the ambient to 60 ℃which can be quickly reached and maintained by a new home-built setup (Figure 5.30). The hydrophilic silicon wafer and glass slide are located in parallel on a platform with a rectangular concave area which gives rise to an accurate 500 µm gap of the capillary length. The platform is connected

to a Peltier controller, a thermoelectric device that can precisely increase and maintain the temperature within 100 ℃ in a few seconds. The details of principle and performance about the heating device can be found in Section 3.4.

In order to estimate the influence of the temperature, a known concentration couple of SWNT and SDS which can surely produce stripes are used in the first place. As shown by the SEM images in Figure 5.31, the stripe pattern can be reproduced at room temperature (RT, 23 ℃ ) but quickly transformed into the holey structure when the it comes to 30 ℃ . Then further increasing of the temperature makes the holes filled by more SWNTs but the film becomes more inhomogeneous at 50 ℃ . The variation of these structures clearly suggests that there are too many SWNTs to make regular stripes when it comes to higher temperature.

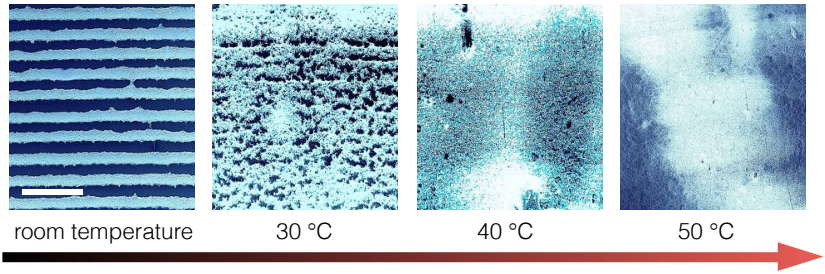


Figure 5.31: The SEM images for the deposition with increasing temperatures. The room temperature (RT) here is 23 ℃ and the concentrations [SWNT]= $2.0 \times 10^{-4}$ wt % and [SDS]=0.1 wt %. The scale bar here is 40 µm.

On the other hand, the increasing temperature can also decrease the surface tension of the solution, especially when the SDS concentration is low [145]. According to Figure 5.3, when the SDS concentration is lower than 1 mM ($\approx$ 0.02 wt%), the surface tension of the solution at RT becomes close to that of pure water (72 mN/m). However, if we increase the temperature from RT to 60 ℃ the surface tension will drop to 65 mN/m [145] which is close to the range of concentration for the fabrication of stripe pattern (0.05-0.1 wt %, see Figure 5.4).

Depending on the consideration and estimation above, we use a fixed SDS concentration (0.02 wt%) but gradually increase the SWNT concentration in order to study the its correlation with temperature. As shown by the

SEM images in Figure 5.32, a new matrix with SWNT concentrations and temperatures has been established similar to Figure 5.4 except that we focus on much lower SWNT concentration here.

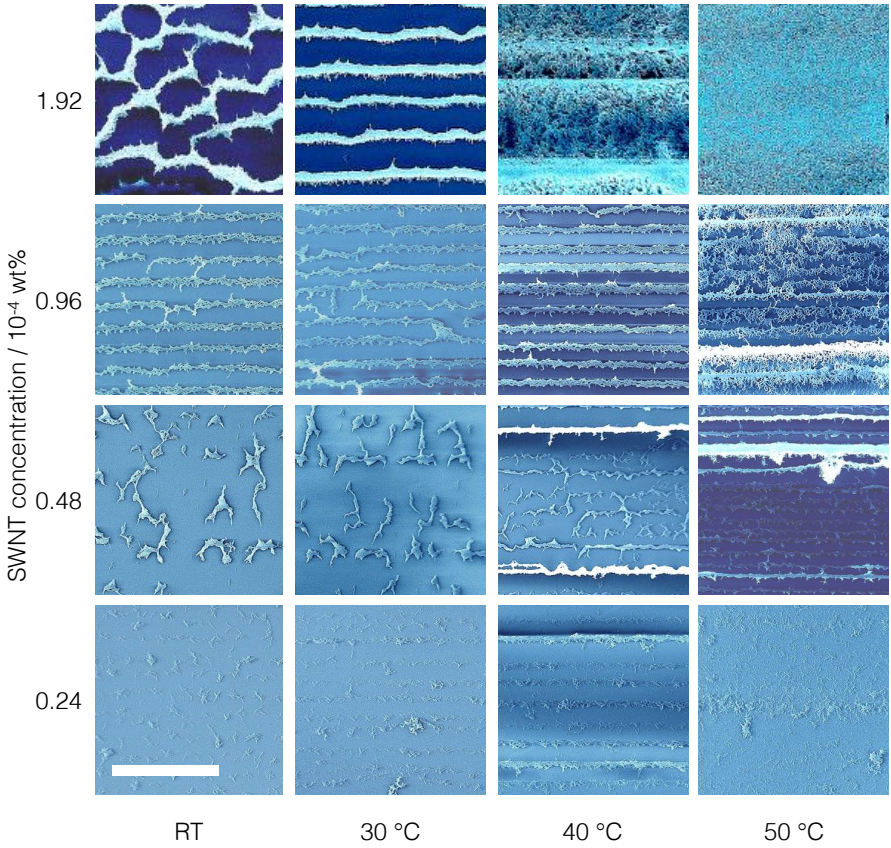


Figure 5.32: SEM images for different SWNT concentrations and temperatures of the substrate. The SDS concentration is fixed as 0.02 wt%. RT here is 24.2 ℃ and the scale bar is 40 µm.

The previous discussion in Section 5.1 with experiments under ambient conditions has already predicted the patterns at RT in Figure 5.32 (the leftmost column). With this range of low SWNT and SDS concentration, the pattern will be "islands" made of SWNT aggregates at first ($0.24 - 0.48 \times 10^{-4}$ wt

%), then irregular stripes or holey films with higher SWNT concentration ($0.96 - 1.92 \times 10^{-4}$ wt %) and finally a homogeneous film ($> 2 \times 10^{-4}$ wt %). Then if we increase the temperature to 30 ℃ interestingly the randomly scattered or connected aggregates start to form the regular stripe pattern, most obviously on the higher SWNT concentration.

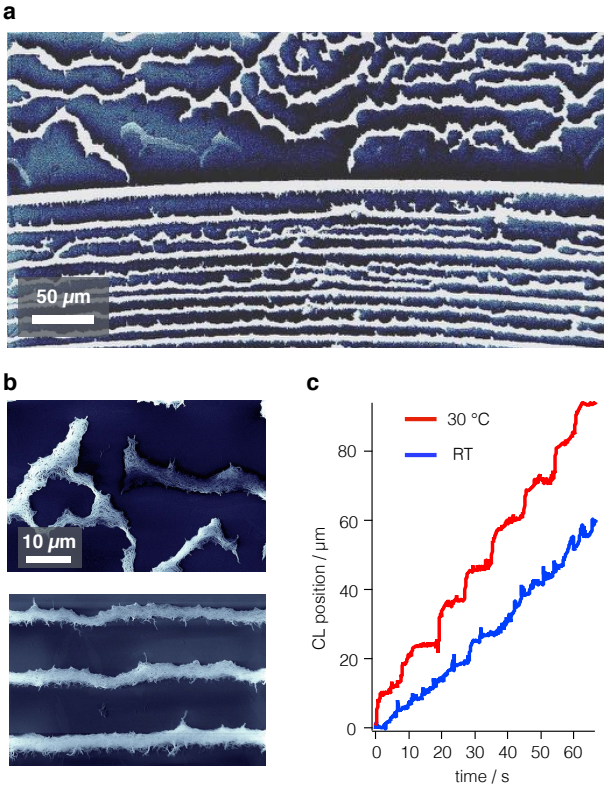


Figure 5.33: (a) SEM image for the transition from RT to 30 ℃ . [SWNT]=$1.92 \times 10^{-4}$ wt %. (b) Partly enlarged SEM images for the details about different morphologies. (c) CL dynamics under two temperatures. The average velocities are 0.9 μm/s for RT and 1.4 μm/s for 30 ℃.

In Figure 5.33a, a SEM image (1000× magnification) shows a clear transition line between RT and 30 ℃ for the SWNT concentration $1.92 \times 10^{-4}$ wt% in Figure 5.32. The randomly arranged and discrete aggregates suddenly turn

into a regularly stripe pattern after a little wider first line where the CL holds for a longer time before the depinning happens. The CL dynamics also shows the same results (see Figure 5.33c). The rate for fabricating stripes can be increased to 1.4 µm/s under 30 ℃.

Likewise the prediction, fabrication of stripe pattern for lower SWNT concentration, for example for [SWNT]=$0.48 \times 10^{-4}$ wt% in Figure 5.32, needs even higher temperature because the pinning can only happen when there is enough contrast of interfacial energy between bare and SWNT-covered surface, which means that the enhanced evaporation at the CL should be able to bring sufficient SWNT particles to the deposition region. So it can be found in Figure 5.32 that the stripes start to appear at 40 ℃ or 50 ℃ when it comes to even lower SWNT concentration. However, compared with RT or 30 ℃ , the alignment of SWNT generally becomes worse at high temperatures, which is also reasonable because the rodlike particles need enough time to rotate for the self-organization as we discussed in Section 5.1. Therefore the temperature higher than 40 ℃ might not be favorable for the local orientation of the stripes. The pinning and depinning movement also disappear when the temperature is higher than 50 ℃ or the SWNT concentration is lower than $0.24 \times 10^{-4}$ wt%.

Another import factor here is the SDS concentration. In order to obtain the specific effects of SDS in the system, we keep the SWNT as $0.96 \times 10^{-4}$ wt% and repeat the similar controlled temperature experiments. The results by SEM images are shown in Figure 5.34. The trend in general is clear that when the temperature is higher than RT, the SDS concentration has to maintain as low as 0.05 wt% to form a regular striped pattern. Furthermore, the higher the temperature is, the lower the SDS concentration must be. Still the regularly repeated structure can hardly be identified at more than 50 ℃ or 0.2 wt% SDS. It can be explained firstly by the temperature effects on the nanostructure of SDS micelles in water. The micelle ellipsoid volume of SDS is found to decrease with increasing temperature or decreasing SDS concentration [146]. For example, there are about 60 SDS molecules in one micelle at RT for a 0.5 wt% concentration. This number falls to around 30, only half of that at RT, when the temperature is 60 ℃ [146]. Despite that the CMC of SDS in this temperature range is almost unchanged [147], the SDS molecules are actually much easier to form the micelles especially in the area with stable high temperature close to the substrate. The contrast of interfacial energy between bare and SWNT-covered region thus can be effectively decreased by this micelles so that it is impossible to see the coffee stain effect in this condition.

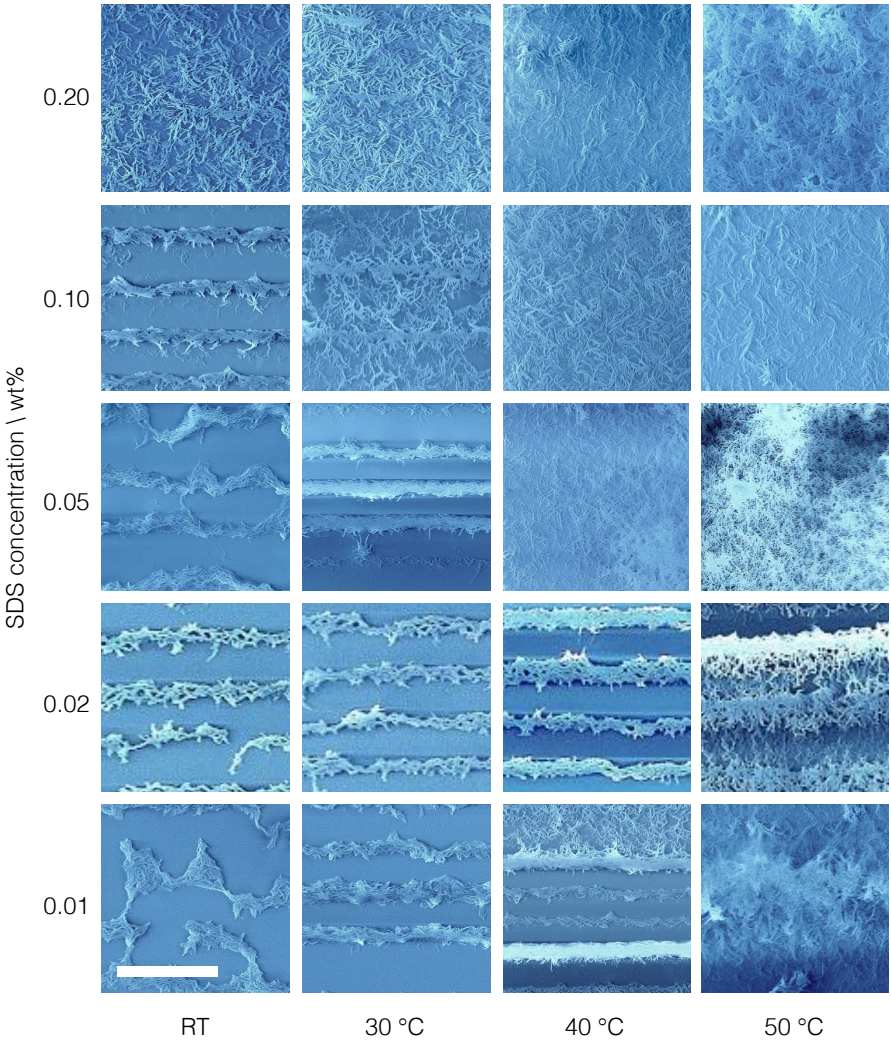


Figure 5.34: SEM images for different SDS concentrations and temperatures of the substrate. The SWNT concentration is fixed as $0.96 \times 10^{-4}$ wt%. RT here is 25.1 ℃ and the scale bar is 20 µm.

Moreover, the desorption rate of SDS on the SWNT surface can be enhanced by the increasing temperature [148, 149]. If so, the interfacial tensions on bare and SWNT-covered surface will become more close and consequently the contact angles will be similar to avoid the depinning.

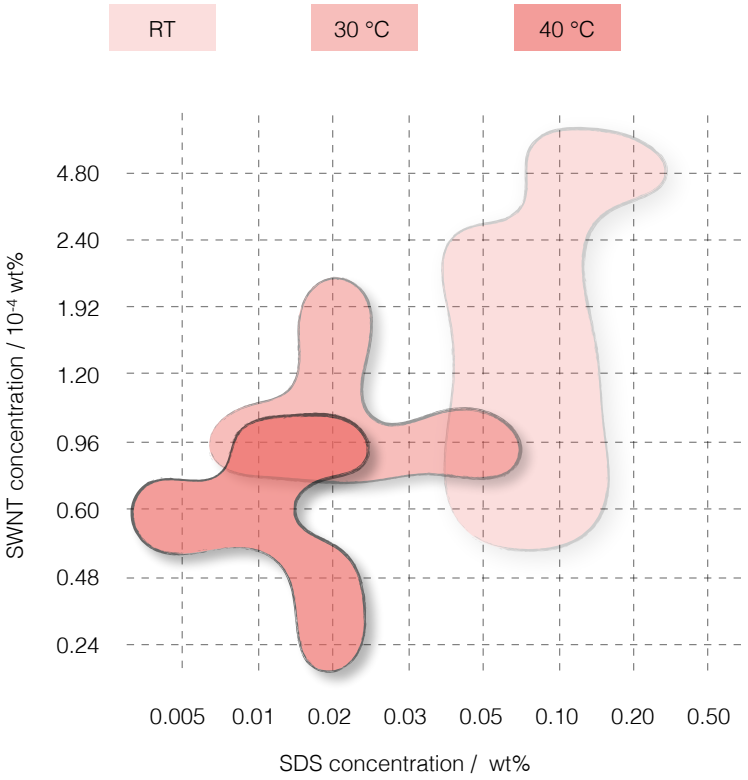


Figure 5.35: Schematic matrix for the SWNT and SDS concentrations that can produce stripe pattern at different temperatures.

To sum up, in this section we have discussed the temperature effect on the deposition of SWNTs by the capillary bridge. As illustrated schematically by Figure 5.35, the interesting striped pattern governed by the coffee stain effect is moving towards lower SWNT and SDS concentrations when it comes to the higher evaporated temperature of the suspension. There might exist multiple reasons for this trend as we discussed above: acceleration of the SWNT de-

position, the easier formation of micelles for the SDS and also the enhanced desorption of SDS on the SWNT surface due to the increasing temperature. Although the rate of the deposition can be increased to as high as 2.5 µm/s at 40 ℃ for a regular striped pattern, the alignment of SWNT is undermined due to the too less time for SWNTs to rotate.

# 6 Self-assembled SWNT thin films with polymer conjugates in organic solvents

PFO and PFO-BPy are two polyfluorene based polymers widely used to selectively disperse the semiconductor SWNTs [20]. The suspensions of single chirality (7,5) or (6,5) SWNTs can be produced by PFO or PFO-BPy respectively as we detailedly described in Section 3.1. In this chapter, these polymer dispersed semiconductor SWNTs in organic solvents will be used for the film fabrication. The fabrication methods not only include two-plate or lens setup we have used before but also a so called dose-controlled floating evaporative self-assembly (DFES) method to try the EISA on the liquid-air interface [43].

In the first section, we will discuss the similar important factors under the same capillary-bridge geometry for deposition with SWNT/polymer organic solutions, for example concentration, contact line velocity and contact angle. The mechanism of dynamical pinning and kink propagation are used to elucidate the process and some phenomenon we observed in the new system.

The second section will focus on the DFES method which allows the SWNT self-assemble on the air/water interface. This special evaporation-induced self-assembly has the advantage to control where the stripes are deposited and the quantity of SWNTs by applying the exact doses and coordinating with the moving speed of substrate. Because some new parameters are also introduced into the system, the variation of the fabrication becomes more complicated and the conditions for the striped pattern turn out to be more stringent.

Finally, we also investigate the optical properties of self-assembled stripe structures by fluorescence microscopy and fluorescence excitation spectroscopy. The results are presented in the last section in this chapter.

## 6.1 Thin film formation under two-plate and lens setup

The PFO or PFO-BPy wrapped SWNTs are dispersed in toluene after the sonication and centrifugation (see Section 3.1.2 for the detail). Then the solution can be filtrated to get rid of the excess polymer and redispersed in other common organic solvents such as toluene, tetrahydrofuran (THF) and chloroform [150]. Due to this preparation process, only the concentration of SWNT is adjustable. According to the direct experience from the experiments with aqueous solutions, at first we tried PFO dispersed (7,5) SWNTs with the concentration within the same range we found by the aqueous solution and repeat the EISA process with all of the three different solvents in ambient conditions and the normal two-plate setup.

In Figure 6.1, the typical SEM images however show that the expected regular pattern is absent not only in each solvent but also in all SWNT concentrations that we choose for the fabrication. These negative results still provide us lots of useful information. As for the toluene solvent, the SWNTs are wrapped tightly and aggregately by the PFO (see Figure 6.1) despite that the contact line (CL) sometimes follows the pinning and depinning process. No matter what concentration of SWNT we use, the PFO dominates the whole deposition. It suggests that toluene is not the ideal solvent for this fabrication.

PFO also can be well-dissolved in THF but the deposition results with SWNT colloids are almost irregular as shown in Figure 6.1 (medium). There seems to be a stripe-like trend on the surface but the zoomed-in image shows no local ordering of the SWNTs. The SWNTs are randomly and loosely connected with each other in this situation.

Nevertheless, the SEM images from chloroform on the bottom of Figure 6.1 show some interesting results. Although randomly arranged tubes form a network on most of the area, some striped-like morphologies can be found with local ordering in a small range. It implies that chloroform could be a better choice than other two solvents. Furthermore, the CL dynamics and the typical morphology from these results suggest that the failure of reproducing the coffee stain effect is due to the too low surface tension of these organic solvents. If we compared them with that of water in 20 ℃ (72 mN/m), toluene is 28.4 mN/m, THF 26.40 mN/m and chloroform 27.50 mN/m. Such low values of surface tension give rise to quit small equilibrium contact angles and the receding contact angles are even hard to be measured accurately

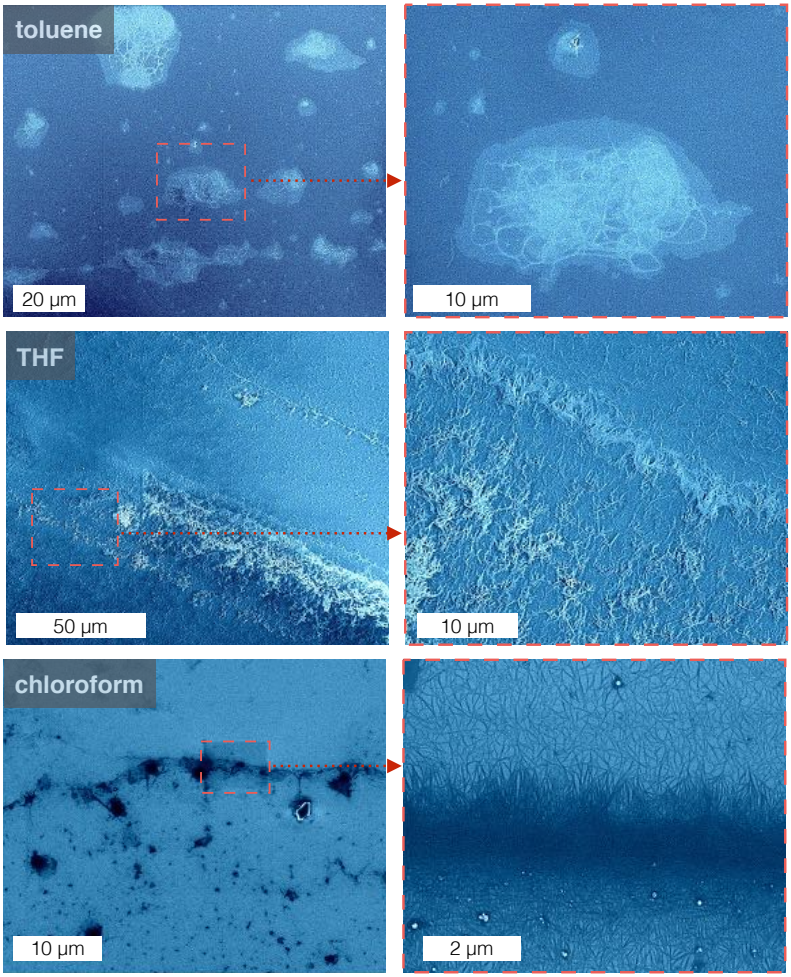


Figure 6.1: SEM images for depositions of the three different sorts of solvents. PFO-SWNT conjugates are used for deposition. The SWNT concentrations here are $0.6 \times 10^{-4}$ wt % for the toluene (top), $1.5 \times 10^{-4}$ wt % for the THF (medium) and $1.6 \times 10^{-4}$ wt % for the chloroform (bottom). Experiments are all in ambient conditions with two-plate setup (capillary length: 550 µm).

because it is typically smaller than 10° [151]. In this situation, the expected contact angle difference from the contrast of interfacial tension is supposed to be narrowed to suppress the depinning motion as we have discussed in Chapter 5.

A direct improvement is to increase the contact angle of the solution on the bare $Si/SiO_2$ surface without SWNTs. As we have described and used for the glass cover slide before, HMDS is again covered on the silicon wafer to increase the contact angle for the new experiments (see the Section 3.3 for the details of preparation). It is clear that HMDS can make the $Si/SiO_2$ surface hydrophobic with contact angle more than 90° but there is still no direct evidence from the reference to show how large the contact angle of chloroform can change on the HMDS. Therefore we need the pre-experiment to prove that the HMDS can have an effect on the contact angle and calculate it quantitatively.

It is too difficult to measure these small contact angles directly by the static sessile drop method but the equilibrium contact angle can be estimated indirectly by known geometrical shape and volume of the drop. Two droplets of SWNT colloid with a identical volume 2 µL and SWNT concentration $0.8\times10^{-4}$ wt% were placed on the normal $Si/SiO_2$ and HMDS-covered surface respectively. If the shape of the sessile drop can be treated like a spherical cap, the volume of it ($V_{\mathrm{drop}}$) will be easily expressed as:

$$V_{\mathrm{drop}} = \frac{1}{24}\pi d_{\mathrm{drop}}^3 \left(\frac{2-3\cos\theta+\cos^3\theta}{\sin^3\theta}\right) \tag{6.1}$$

where $d_{\mathrm{drop}}$ is the diameter of the drop which can be easily measured. For a constant and known volume of droplet, the relation between $d_{\mathrm{drop}}$ and equilibrium $\theta$ can be well defined. As shown by Figure 6.2a, the drop on hydrophilic bare silicon surface makes a disc of film whose diameter is around 4 mm, however the identical droplet placed on the HMDS-treated surface forms a typical "coffee ring" pattern and the diameter shrinks to 3 mm more or less. Depending on equation 6.1, the result of quantitative calculation is shown in Figure 6.2b where the curve is plotted by the correlation between the diameter and contact angle with 2 µL drop volume. The increase of the equilibrium contact angle is very evident from 20° to 40° when the drop on HMDS-covered surface but the actual receding contact angle during the evaporation is supposed to be smaller than that.

On the basis of this result, we repeated the similar EISA experiment on the two-plate setup but with HMDS-covered substrates instead. The exact solution here we used contains $0.8\times10^{-4}$ wt% SWNT and PFO conjugates, the

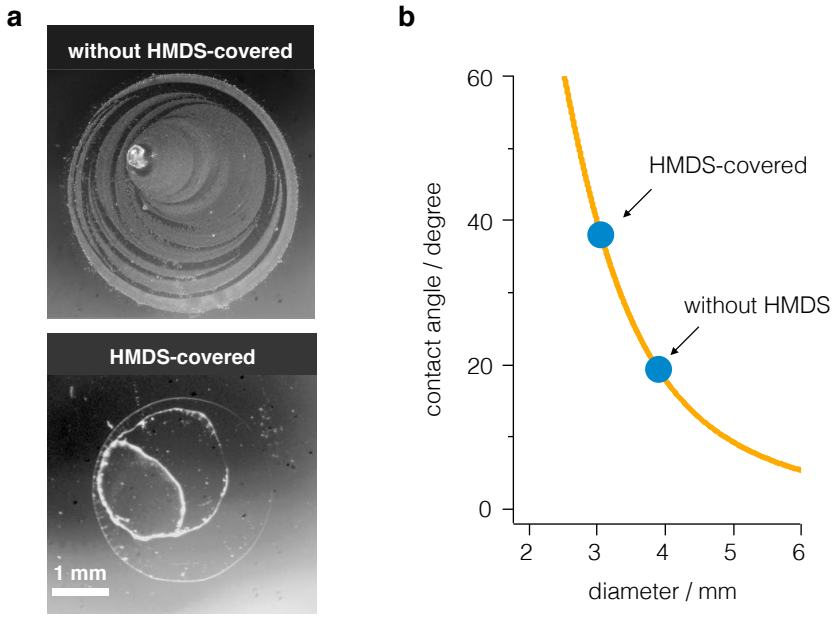


Figure 6.2: The comparison of contact angles on bare $Si/SiO_2$ and HMDS-covered surfaces. (a) The optical images of the deposition patterns from the same 2 µL sessile droplets of SWNT-PFO conjugates in chloroform but on the different surfaces with or without HMDS. (b) With the constant drop volume 2 µL, quantitative calculation based on equation 6.1 shows that the contact angle increases dramatically on HMDS-covered surface.

HPLC chloroform mixed with 1 v% (v/v%, volume percent) ethanol which plays a very important and subtle role in this system as well and will be carefully discussed later in this section.

The typical pinning and depinning process can be identified this time as shown in Figure 6.3. From the CL dynamics in Figure 6.3a, we can obtain the average velocity of CL as high as 19.9±2 µm/s which is one order of magnitude higher than CL velocities recorded previously with aqueous solution. Obviously it is because chloroform is more volatile than water (boiling point 61.15 ℃). The average time interval and jump distance are also distinct in this situation. It only needs about 3.1±0.9 s for one typical pinning and depinning process. The average jumping distance is around 58.1±14.3 µm which is much

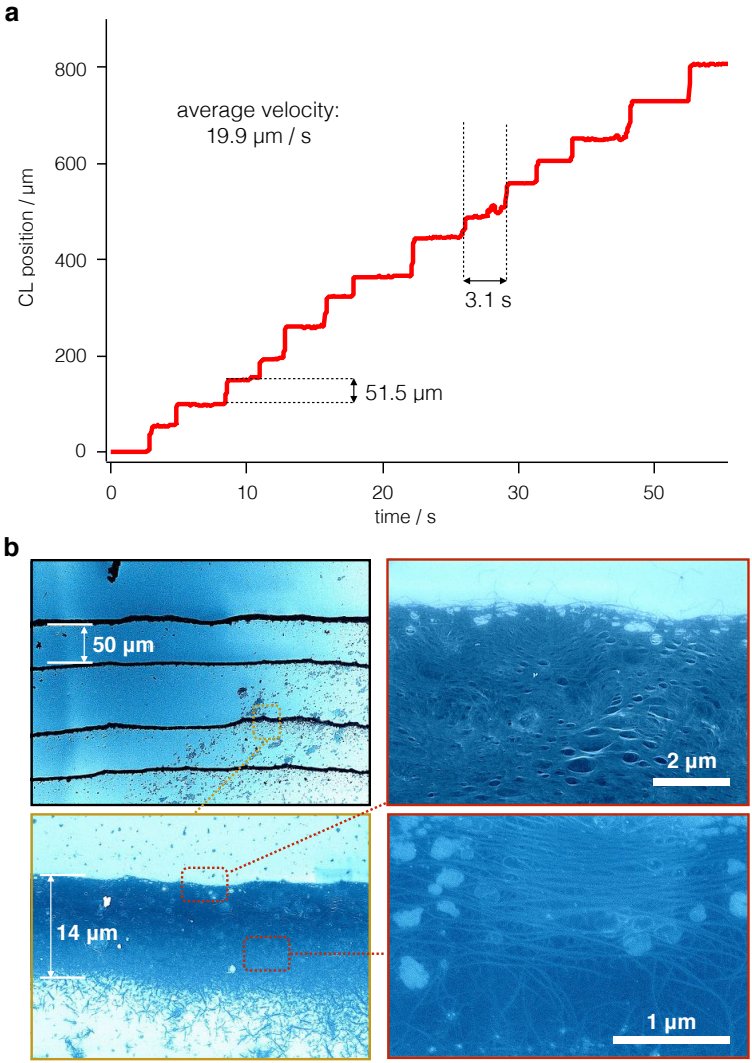


Figure 6.3: The deposition of SWNT-PFO conjugates dispersed in chloroform on HMDS-covered silicon wafer with two-plate setup. (a) CL dynamics from the observation by optic microscope. A typical time interval and a jumping distance are marked. The average velocity is calculated as 19.9 µm/s. (b) SEM images for the morphology. [SWNT]=$0.8 \times 10^{-4}$ wt%.

bigger than 8 µm from the aqueous solution with the same 550 µm of capillary bridge. The width of the stripe is not so homogeneous in this case ranging from 10 to 20 µm. The alignment of SWNT is displayed in Figure 6.3b. The too quick evaporation gives rise to inhomogeneity within one stripe. In the early stage of the deposition, the upper edge of the stripe has multi-layered SWNTs with higher dense than that on the lower part of the stripe. Furthermore, when a depinning movement starts, the arrangement of SWNTs on the bottom of the stripe become random, which is consistent with the previous mechanism of order-to-disorder transition in coffee stains [66, 152]. It states that the high-speed particles at the depinning moment are jammed into a disordered phase because they do not have the time to arrange orderly [66].

As for the quantitative calculation, we have already known from the equation 5.6 that the jumping distance $\Delta x$ can be directly associated with the change of contact angle $\Delta\theta$:

$$\Delta x = d \cdot f(\theta) \cdot \Delta\theta \tag{6.2}$$

where the function $f(\theta)$ which is also shown in Figure 5.12 only has one variable $\theta$. So if we want to obtain the value of $\Delta x$, we have to determine the receding contact angle first. Instead of the direct measurement, we take advantage of the geometrical characterization of the setup and reckon the contact angle by the measured width of the meniscus (see the dark area in Figure 6.4a). The distance from the CL to the center of the meniscus (w) can be easily measured to calculate the contact angle on the basis of the geometry illustrated schematically by Figure 6.4b. For a known length of the capillary bridge (d=550 µm), it yields:

$$\mathrm{w} = \frac{1 - \sin\theta}{\cos\theta} \cdot \frac{d}{2} \tag{6.3}$$

If we put the width before pinning ($w_1$=164.4 µm) and depinning ($w_2$=253.2 µm), the average contact angles calculated from the equation 6.3 are 32.6° ($\theta_1$) and 6.3° ($\theta_2$) respectively (see Figure 6.4c). If we compare the receding contact angle on the HMDS-covered silicon wafer ($\theta_1$=32.6°) here with the equilibrium one we estimated previously by droplet experiment (around 40°), the slightly smaller value here for the receding one is reasonable. But the contact angle before depinning ($\theta_2$=6.3°) should be treated like rough estimation (<10°) due to the inaccuracy of this method and errors in the range of small angles. As we discussed in the last chapter, the contact angle change is induced by the contrast of interfacial tension between HDMS-covered silicon surface and PFO-covered SWNT surface.

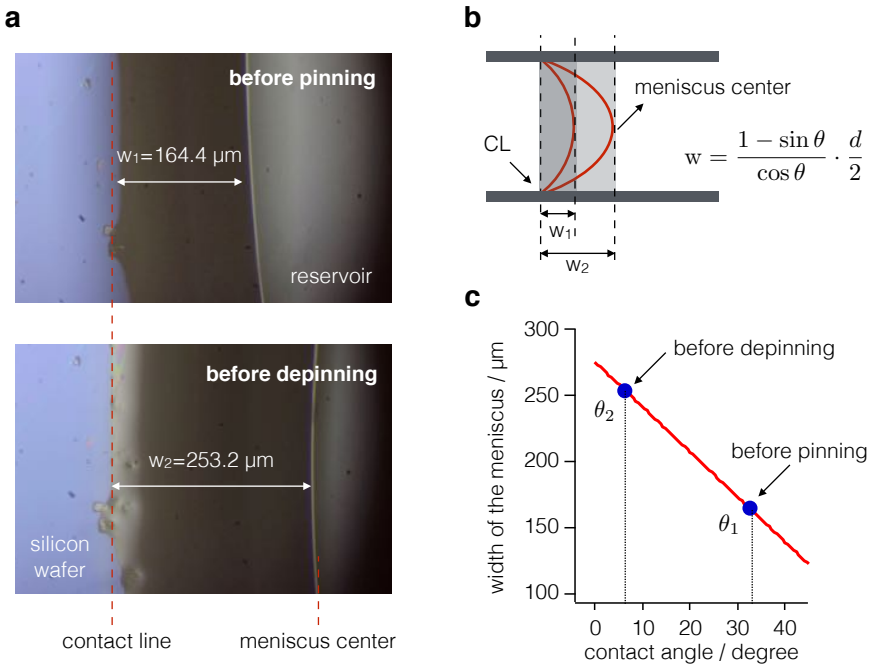


Figure 6.4: The contact angle change on the HMDS-covered surface between pinning and depinning moment. (a) The optic microscope images recorded by the GoPro camera show the width of the meniscus before the pinning and depinning moments. (b) The two-plate geometry for the width of meniscus (w) and the relation between w and the receding contact angle $\theta$. (c) Calculated $\theta_1$ and $\theta_2$ corresponding to the meniscus width $w_1$ and $w_2$ based on the equation in (b).

Now if we put the $\theta_1$ into the function $f(\theta)$ and transfer the unit of rad into degree, the equation 6.3 can be simplified as:

$$\Delta x = -d \times 0.0044 \times \Delta\theta \tag{6.4}$$

where $\Delta\theta = \theta_2 - \theta_1 = -26.3°$, d = 550 µm. The jumping distance $\Delta x$ thus can be calculated as 63.6 µm which is close to our experimental results 58.1±14.3 µm. Such a large $\Delta\theta$ is sufficient to make the contact angle change $\mathrm{d}\theta/\,\mathrm{d}t$ fast enough in order to compete the high evaporation rate of chloroform and pin the CL. According to equation 5.10, the threshold rate of $\mathrm{d}\theta/\,\mathrm{d}t$ here is around -8 °/s which is also reconcilable with the average time interval 3.1 s in this case. In short, the behavior of CL with SWNT-polymer conjugates as deposits and chloroform as solvent can also be well described by the dynamical pinning model we built for the aqueous solution for the two-plate geometry in ambient conditions.

In addition, as we mentioned above, there is also 1 v% ethanol mixed with chloroform before deposition, which is a key factor to fabricate the stripe pattern. This subtle effect is difficult to identify mainly because 0.5-1.0 v% ethanol is originally added even for the ACS grade chloroform as a stabilizer. In order to find the reason and explanation for it, a series of experiments with different ethanol ratios in the HPLC grade chloroform ($\geqq$ 99.9 %) have been accomplished while all of other conditions remained unchanged.

We first use the (6,5) SWNT/PFO-BPy conjugates in chloroform as the suspension. The optical images in Figure 6.5a give the clear change of morphology with the increasing ethanol ratio from null to 12 v%. There is no clear striped pattern without ethanol in the solution and the typical and normal stripes can be only observed when the ethanol content is 1 v%. However, if the ratio of ethanol equals or exceeds 2 v%, the pattern will again vanish. The CL dynamics in Figure 6.5b provide more details. When there is no ethanol, the pinning and depinning process is rare and irregular. But only 1 v% ethanol can make the movement of CL follow the normal coffee stain effect. From 2 v% to 8 v%, the CL moves continuously and leaves film pattern as the images show. However, when the ethanol ratio is as high as 12 v%, the typical pinning and depinning movement appears again. The striped pattern actually can be found in the optical image but the stripes become much broader than that with 1 v% ethanol. This interesting reappearance of coffee stain effect may give us a hint to explain why such a little amount of ethanol can induce the dramatic change of morphology. From the previous research, we have already known that the surface tension of the suspension, the interfacial tension contrast between solid surfaces and the evaporation

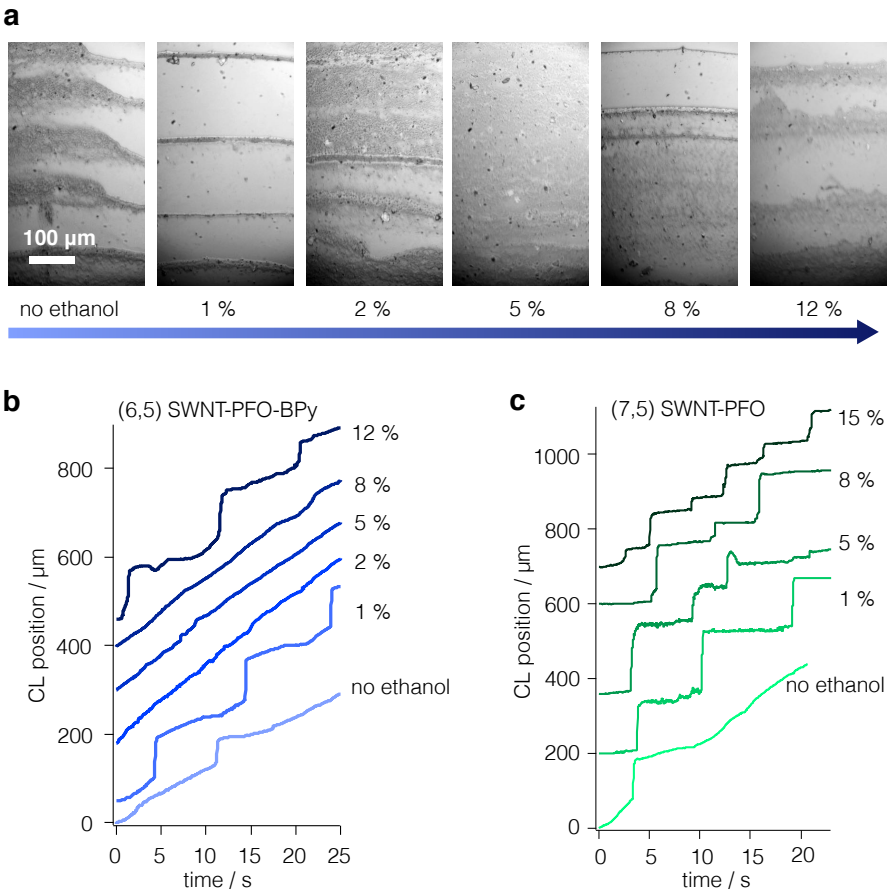


Figure 6.5: The ethanol effect. (a) Along with the increasing ratio of ethanol (from null to 12 v%), the optic microscope images show that the evident change of morphology. The regular stripe pattern only can be fabricated with 1 wt% ethanol. All the suspensions contain the same $0.8 \times 10^{-4}$ wt% (6,5) SWNT/PFO-BPy conjugate and chloroform as solvent. (b) The corresponding CL dynamics from SWNT/PFO-BPy suspensions with different ratios of ethanol. (c) The CL dynamics recorded from the similar experiments but with SWNT/PFO suspensions instead.

rate are supposed to be important factors on this process. The question is how much the 1 v% ethanol can change in the system.

As for the interfacial tension, 1 v% should hardly affect the dispersion of the SWNT-polymer conjugates. The Table 6.1 shows the comparison between chloroform and ethanol in terms of boiling point, surface tension and vapor pressure. The most evident difference is the vapor pressure at room temperature.

| | **chloroform** | **ethanol** |
|---|---|---|
| boiling point | 61.15 ℃ | 78.37 ℃ |
| surface tension (25 ℃) | 26.67 mN/m | 22.39 mN/m |
| vapor pressure (25 ℃) | 25.9 kPa | 7.92 kPa |

Table 6.1: Comparison of several evaporation-related properties between chloroform and ethanol.

The equilibrium vapor pressure of a solvent at certain temperature essentially indicates its evaporation rate which is the key point in the coffee stain effect. Therefore, in order to quantitatively examine the vapor pressure change of the mixture, we take a close look at the phase diagram with the two components. It is shown in Figure 6.6a that the x axis represents the volume ratio of ethanol in liquid (blue curve) and vapor (red curve) phase from zero to 100 v% and y axis is the vapor pressure of the mixed solvent at 25 ℃from 25.9 kPa to 7.92 kPa. The entire trend is easy to understand because ethanol has lower vapor pressure and slower evaporation rate than chloroform so that the vapor pressure of the whole mixed solvent will decrease if the ethanol ratio increases. However, we also notice a interesting turning of pressure in the ethanol range of 1-15 v% which is marked by a gray circle in Figure 6.6a. The detailed data points are shown in Figure 6.6b. It is clear that when the 1 v% ethanol is added in the liquid phase, the corresponding ratio of ethanol in vapor is around 3 v% and the vapor pressure sightly increases to 26.5 kPa. Then if the ratio of ethanol keeps increasing, the vapor pressure will increase as well till the volume ratio in liquid is as high as 5 % after which the pressure starts to decrease. The value of the vapor pressure returns to around 26.5 kPa

when there is 12 v% ethanol in the liquid phase of the mixture. The increasing of vapor pressure means the enhancement of evaporation which could have an effect on the CL movement. The inverted U-shaped turning of vapor pressure here is consistent with the reappearance of coffee stain phenomena from our experimental results in Figure 6.5 in the same component solvent with chloroform and ethanol.

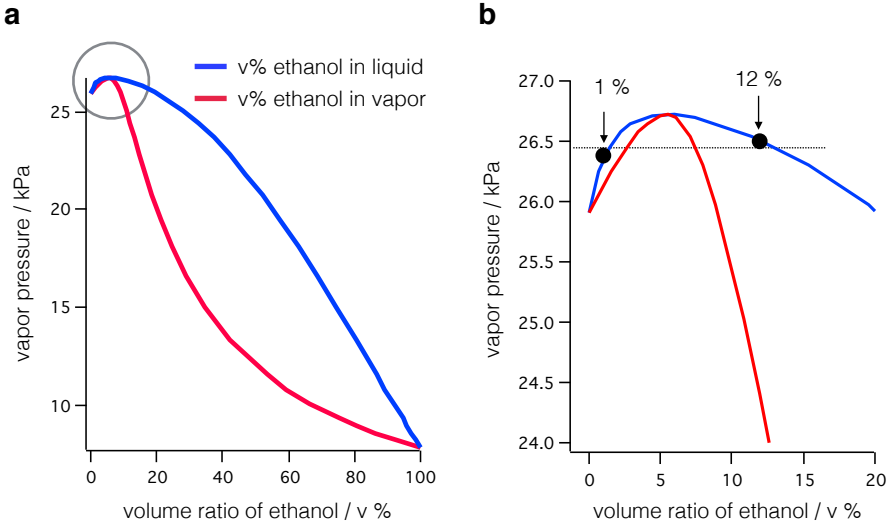


Figure 6.6: (a) The phase diagram of the mixture of chloroform and ethanol at 25 ℃. (b) The range marked by the gray circle in (a).

Although it suggests that a small amount of ethanol enhances the evaporation along the contact line and make the regular stripe pattern, the change of vapor pressure is very small after all. A series of similar experiments with SWNT/PFO conjugates are repeated to further verify it. The results show that the null to 1 v% transition is confirmed whereas the further increasing of ethanol cannot make the stripes subsequently disappear and emerge. The pinning/depinning movement keeps appearing but both the time interval of pinning and the jumping distance of depinning decrease (see Figure 6.5c). Despite that the decreasing of pinning time and depinning distance are also probably due to the enhanced evaporation, still some other parameters might also be changed in the system along with the increasing ethanol. Therefore, except the confirmed important effect of 1 v% ethanol in the process, the va-

por pressure change is one of the possible reasons for the ethanol effect. More comprehensive experiments should be designed and achieved in the future to prove it or find other related factors.

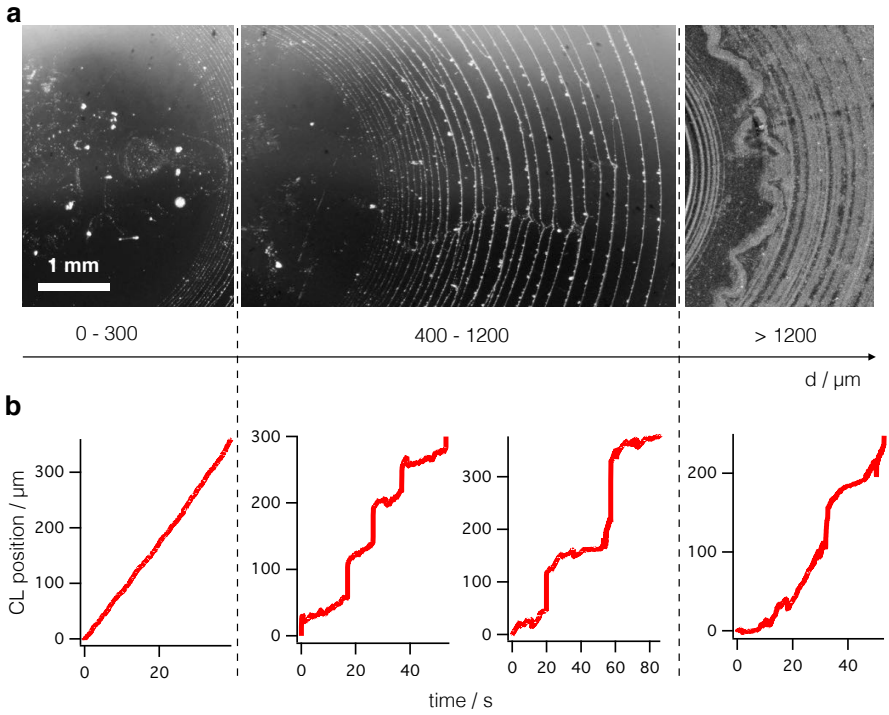


Figure 6.7: (a) The optical images of the ring pattern and the CL dynamics from the edge to the center. The axis below indicates the distance (d) change along the radial direction. (b) The CL dynamics in different ranges of d corresponding to the change of the deposition pattern. The suspension here is $1.6 \times 10^{-4}$ wt% SWNT/PFO conjugates in chloroform with 1 v% ethanol.

The lens setup is applied to study the variation of the CL velocity with the same SWNT/PFO chloroform suspension. As shown by Figure 6.7a, there is a clear pattern of gradient concentric rings which was previously reported under a similar sphere-on-flat geometry [132]. The CL dynamics under the gradually changed distance (d) show the trend from the irregular pinning to

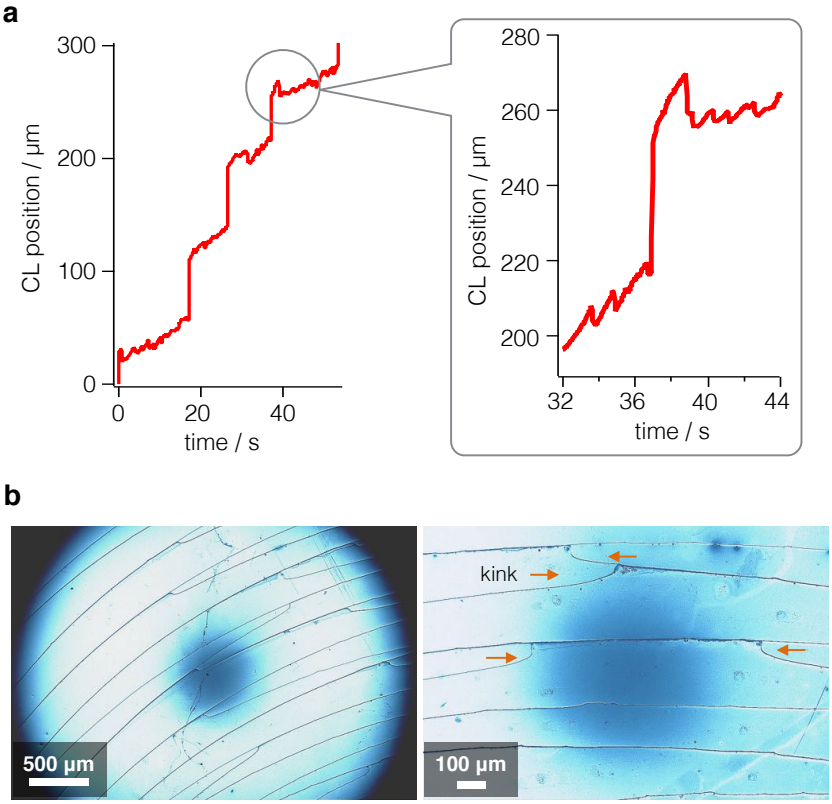


Figure 6.8: (a) The breathing motion of SWNT/PFO conjugate in chloroform. CL dynamics is recored from the fabrication with the lens setup. (b) The bifurcation of stripes due to the typical kink motions during depinning shown by the SEM observation. The arrows indicate the direction of kink propagation. Both of the suspensions here are $0.8 \times 10^{-4}$ wt% SWNT/PFO conjugates in chloroform with 1 v% ethanol.

the continuous moving. When d is between 400-1200 µm, the regular rings can be produced. The pinning time and depinning distance are gradually decreasing as usual because the smaller d gives rise to a enhancement of evaporation. Combing with stripes, this ring-like structure could help to make more complicate and functional patterns in the future.

Last but not least, the breathing motion that represents the dynamical pinning mechanism and the kink which dominates the propagation of the CL can be confirmed with the SWNT/polymer conjugates and chloroform as the solvent. The breathing motion is not easy to be observed because the evaporation rate of chloroform is high enough to endure the decrease of contact angle. But there is still evidence when the velocity of CL becomes slow with the large capillary bridge in lens setup (see Figure 6.8a). The clear breathing motion can be identified if the velocity is as low as about 6 µm/s.

In addition, the typical kink can be found here as the main style of propagation of the CL. The SEM images in Figure 6.8b show the special bifurcation of stripes which is actually due to the kinks. From the previous data, we know that the evaporation rate is very high and it only needs a few seconds to build single stripe. That means if the zipper-like movement is stopped or delayed by some big dirts or aggregates in the stripe for only a few seconds, the deposition will carry on in the middle of the propagation and gives rise to a new and thin stripe between the two regular pinning. Therefore, in order to obtain the extremely standard striped pattern, the kink should be as smooth as possible and the aggregates in the stripe should be eliminated.

To sum up, the distinct SWNT/polymer conjugate suspensions in organic solvents for the coffee stain effect are studied in this section. HMDS covering on the silicon wafer is necessary to establish the interfacial tension contrast due to the low surface tension of the common organic solvents we tried. The chloroform is so far the best option for fabrication of regular striped pattern because of its appropriate thermodynamical properties. A certain amount of ethanol (1 v%) is also very important in the system but the true reason for its effect is still ambiguous. The typical breathing motion and kink are confirmed in the new system, which is consistent with the dynamical pinning discussion concerning about the aqueous solution. The high rate of deposition on one hand could substantially improve the efficiency of fabrication. On the other hand, the local ordering and the homogeneity of the stripes or films are to some extent hindered by the high moving velocity of SWNTs in the suspensions. The role of the polymers playing in the system also needs more experiments to further evaluate because the fine control of their concentrations are absent and their interactions with tubes in the solution are ignored as well.

## 6.2 Thin film formation by dose-controlled, floating evaporative self-assembly

In all of the previous discussions on the EISA process and mechanism, the particles for deposition are always followed the convective flow from the center of the reservoir to the three-phases contact line where the self-assembly happens. In this situation, all of the materials for the fabrication have already been placed in the setup before the self-assembly starts. The fabrication and morphology can only been controlled by the original concentrations of the solutes or other ambient conditions during the evaporation. However, in this section, a different method called dose-controlled floating evaporative self-assembly (DFES) is used to make the striped pattern. The entire methodology is adapted from the paper published recently by Joo *et al.* [43]. The detailed description of the experimental setup can be found in Section 3.4. Schematics in Figure 6.9 here also illustrate the process of deposition step by step.

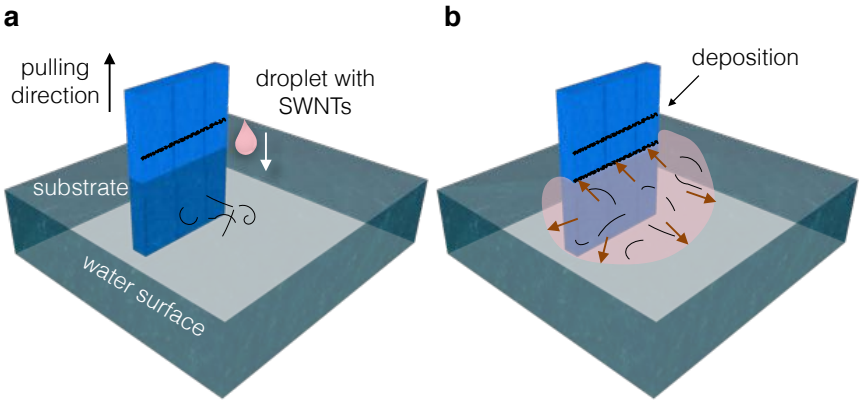


Figure 6.9: Schematic illustration of the iterative process used to fabricate aligned SWNTs driven by the spreading and evaporation of controlled doses of organic solvent at the air/water interface.

At the beginning a droplet from a colloid suspension containing SWNT/polymer conjugates strikes the surface of water (see Figure 6.9a). Due to the relatively low surface tension of the most organic solvents we used here such as chloroform, THF, toluene and chlorobenzene, the droplet on the water surface will

spread immediately as a result of the marangoni effect [107]. As illustrated by Figure 6.9b, the spreading and simultaneous evaporation leads to the deposition on a substrate which is held vertically and immersed partially in water. Well-aligned SWNTs could be found in the stripes after their self-assembly on the water/air interface [43]. The substrate is pulled out from the water surface at certain speed by a home-built dip-coating machine so that the next droplet can make the deposition on a new region. The advantages of this method are that it is able to control the dose of the suspensions in the first place and promotes a more flexible modulation of the properties of stripes. In addition, the number of stripes and the distance between them can be fully controlled by the rate of injection and the pulling speed of the substrate respectively.

Likewise the substrate is cleaned by Piranha solution, then rinsed by HPLC water and finally coated by HMDS. The SWNT suspension is exactly the same with what we used in the last section. The preparation of polymer-wrapped semiconductor SWNTs with single chirality can be found in Section 3.2. Similarly, the interesting ethanol effect will also be discussed here later. Solvents used in this experiment must be almost immiscible with water and their evaporation rates should be cooperated properly with the pulling speed. In this section, we will mainly present two solvents, chloroform for a high evaporation rate and chlorobenzene for a low one.

The results are shown in Figure 6.10 from the colloid suspension containing $4.8 \times 10^{-4}$ wt% SWNT/PFO-BPy conjugates in chloroform and 2 v% ethanol. The pullout speed is fixed as 5 mm/min (around 83 µm/s) based on the parameters from the paper [43]. The droplets (about 2.5 µL per dose) are applied at the certain rate as around 15 drops per minute.

The optical images in Figure 6.10 show the morphological properties of the deposition from the method and materials presented above. One drop here represents one stripe (Figure 6.10a), however in contrast with the two-plate method, the stripes here are not only individual lines from macroscopic observation but covering certain areas the widths of which are typically more than 200 µm. Both the widths of stripe and spacing are around 200 µm which is precisely determined by the dose of droplet and the pullout speed respectively. Furthermore there is obvious inhomogeneity within one stripe. As shown by Figure 6.10b, a typical stripe includes a bright and continuous line in its front and a subsequent dark area coated by relatively sparse deposition. In order to understand the whole process, we need more comprehensive morphological information about the thin film.

A series of SEM images in Figure 6.11 show the detailed morphology of one representative stripe. Because the substrate is pulled up constantly from

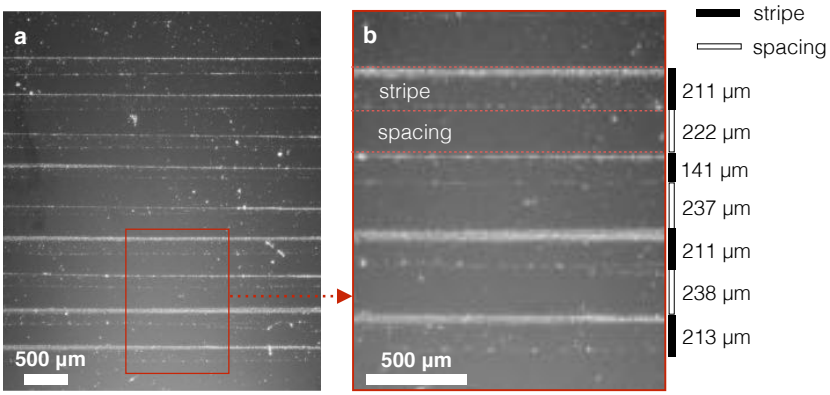


Figure 6.10: Optical images of the stripes recorded by a macro objective (5× magnification) and the GoPro camera. (a) A typical stripe not only contains a line with dense deposition but also covers a less deposited region. (b) An enlarged image shows the regions of stripe and spacing (marked by the red dashes lines). The widths of stripe and spacing are marked and displayed aside by the solid and hollow bars respectively. [SWNT]=$4.8 \times 10^{-4}$ wt%.

the water phase during the deposition, the film morphology can be examined from top to bottom following the chronological order. The iterative structure is shown by Figure 6.11b. Before a new drop is added, there have already been the deposition of SWNTs forming a network. These tubes should be the residue on the water surface left by the evaporation of the last drop as the schematic illustration in Figure 6.9a. Similar with the optical images, the high dense part can be found in the beginning of the stripe region where SWNTs are aligned very well (see Figure 6.11c). However after the 10-20 µm dense deposition, SWNTs on the rest of region whose width usually exceeds 100 µm become again randomly arranged. The density of tubes here is even less than that on the spacing area from water surface. This difference can also be explained by the concept of "rush hour" during depinning [66]. The evaporation rate of the 2 µL chloroform drop is fast according to the recorded movie from GoPro camera. The deposition process including the advancing and receding of the CL lasts within 1 s and the covering width is typically more than 200 µm, which means that the receding velocity of the three phases CL could be as fast as 400 µm/s. Such a high velocity can inevitably lead to

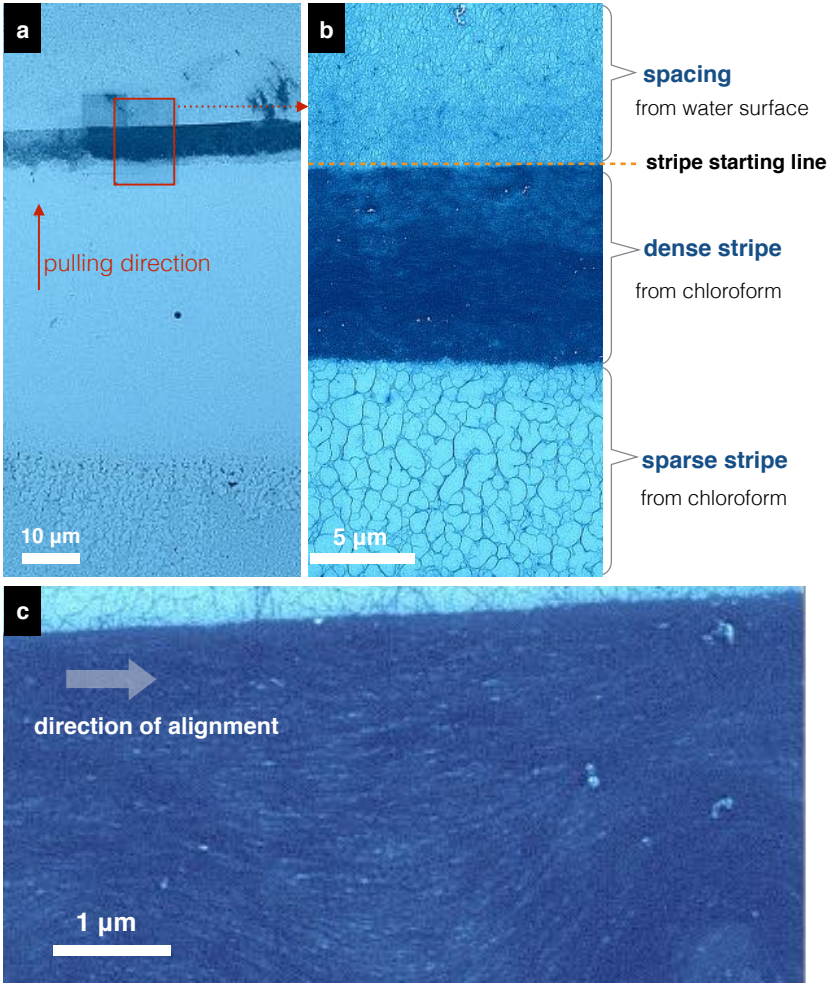


Figure 6.11: SEM images of the structure of a typical stripe. (a) An overall view shows a thin dense stripe between the areas covering by films with randomly deposited SWNTs. (b) The area near the black stripe is focused. A network of SWNTs can be found in the region of spacing. The stripe includes an area of densely well-aligned SWNTs and an loosely linked network of SWNT bundles as well. (c) The dense stripe is zoomed in to show the alignment of SWNTs. [SWNT]=$4.8 \times 10^{-4}$ wt%.

the disorder and loose network of SWNTs. Even if the evaporation of water is much slower than that of chloroform, the residue of SWNTs on water surface has more time to deposit because we used a relatively slow dropping rate (around 5 s per dose).

This inhomogeneity of deposition within a stripe can lead to another situation: a multiple-striped structure. The experimental conditions are maintained and the width of the whole region of the stripe is still in the vicinity of 200 µm as shown by Figure 6.12a. However, the inner structure has changed into many thin stripes covering most of the deposited region. The spacing between the stripes is around 3 µm and the width of them is less than 1 µm (see Figure 6.12c).

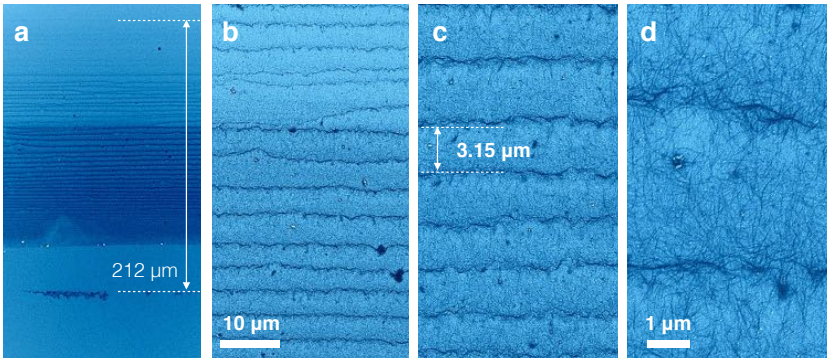


Figure 6.12: SEM images of the multiple stripes from the deposition of one droplet of chloroform. The images are kept zooming in from left to right with magnification 600×, 3000×, 7000×, 22000× respectively. [SWNT]=4.8 × $10^{-4}$ wt%.

Figure 6.12d shows that many tubes spread randomly between these sub stripes which are composed by only several entangled bundles. The multiple sub stripes here remind us the mechanism of pinning/depinning process with the two-plate setup. It implies that the conventional pinning/depinning can be repeated in such a short time and a small region. The sub stripes can be found in most experiments with different concentrations of SWNT, pullout speeds and doses but unfortunately without fixed regularity. Moreover, the morphology of them is not always as homogeneous as what we present in Figure 6.12. In some cases, the single dense stripe appears as usual like Figure 6.11 but was followed by a few thin sub stripes. Given that there

could be so many factors that affect the process, the crucial condition for the formation of subs stripes is still ambiguous. To find out whether it is the similar pinning/depinning process that produces the sub stripes in such short time interval, we use the chlorobenzene as the solvent instead of chloroform to slow down the evaporation.

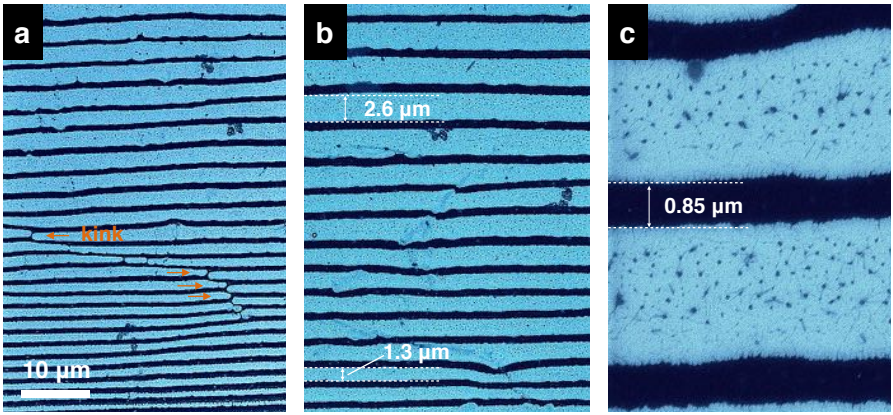


Figure 6.13: SEM images of the multiple stripes from the deposition of one droplet of chlorobenzene. (a) The regular striped pattern covers over 200 µm length and the special morphologies from kinks are marked by the arrows. (b) Depinning distance decreases gradually from top to bottom. (c) The width of the stripes is around 0.8 µm. [SWNT]=$2.0 \times 10^{-4}$ wt%.

In the experiment with chlorobenzene, in order to exclude the effect from the pullout speed and shear force, we stopped the pulling at last, casted one drop and let it evaporate stationary. With the rather lower vapor pressure (1.2 kPa) of chlorobenzene, the evaporation of the same 2 µL droplet can last several minutes. The deposition of this specific drop shown by Figure 6.13 forms a well-regulated striped pattern which has a greater density of SWNTs even with a much smaller concentration ($2.0 \times 10^{-4}$ wt%) than those from chloroform. From the movie recorded by the macro objective and GoPro camera, the typical kink movement can be clearly identified. The special morphology from the delayed zipping is marked in Figure 6.13a exactly like what we have found with two-plate setup before in Figure 6.8b. Another obvious trend is that the width of spacing between the adjacent stripes keeps decreasing from the beginning of evaporation to the end (see Figure 6.13b).

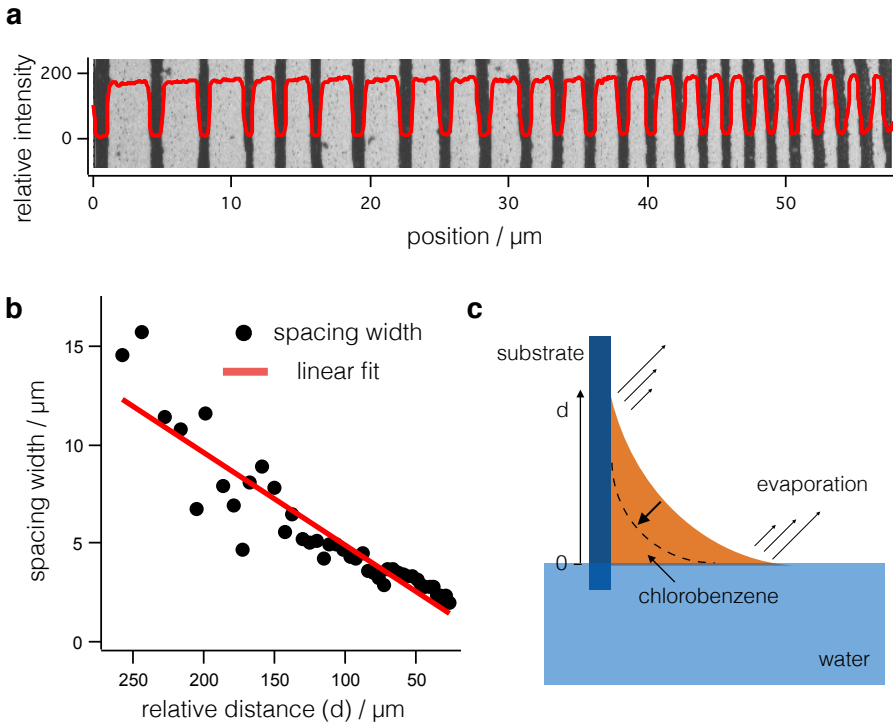


Figure 6.14: (a) Line analysis for the stripes on the SEM image. (b) The width of spacing between two adjacent stripes decreases linearly along with the distance between the CL and water level. (c) Schematic illustration of the geometry of solid substrate, water surface and floating chlorobenzene drop. The dashes curve and the arrow indicate the shrinking of meniscus during the evaporation.

A more specific image line analysis on the spacing width is shown in Figure 6.14. The diagram (see Figure 6.14c) illustrates the evaporation of the suspension on the corner between solid substrate and water surface. An quasi and flexible capillary bridge can be established and held in a small range during the time of evaporation temporarily. The diagram in Figure 6.14c is only for illustrative purpose. The specific shape of the meniscus is actually determined by the competition of the two different capillary forces along the solid substrate and the water surface. If we set the water level as distance zero that is also the where the deposition stops, a relative distance d from a certain stripe to the water level can be easily obtained from the SEM image. The measured d approximately indicates the length of the capillary bridge as an analogy to our previous discussion on the two-plate setup. By the multi-peaks fitting for the result curve of image line analysis (Figure 6.14a), each stripe can be fit well by Gaussian and the widths of stripes are almost maintained (the average FWHM of peak is $0.72 \pm 0.11$ µm). The widths of the spacing between these stripes are plotted against the distance from the CL position to the end of deposition, the water level (see Figure 6.14b).

The linear decreasing here in Figure 6.14b is consistent with the equation mentioned in Chapter 5 for the capillary bridge in two-plate geometry:

$$\Delta x = d_{\text{bridge}} \cdot f(\theta)\Delta\theta \tag{6.5}$$

where the $\Delta x$ is also the spacing width, $f(\theta)$ is only associated with the contact angle, $d_{\text{bridge}}$ is the height of the capillary bridge. With a fixed SWNT concentration, $\Delta\theta$ induced by the contrast of interfacial tension between SWNT-covered and bare surface should maintain constant. Then we obtain the linear relation between $\Delta x$ and $d_{\text{bridge}}$ as well. Although the linear trend is evident, as for the direct quantitative simulation, we have to know the precise change of contact angle for chlorobenzene from SWNT/polymer surface to the HMDS-covered $Si/SiO_2$. That could be a perspective in the future.

A brief summary for this section is that we have tried a well-established method called dose-controlled floating evaporative self-assembly (DFES) which is supposed to precisely control the quality of stripes. Despite that the dense and well-aligned tubes form the stripe in the deposited region, the network contains randomly arranged tubes seems to be inevitable due to the interval deposition from water surface and the "rush hour" effect from too high evaporative velocity. Furthermore, the interesting sub stripes within the deposition of one dose imply that the whole DFES process might follow the coffee stain effect as well. The typical kink and depinning movement were identified not

only by the macroscopic observation but also from the SEM images. Using chlorobenzene as the solvent, the much denser sub stripes show a clear trend that the spacing width is proportional to the CL position relative to the water level which can be analogical to the height of capillary bridge in the conventional two-plate geometry.

Although the dose and morphology are precisely controlled in DFES method, lots of other factors are introduced, some of which such as the ethanol effect, the geometry of meniscus are still ambiguous. There is also a problem on the continuous fabrication because for example when the chloroform is covering the most of the water surface around the substrate, the marangoni effect is suppressed due to the loss of surface tension gradient. The spread of the drop will be hindered and the SWNT cannot reach the substrate then. All of these questions and problems need further research in the future.

## 6.3 Photoluminescence excitation spectroscopy of SWNT stripes and films

Networks or thin films of SWNTs, with their unique electrical, thermal and mechanical properties, offer great potential applications in optoelectronic and photovoltaic devices [153, 154]. Although a concise introduction of SWNT basics has been already provided in Section 2.3, an additional background of its band structure and optical properties will be briefly discussed here.

According to Equation 2.10, a SWNT could be either metallic with (n-m)mod(3)=0 or semiconducting with (n-m)mod(3)=1 or 2 (where mod is "division by modulus"), depending on the chiral angle. The particular interest for optoelectronic applications focuses on semiconducting nanotubes due to their direct bandgap which can be used to both generate and detect light. Therefore all of the discussions here are based on the highly purified (6,5) or (7,5) semiconducting tubes that we prepared from either DGU or polymer-sorting process (see Section 3.1). For a individual semiconducting SWNT, the quasi 1D structure not only leads to a characteristic Density Of States (DOS) distribution but also strongly enhances the binding energies of excitons which act as Coulomb-bound electron-hole pairs [155, 156].

As schematically illustrated in Figure 6.15, the DOS distribution of the carbon nanotubes is dominated by sharp peaks, so-called the van Hove singularities, which are a key feature of the DOS of 1D situation. The energy differences between corresponding van Hove singularities are inversely proportional to the diameter of the tube. Both theoretical and experimental studies show that excitons dominate the optical transitions in SWNTs, due to the strong Coulomb interaction caused by the one-dimensionality and limited screening [157–160]. The first subband exciton binding energy for the (6,5) SWNT could be as large as $E_b \approx 0.4$ electron Volt (eV) [157] and instead of the original free carrier gap ($E_g$) from van Hove singularities, the relevant singlet excitonic states are referred to as $S_1$ and $S_2$. The corresponding absorption spectrum of (6,5) SWNT is shown by Figure 3.3 with exciton resonances $S_1$ at 989 nm (1.25 eV) and $S_2$ at 572 nm (2.17 eV).

The photoluminescence (PL) of the semiconducting SWNT thus can be described by the excitonic transitions. An electron in SWNT absorbs excitation light via $S_2$ transition, resulting in an exciton state. Both electron and hole then rapidly relax to first subband $S_1$ due to an electron-phonon interaction [161]. Spontaneous recombination through $S_1$ transition finally creates the PL. As we mentioned above, the absorption and emission strongly

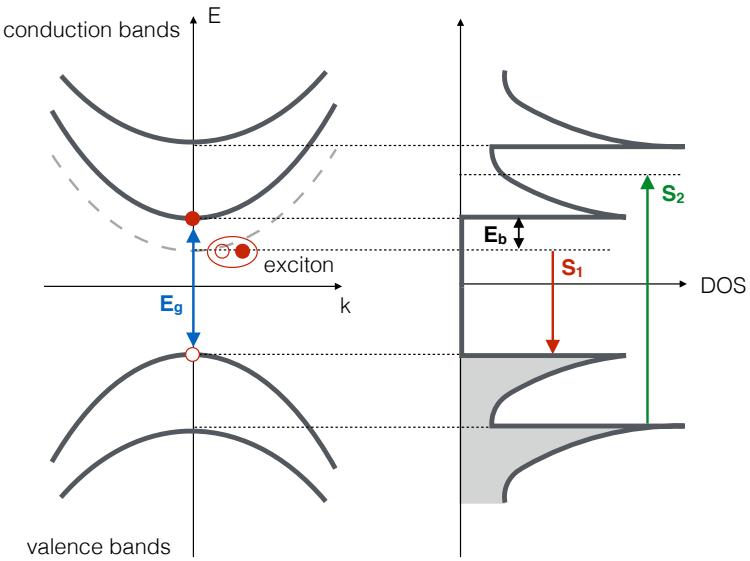


Figure 6.15: Schematic density of states (DOS) and excitonic transitions for the semiconducting SWNT. The hollow and solid red circles represent the hole and electron respectively. $E_g$ is the band gap and $E_b$ the binding energy of the first subband exciton. Solid arrows depict the typical excitonic emission ($S_1$) and absorption ($S_2$) at the exciton states in the first and second subbands respectively.

depends on the chirality of SWNT so that each SWNT species has a specific combination of $S_1$ and $S_2$ as a fingerprint. Photoluminescence excitation (PLE) spectroscopy has been extensively used as a map to identify different semiconducting SWNTs species and probe their electronic structures as well [162–165]. A typical PLE map of (6,5) SWNT in SDS suspension is shown in Figure 6.16. The excitation of $S_2$ exciton and the emission at $S_1$ subband clearly identify the (6,5) SWNT.

The SWNT exciton binding energy strongly depends on the one dimensionality and environmental screening [166]. Therefore when it comes to the device-scale thin film or network of SWNTs, the features of optical optoelectronic properties of the individual tube that we discussed above can be inevitably influenced by intertube interactions and solid substrates.

Using the same (6,5)-enriched SWNT suspension, the striped pattern on

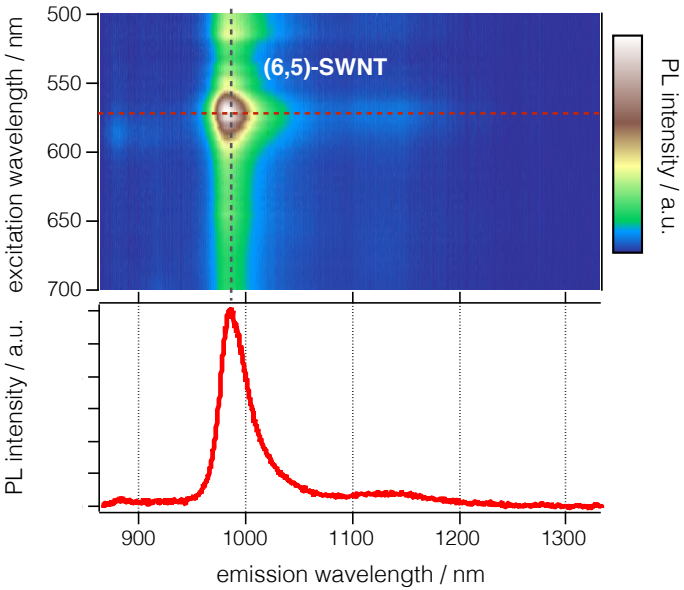


Figure 6.16: PLE map of (6,5) SWNTs in a SDS-dispersed suspension. The PL spectrum beneath is from the cross section of the PLE map with excitation at 570 nm (the red dashed line). The PL emission from the first subband exciton $S_1$ is at around 990 nm wavelength (the black dashed line).

the silicon wafer surface is characterized by the fluorescence microscopy and excitation spectroscopy (see Figure 6.17). The PL image of the striped SWNT pattern in Figure 6.17a clearly demonstrates that the self-assembled SWNT filaments in these structures preserve the semiconducting character of the starting SWNT material. The corresponding PL spectra and PLE map (Figure 6.17b and c) also show the considerable red-shift and broadening of emission features due to the interactions among SWNTs and with the underlying substrate.

With the SWNT selective-sorting technique and solution-processed film fabrication, it is now possible to make mixtures of chirality-specific nanotubes patterns that are spectroscopically isolated [162, 167–169]. The diffusion of excitons along the individual tube or within a bundle of tubes is proved to be as long as 600 nm [170, 171] compared with 5-15 nm in moleculars and

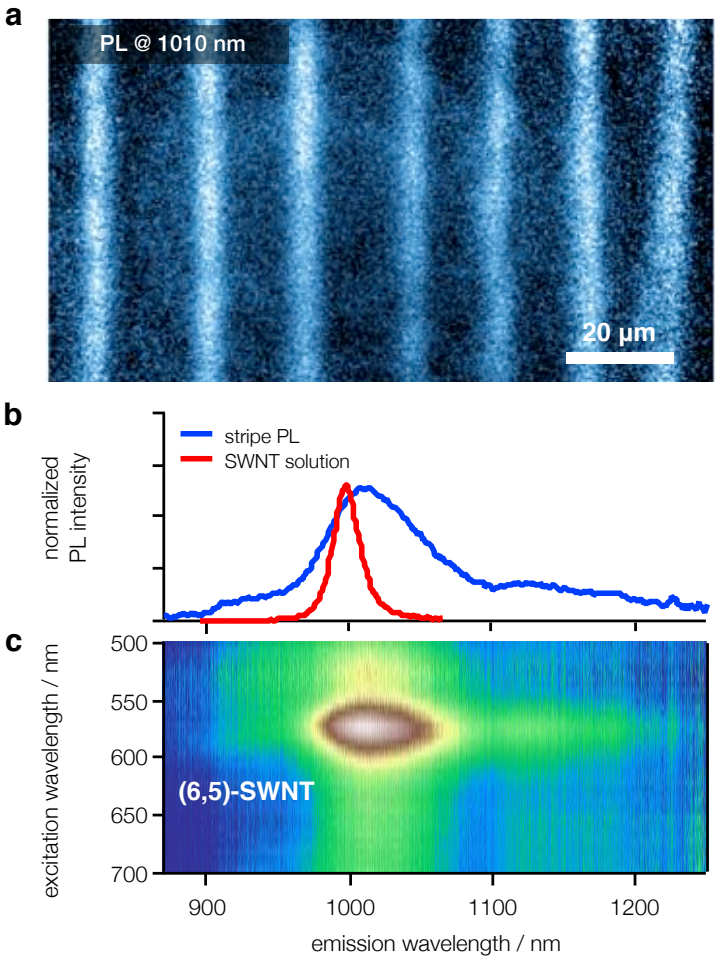


Figure 6.17: PL image and PLE map of (6,5)-SWNT stripes for aqueous suspension. (a) PL image of a stripe pattern recorded for emission from the first subband exciton. The sample is excited by 568 nm irradiation from a supercontinuum light source. (b) PL spectra from the starting material in suspension and the self-assembled film show a clear red-shift of emission on the substrate. (c) PLE map of the same film reveals a broadened (6,5) PL emission feature.

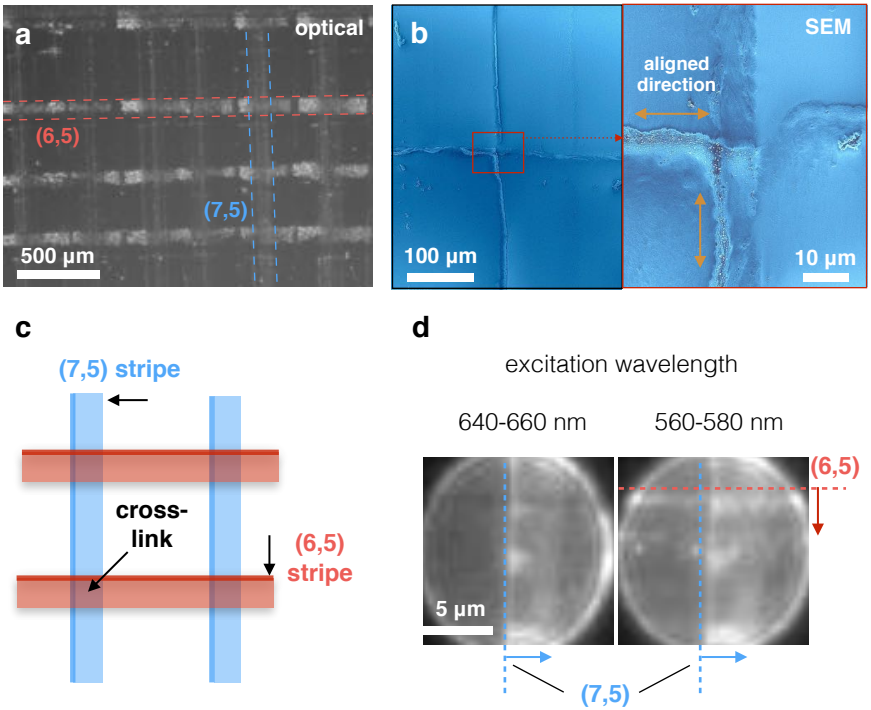


Figure 6.18: (a) Optical image of the (7,5)/(6,5) stripe network. (b) SEM images indicate the alignment of SWNTs at the crosslinked position. (c) The black arrows on the schematic point out the positions measured by the PLE spectroscopy. (d) The PL images of the crosslinked position was excited at different wavelength ranges. Excitation at 640-660 nm shows only PL signal of (7,5) stripe whereas that 560-580 nm shows both (7,5) and (6,5) stripes that perpendicularly cross each other.

polymers [172, 173]. More recently, a research on the coupled semiconducting SWNT thin films has shown that the excitons can transfer rapidly between the densely packed nanotube fibers but in the very porous SWNT films, interfiber transfer is greatly suppressed [167]. The Exciton Energy Transfer (EET) on the intersections of highly packed and oriented SWNT stripes however has not yet been achieved. More interestingly, PLE mapping could possibly provide insight into exciton energy transfer between these mixtures of semiconducting nanotubes with complex structures and controlled band gaps.

By the DFES method described in Section 6.2, a network contains a horizontal striped pattern of (6,5) SWNT/PFOBpy conjugates and a vertical one from (7,5) SWNT/PFO which were fabricated with simply 90° rotation of substrate (Figure 6.18a and b). With the different excitation wavelengths, PL images also prove the perpendicularly overlapped (7,5)/(6,5) stripes at the crosslinked position (Figure 6.18d). In the PL images, the typical structure of stripes from DFES process can be identified as one brightest thin densely aligned SWNTs stripe and a loosely-connected SWNTs film (for corresponding SEM images, see Figure 6.11). The PLE maps were recorded in the regions of highly aligned SWNTs. The representative positions as purified (7,5) or (6,5) stripes and a crosslinked area are pointed out schematically in Figure 6.18c.

The results of PLE maps recorded in these three distinct positions are shown in Figure 6.19 as (a) on a crosslinked site, (b) on a (7,5) SWNT/PFO stripe and (c) on a (6,5) SWNT/PFOBpy stripe. Likewise the broadening emissions from $S_1$ subbands and the red-shift feature can be identified from both types of stripes. Excitation $S_2$ levels are at around 572 nm for (6,5) and 655 nm for (7,5) tubes and the corresponding emission at $S_1$ subbands are at 1004 nm and 1048 nm respectively. Except the main features of excitonic excitation and emission, several sorts of sidebands are also shown in the maps.

First at right side of the $S_1$ emissions, there are two sidebands for both of SWNT types at approximately 100-150 meV below the $S_1$ level (see the yellow arrows on Figure 6.19b and c). These sidebands originate from dipole-forbidden "dark" excitons coupled with $K$-point phonons according to the theoretical prediction from Torrens *et al.* [174] and the experimental result from Maruyama *et al.* [175].

Besides, another two phonon sidebands above the main $S_2$ absorption are indicated by the white arrows (Figure 6.19b and c). These excitonic sidebands are well studied and recognized as strong exciton-phonon coupling to the longitudinal optical phonons near the $\Gamma$ and $K$ point of the graphene Brillouin zone [176, 177]. This excitonic phonon sideband of (7,5) tubes here could inevitably influence the interpretation of EET on the crosslinked site because the expected EET from (6,5) to (7,5) tubes is supposed to be found in the similar excitation wavelength (see the black cross mark in Figure 6.19a). As illustrated by Figure 6.19d, (6,5) tubes have larger $S_1$ and $S_2$ gaps than (7,5) tubes. Therefore, as tubes of both species can be adjacent to one another in this region, $S_2$ excitation of (6,5) tubes as a donor should make EET possible to the (7,5) tube as an acceptor, but not vice versa.

In order to get rid of the influence from the phonon sideband, longitudinal

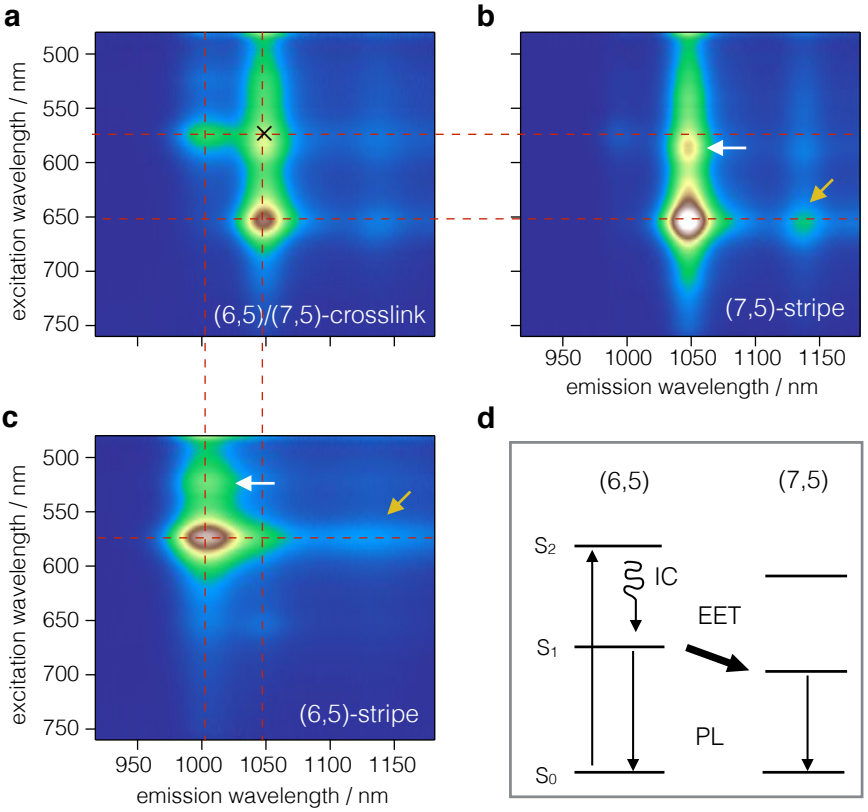


Figure 6.19: Energy transfer in SWNT networks. (a) The PLE map on a crosslinked site. The possible EET position is marked by a black cross. (b) and (c) are the measures of PLE map on the only (7,5) and (6,5) sites as references. Two types of exciton-phonon coupling sidebands are indicated by the white and yellow arrows respectively. (d) A Jablonski diagram illustrates the relevant photophysical process.

cross sections from the PLE maps of crosslink and (7,5) stripe at 1048 nm emission wavelength are extracted respectively and normalized for comparison (Figure 6.20a). The curve from the subtraction between the two normalized spectrums of crosslink and (7,5) stripe indicates the typical EET with absorption at 572 nm and emission at 1048 nm (Figure 6.20b), same as the position that marked by the cross on the PLE map in Figure 6.19a.

To sum up briefly, although the results of PLE maps show that the EET process happens between adjacent tubes at the crosslinked sites, the overlapping (7,5) phonon sideband hinders the further quantitative analysis. Combination of other species of semiconducting tubes like (9,4), (7,6) or (8,4) could be more appropriate for the EET identification instead of (7,5)/(6,5) crosslink due to the much less effect of phonon sidebands [162].

What's more, in order to clarify the effect from the alignment, the crossed stripes could be exploited in polarized PLE spectroscopy. Because optical transitions induced by light polarized along the tube axis can be much stronger than the perpendicular excitation due to the one dimensionality [178, 179], it should therefore be possible to excite only single species in one stripe selec-

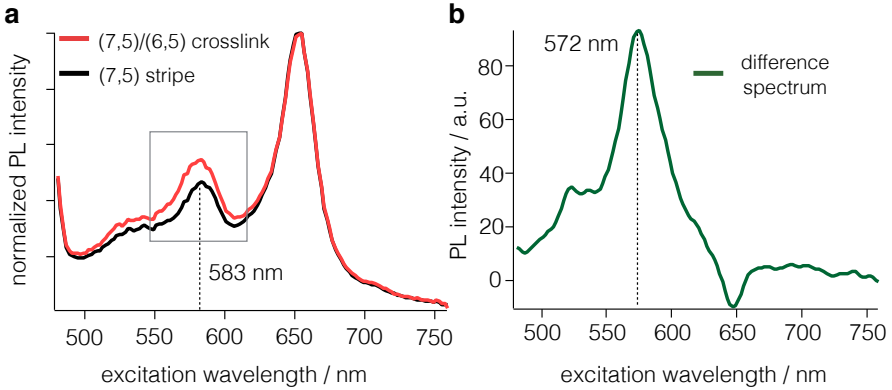


Figure 6.20: (a) Comparison of PLE spectra of crosslink and (7,5) stripe at the $S_1$ emission energy of (7,5) tubes. Each PLE spectrum was recorded along the PL emission wavelength 1048 nm and normalized at the excitation peak of 655 nm. The peaks including phonon sidebands (583 nm) and possible EET are marked by a rectangle. (b) The spectra indicates the difference between the two curves in (a). The dominating peak at 572 nm clearly represents the EET.

tively. If so, the requirement for the sample preparation will be stricter. The alignment of SWNTs within stripes should be well controlled and the random tubes without stripes must be eliminated by improving the so-called DFES technique or simply using other EISA methods in the future.

# 7 Summary

In summary, we have prepared single-wall carbon nanotube (SWNT) thin films by the method of evaporation-induced self-assembly (EISA). Using the scalable two-plate or lens setups, sorts of different film types or patterns of SWNTs has been successfully fabricated directly from the evaporation of solvents and could be precisely controlled by the concentrations of SWNT in ambient conditions. The special geometry of meniscus as the capillary bridge has not only given rise to a much higher efficiency of fabrication than what previously reported [33, 35] but also allowed us to monitor the pinning and depinning process carefully and further investigate the mechanism underlying the formation of different film morphologies.

In contrast with the conventional "stick-slip" model [40], we have provided the new dynamical pinning and zipping model for the contact line (CL) behavior. By analyzing the motion of CL and varying deposited patterns, the traditionally so-called "stick" state should be treated as a dynamical pinning process due to the interfacial tension contrast between SWNT-covered and bare silicon surface. Besides, the plausible one-step "slip" motion could be dominated by the zipping-like kink propagation.

In addition, the experiments with heated substrates at higher temperatures between 30 ℃ and 50 ℃ have shown that the striped pattern could be fabricated by both much lower SWNT and SDS concentrations than that in room temperature, which is consistent with our model of interfacial tension contrast. In this situation, the deposition rate was increased but the quality of SWNT alignment was undermined because the corresponding moving velocity of SWNT was also too fast for SWNTs to rotate when the evaporative rate was high.

The similar results were identified by the SWNT/polymer conjugates dispersed in chloroform under the similar setups and other identical conditions. The typical breathing motion of dynamical pinning and zipping-like propagation for depinning were confirmed by the new suspensions despite that some morphological parameters changed dramatically compared with that from the aqueous solution. For example, the spacing between stripes reached 100 µm $\sim$ 200 µm because the large contact angle contrast between HDMS- and SWNT-

covered surface accompanies with the high evaporation rate of chloroform in the pinning and depinning process. Likewise the average CL velocity for fabrication reached around 20 µm/s due to the much higher evaporation rate of chloroform than water.

Using alike suspensions, the modified EISA method called dose-controlled floating evaporative self-assembly (DFES) was employed to implement the self-assembly of SWNTs on the water/air interface and then deposit them on solid substrate by directed floating. The method was adapted from the work that Anorld *et al.* published before [43]. Although the stripes were fabricated successfully by drops with certain doses and SWNT concentrations, there inevitably existed randomly oriented SWNTs from the water surface that built networks between the stripes containing well-aligned tubes. In order to slow down the evaporation rate and monitor the process detailedly, we used chlorobenzene as the solvent instead of chloroform and find the typical pinning/depinning movement of the CL. A preliminary analysis of the results in terms of chlorobenzene implied that the CL possibly followed the similar pinning/depinning process in consistence with our model with capillary bridge.

In the last part of the thesis, the primary research on the optical properties of these stripes of ultrahigh purity semiconducting nanotubes was conducted by fluorescence microscopy and photoluminescence excitation (PLE) spectroscopy. The energy transfer of the photogenerated excitons was confirmed between different tube species with controlled band gaps.

In short, the experiments performed in this thesis allowed to gain new insights about the fabrication of large-area SWNT thin films by the cost-effective solution-processed method and most importantly to uncover its intrinsic mechanism as well. Combined with the separation and selection technique like density gradient centrifugation or polyfluorene derivatives assisted method, highly monodisperse semiconducting nanotubes could be deposited into organized, controllable and functional arrays.

Beyond the ambient conditions, precise control for the evaporation under preset temperature and vapor pressure could possibly extend the technique to the industry level. Assisted by some other mature techniques such as roll-to-roll printing, the cost-effective method could be widely used in the manufacture of various thin film devices. More complex 2D or even three-dimensional (3D) structures could be designed and accomplished by the method for the functional or stretchable requirements. Further research on the fundamental exciton transition and diffusion in different networks or structures of SWNTs will be the significant precondition for the real applications.

Looking ahead, from the individual carbon nanotube to its thin film, this promising material with outstanding properties had many challenges to overcome before the real-world applications. Thanks to the availability of pure and well-defined materials, the scalable solution-processed approaches for fabrication of thin films should be able to unlock the potential of carbon nanotubes and exploit them in (opto-)electronic devices in the foreseeing future.

# 8 Zusammenfassung

Im Rahmen der vorliegenden Arbeit wurden über die Methode der Verdunstungsinduzierten Selbstanordnung (evaporation-induced self-assembly, EISA) dünne Filme aus einwandigen Kohlenstoffnanoröhren (SWNTs) hergestellt. Die Verwendung eines individuell anpassbaren Zwei-Platten- oder Linsen-Aufbaus ermöglichte durch präzise Kontrolle der Konzentrationen der verwendeten SWNT-Suspensionen und der unterschiedlichen Reaktionsbedingungen die Herstellung verschiedenster Arten und Anordnungen von SWNT-Dünnfilmen. Durch Ausnützen der speziellen Geometrie des Meniskus einer Kapillarbrücke zwischen zwei Oberflächen konnte nicht nur eine effizientere Herstellung im Vergleich zu früheren Veröffentlichungen [33,35] erzielt werden, sondern es konnte auch der Mechanismus der Selbstanordnung (Pinning und Depinning) in Abhängigkeit der Reaktionsbedingungen und die resultierende Dünnfilmmorphologie untersucht werden.

Es konnte gezeigt werden, dass im Gegensatz zum gängigen "stick-slip" Modell [40] durch ein dynamisches Reißverschluss-Modell (dynamical pinning and zipping model) das Verhalten an der Kontaktlinie (contact line, CL) besser beschrieben werden kann. Eine Analyse der CL-Bewegung unter unterschiedlichen Abscheidungsbedingungen führte zu dem Schluss, dass der bisher verwendete "Stick"-Zustand als dynamischer Pinning-Zustand betrachtet werden sollte, dessen Zustandekommen auf der unterschiedlichen Oberflächenspannung zwischen SWNT-bedeckten und -freien Bereichen auf der Abscheidungsoberfläche beruht. Beim bisher als einschrittige "Slip"-Bewegung beschriebenen Fortschreiten der CL ist dagegen eine Reißverschluss-ähnliche Knick-Bewegung vorherrschend.

Weiterführende temperaturabhängige Abscheidungsstudien zur Dünnfilmpräparation konnten zeigen, dass Dünnfilme in Streifenanordnung bei wesentlich geringeren SWNT- und Seifenkonzentrationen im Vergleich zu Raumtemperatur hergestellt werden können. Auch diese Prozesse konnten durch das oben beschriebene Oberflächenspannungskontrastmodell erklärt werden. Die Abscheidungsrate nimmt mit höherer Temperatur zu, wobei die Ordnung der abgeschiedenen SWNTs im Dünnfilm abnimmt, da die Bewegungsgeschwindigkeit hin zur CL im Vergleich zur Rotationsgeschwindigkeit

stark zunimmt.

Auch für SWNT/Polymer Suspensionen in organischen Lösungsmitteln konnte das Verhalten der CL nach dem dynamischen Reißverschluss-Modell erklärt werden und gestreifte Dünnfilme hergestellt werden. Die Filmmorphologie und der Streifenabstand unterschieden sich jedoch maßgeblich von denen aus wässrigen SWNT Suspensionen hergestellten Dünnfilmen. Hierfür ist auch die mit 20 µm/s sehr hohe Herstellungsgeschwindigkeit verantwortlich.

Unter Verwendung der organischen SWNT Suspensionen wurden auch Experimente zu einer von EISA entlehnten Abscheidungsmethode (dose-controlled floating evaporative self-assembly, DFES) [43] durchgeführt. Hierbei wurden gestreifte SWNT Dünnfilme durch SWNT-Selbstanordnung schwimmend an der Flüssig/Luft-Grenzfläche und anschließender Abscheidung auf festem Substrat hergestellt. Auch hier konnte ein CL-verhalten, welches dem dynamischen Reißverschluss-Modell folgt nachgewiesen werden. Detailliertere Betrachtung des Zwischenstreifenraumes zeigte jedoch willkürlich angeordnete SWNTs unabhängig der Herstellungsparameter.

Im letzten Teil der Dissertation wurden mittels Fluoreszenz-Anregungs-Spektroskopie und Fluoreszenzmikroskopie die optischen Eigenschaften der Streifen-Dünnfilme, bestehend aus hochaufgereinigten halbleitenden SWNTs untersucht. Bei Streifenmustern aus unterschiedlichen SWNT Spezies konnte ein Energietransfer der exzitonischen angeregten Zustände zwischen SWNTs mit unterschiedlicher Bandlücke nachgewiesen werden.

Zusammengefasst lässt sich sagen, dass die im Rahmen dieser Dissertation durchgeführten Experimente ein tieferes Verständnis der Herstellung großflächiger SWNT Dünnfilme durch Entdeckung des zugrundeliegenden Mechanismus ermöglichten. In Kombination mit Auftrennungsverfahren wie Dichtegradientenultrazentrifugation oder Polymer-basierten Ansätzen können so monodisperse, halbleitende SWNTs kontrolliert zu geordneten, funktionellen Arrays angeordnet werden.

Präzise Kontrolle der Umgebungsbedingungen, wie Temperatur oder Druck, könnten die Technik auch für industrielle Anwendung interessant machen. Unterstützt durch etablierte Methoden wie dem Rollendruck könnte die kostengünstige Methode großflächig zur Herstellung von verschiedenen Dünnfilmen zur Anwendung kommen. Komplexere, funktionelle, dehnbare 2D oder 3D Strukturen könnten so entworfen werden. Weitere Untersuchungen hinsichtlich der exzitonischen Übergänge und Exzitondiffusion in solchen SWNT-Netzwerken oder -Strukturen wären die Grundvoraussetzung für tatsächliche Anwendungsmöglichkeiten.

Vorausschauend lässt sich sagen, dass auf dem Weg von der individuellen Nanoröhre hin zu SWNT Dünnfilmen noch zahlreiche Herausforderungen bestehen, bevor eine reale Anwendung dieser vielversprechenden Materialien möglich erscheint. Durch hochreines und wohldefiniertes Ausgangsmaterial könnte die frei skalierbare Herstellung von SWNT Dünnfilmen über die hier beschriebenen Methoden aber eine Anwendungsmöglichkeit für das lange prognostizierte Potential der Kohlenstoffnanoröhren in (opto-)elektronischen Vorrichtungen in näherer Zukunft ermöglichen.

# Bibliography


[1] Erik T Thostenson, Zhifeng Ren, and Tsu-Wei Chou. Advances in the science and technology of carbon nanotubes and their composites: a review. *Composites science and technology*, 61(13):1899–1912, 2001.

[2] Hongjie Dai, Eric W Wong, and Charles M Lieber. Probing electrical transport in nanomaterials: conductivity of individual carbon nanotubes. *Science*, 272(5261):523–526, 1996.

[3] Xinjian Zhou, Ji-Yong Park, Shaoming Huang, Jie Liu, and Paul L McEuen. Band structure, phonon scattering, and the performance limit of single-walled carbon nanotube transistors. *Physical Review Letters*, 95(14):146805, 2005.

[4] Feng Wang, Gordana Dukovic, Louis E Brus, and Tony F Heinz. The optical resonances in carbon nanotubes arise from excitons. *Science*, 308(5723):838–841, 2005.

[5] Silvia M Santos, Bertrand Yuma, Stéphane Berciaud, Jonah Shaver, Mathieu Gallart, Pierre Gilliot, Laurent Cognet, and Brahim Lounis. All-optical trion generation in single-walled carbon nanotubes. *Physical review letters*, 107(18):187401, 2011.

[6] Richard Martel, T Schmidt, HR Shea, T Hertel, and Ph Avouris. Single- and multi-wall carbon nanotube field-effect transistors. *Applied Physics Letters*, 73(17):2447–2449, 1998.

[7] Jing Kong, Nathan R Franklin, Chongwu Zhou, Michael G Chapline, Shu Peng, Kyeongjae Cho, and Hongjie Dai. Nanotube molecular wires as chemical sensors. *Science*, 287(5453):622–625, 2000.

[8] E Kymakis and GAJ Amaratunga. Single-wall carbon nanotube/conjugated polymer photovoltaic devices. *Applied Physics Letters*, 80(1):112–114, 2002.

[9] Qing Cao, Hoon-sik Kim, Ninad Pimparkar, Jaydeep P Kulkarni, Congjun Wang, Moonsub Shim, Kaushik Roy, Muhammad A Alam, and John A Rogers. Medium-scale carbon nanotube thin-film integrated circuits on flexible plastic substrates. *Nature*, 454(7203):495–500, 2008.

[10] Max M Shulaker, Gage Hills, Nishant Patil, Hai Wei, Hong-Yu Chen, H-S Philip Wong, and Subhasish Mitra. Carbon nanotube computer. *Nature*, 501(7468):526–530, 2013.

[11] Yabin Chen, Yingying Zhang, Yue Hu, Lixing Kang, Shuchen Zhang, Huanhuan Xie, Dan Liu, Qiuchen Zhao, Qingwen Li, and Jin Zhang. State of the art of single-walled carbon nanotube synthesis on surfaces. *Advanced Materials*, 26(34):5898–5922, 2014.

[12] Lei Ding, Alexander Tselev, Jinyong Wang, Dongning Yuan, Haibin Chu, Thomas P McNicholas, Yan Li, and Jie Liu. Selective growth of well-aligned semiconducting single-walled carbon nanotubes. *Nano letters*, 9(2):800–805, 2009.

[13] Jing Lu, Lin Lai, Guangfu Luo, Jing Zhou, Rui Qin, Dan Wang, Lu Wang, Wai Ning Mei, Guangping Li, Zhengxiang Gao, et al. Why semiconducting single-walled carbon nanotubes are separated from their metallic counterparts. *Small*, 3(9):1566–1576, 2007.

[14] Weiwei Zhou, Shutong Zhan, Lei Ding, and Jie Liu. General rules for selective growth of enriched semiconducting single walled carbon nanotubes with water vapor as in situ etchant. *Journal of the American Chemical Society*, 134(34):14019–14026, 2012.

[15] Jie Liu and Mark C Hersam. Recent developments in carbon nanotube sorting and selective growth. *MRS bulletin*, 35(04):315–321, 2010.

[16] Michael S Arnold, Samuel I Stupp, and Mark C Hersam. Enrichment of single-walled carbon nanotubes by diameter in density gradients. *Nano Letters*, 5(4):713–718, 2005.

[17] Michael S Arnold, Alexander A Green, James F Hulvat, Samuel I Stupp, and Mark C Hersam. Sorting carbon nanotubes by electronic structure using density differentiation. *Nature nanotechnology*, 1(1):60–65, 2006.

[18] Mildred S Dresselhaus, Gene Dresselhaus, PC Eklund, and AM Rao. *Carbon nanotubes*. Springer, 2000.

[19] Mark C Hersam. Progress towards monodisperse single-walled carbon nanotubes. *Nature Nanotechnology*, 3(7):387–394, 2008.

[20] Adrian Nish, Jeong-Yuan Hwang, James Doig, and Robin J Nicholas. Highly selective dispersion of single-walled carbon nanotubes using aromatic polymers. *Nature Nanotechnology*, 2(10):640–646, 2007.

[21] Gang Li, Vishal Shrotriya, Jinsong Huang, Yan Yao, Tom Moriarty, Keith Emery, and Yang Yang. High-efficiency solution processable polymer photovoltaic cells by self-organization of polymer blends. *Nature materials*, 4(11):864–868, 2005.

[22] David Grosso, Florence Cagnol, GJ de AA Soler-Illia, Eduardo L Crepaldi, Heinz Amenitsch, Aline Brunet-Bruneau, Alexi Bourgeois, and Clement Sanchez. Fundamentals of mesostructuring through evaporation-induced self-assembly. *Advanced Functional Materials*, 14(4):309–322, 2004.

[23] C Jeffrey Brinker, Yunfeng Lu, Alan Sellinger, and Hongyou Fan. Evaporation-induced self-assembly: nanostructures made easy. *Advanced materials*, 11(7):579–585, 1999.

[24] GJ de AA Soler-Illia, A Louis, and C Sanchez. Synthesis and characterization of mesostructured titania-based materials through evaporation-induced self-assembly. *Chemistry of Materials*, 14(2):750–759, 2002.

[25] Torsten Brezesinski, Matthijs Groenewolt, Alain Gibaud, Nicola Pinna, Markus Antonietti, and B Smarsly. Evaporation-induced self-assembly (eisa) at its limit: Ultrathin, crystalline patterns by templating of micellar monolayers. *Advanced Materials*, 18(17):2260–2263, 2006.

[26] Yunfeng Lu, Hongyou Fan, Aaron Stump, Timothy L Ward, Thomas Rieker, and C Jeffrey Brinker. Aerosol-assisted self-assembly of mesostructured spherical nanoparticles. *Nature*, 398(6724):223–226, 1999.

[27] Robert D Deegan, Olgica Bakajin, Todd F Dupont, Greb Huber, Sidney R Nagel, and Thomas A Witten. Capillary flow as the cause of ring stains from dried liquid drops. *Nature*, 389(6653):827–829, 1997.

[28] Henning Sirringhaus. Device physics of solution-processed organic field-effect transistors. *Advanced Materials*, 17(20):2411–2425, 2005.

[29] Sang Hyun Park, Dong Qin, and Younan Xia. Crystallization of mesoscale particles over large areas. *Advanced Materials*, 10(13):1028–1032, 1998.

[30] Beng S Ong, Chensha Li, Yuning Li, Yiliang Wu, and Rafik Loutfy. Stable, solution-processed, high-mobility zno thin-film transistors. *Journal of the American Chemical Society*, 129(10):2750–2751, 2007.

[31] Robert D Deegan. Pattern formation in drying drops. *Physical review E*, 61(1):475, 2000.

[32] William R Small, Chris D Walton, Joachim Loos, and Marc in het Panhuis. Carbon nanotube network formation from evaporating sessile drops. *The Journal of Physical Chemistry B*, 110(26):13029–13036, 2006.

[33] Michael Engel, Joshua P Small, Mathias Steiner, Marcus Freitag, Alexander A Green, Mark C Hersam, and Phaedon Avouris. Thin film nanotube transistors based on self-assembled, aligned, semiconducting carbon nanotube arrays. *Acs Nano*, 2(12):2445–2452, 2008.

[34] Qingwen Li, Yuntian T Zhu, Ian A Kinloch, and Alan H Windle. Self-organization of carbon nanotubes in evaporating droplets. *The Journal of Physical Chemistry B*, 110(28):13926–13930, 2006.

[35] Tejas A Shastry, Jung-Woo T Seo, Josue J Lopez, Heather N Arnold, Jacob Z Kelter, Vinod K Sangwan, Lincoln J Lauhon, Tobin J Marks, and Mark C Hersam. Large-area, electronically monodisperse, aligned single-walled carbon nanotube thin films fabricated by evaporation-driven self-assembly. *small*, 9(1):45–51, 2013.

[36] Gerald J Brady, Yongho Joo, Meng-Yin Wu, Matthew J Shea, Padma Gopalan, and Michael S Arnold. Polyfluorene-sorted, carbon nanotube array field-effect transistors with increased current density and high on/off ratio. *ACS nano*, 8(11):11614–11621, 2014.

[37] Gerald J Brady, Yongho Joo, Susmit Singha Roy, Padma Gopalan, and Michael S Arnold. High performance transistors via aligned polyfluorene-sorted carbon nanotubes. *Applied Physics Letters*, 104(8):083107, 2014.

[38] Satoshi Watanabe, Koji Inukai, Shunsuke Mizuta, and Minoru T Miyahara. Mechanism for stripe pattern formation on hydrophilic surfaces by using convective self-assembly. *Langmuir*, 25(13):7287–7295, 2009.

[39] Philip Born, Susanne Blum, Andres Munoz, and Tobias Kraus. Role of the meniscus shape in large-area convective particle assembly. *Langmuir*, 27(14):8621–8633, 2011.

[40] Martin ER Shanahan. Simple theory of" stick-slip" wetting hysteresis. *Langmuir*, 11(3):1041–1043, 1995.

[41] Anaïs Gauthier, Marco Rivetti, Jérémie Teisseire, and Etienne Barthel. Role of kinks in the dynamics of contact lines receding on superhydrophobic surfaces. *Physical review letters*, 110(4):046101, 2013.

[42] Renaud Dufour, Philippe Brunet, Maxime Harnois, Rabah Boukherroub, Vincent Thomy, and Vincent Senez. Zipping effect on omniphobic surfaces for controlled deposition of minute amounts of fluid or colloids. *Small*, 8(8):1229–1236, 2012.

[43] Yongho Joo, Gerald J Brady, Michael S Arnold, and Padma Gopalan. Dose-controlled, floating evaporative self-assembly and alignment of semiconducting carbon nanotubes from organic solvents. *Langmuir*, 30(12):3460–3466, 2014.

[44] Ying Diao, Leo Shaw, Zhenan Bao, and Stefan CB Mannsfeld. Morphology control strategies for solution-processed organic semiconductor thin films. *Energy & Environmental Science*, 7(7):2145–2159, 2014.

[45] Richard R Lunt, Jay B Benziger, and Stephen R Forrest. Relationship between crystalline order and exciton diffusion length in molecular organic semiconductors. *Advanced Materials*, 22(11):1233–1236, 2010.

[46] Shoushan Fan, Michael G Chapline, Nathan R Franklin, Thomas W Tombler, Alan M Cassell, and Hongjie Dai. Self-oriented regular arrays of carbon nanotubes and their field emission properties. *Science*, 283(5401):512–514, 1999.

[47] Yoichi Murakami, Shohei Chiashi, Yuhei Miyauchi, Minghui Hu, Masaru Ogura, Tatsuya Okubo, and Shigeo Maruyama. Growth of vertically aligned single-walled carbon nanotube films on quartz substrates and their optical anisotropy. *Chemical Physics Letters*, 385(3):298–303, 2004.

[48] Julie A Bardecker, Ali Afzali, George S Tulevski, Teresita Graham, James B Hannon, and Alex K-Y Jen. Directed assembly of single-walled carbon nanotubes via drop-casting onto a uv-patterned photosensitive monolayer. *Journal of the American Chemical Society*, 130(23):7226–7227, 2008.

[49] Marta Mas-Torrent and Concepcio Rovira. Novel small molecules for organic field-effect transistors: towards processability and high performance. *Chemical Society Reviews*, 37(4):827–838, 2008.

[50] Hoi Nok Tsao and Klaus Müllen. Improving polymer transistor performance via morphology control. *Chemical Society Reviews*, 39(7):2372–2386, 2010.

[51] Alberto Salleo, R Joseph Kline, Dean M DeLongchamp, and Michael L Chabinyc. Microstructural characterization and charge transport in thin films of conjugated polymers. *Advanced Materials*, 22(34):3812–3838, 2010.

[52] DH Kim, JOONG TARK Han, YD Park, Yunseok Jang, JH Cho, Minkyu Hwang, and Kilwon Cho. Single-crystal polythiophene microwires grown by self-assembly. *Advanced Materials*, 18(6):719–723, 2006.

[53] Peter J Diemer, Christopher R Lyle, Yaochuan Mei, Christopher Sutton, Marcia M Payne, John E Anthony, Veaceslav Coropceanu, Jean-Luc Brédas, and Oana D Jurchescu. Vibration-assisted crystallization improves organic/dielectric interface in organic thin-film transistors. *Advanced Materials*, 25(48):6956–6962, 2013.

[54] Svetlana Karabasheva, Stanislav Baluschev, and Karlheinz Graf. Microstructures on soluble polymer surfaces via drop deposition of solvent mixtures. *Applied physics letters*, 89(3):031110, 2006.

[55] Nam Joong Jeon, Jun Hong Noh, Young Chan Kim, Woon Seok Yang, Seungchan Ryu, and Sang Il Seok. Solvent engineering for high-performance inorganic–organic hybrid perovskite solar cells. *Nature materials*, 2014.

[56] Joonhyung Park, Sangwoon Lee, and Hong H Lee. High-mobility polymer thin-film transistors fabricated by solvent-assisted drop-casting. *Organic electronics*, 7(5):256–260, 2006.

[57] R Gupta and WA Weimer. High enhancement factor gold films for surface enhanced raman spectroscopy. *Chemical physics letters*, 374(3):302–306, 2003.

[58] Osamu Goto, Shigetaka Tomiya, Yosuke Murakami, Akira Shinozaki, Akira Toda, Jiro Kasahara, and Daisuke Hobara. Organic single-crystal arrays from solution-phase growth using micropattern with nucleation control region. *Advanced Materials*, 24(8):1117–1122, 2012.

[59] Zhenguo Chi, Xiqi Zhang, Bingjia Xu, Xie Zhou, Chunping Ma, Yi Zhang, Siwei Liu, and Jiarui Xu. Recent advances in organic mechanofluorochromic materials. *Chemical Society Reviews*, 41(10):3878–3896, 2012.

[60] Taekyung Yu, Byungkwon Lim, and Younan Xia. Aqueous-phase synthesis of single-crystal ceria nanosheets. *Angewandte Chemie International Edition*, 49(26):4484–4487, 2010.

[61] Hanying Li, Benjamin CK Tee, Judy J Cha, Yi Cui, Jong Won Chung, Sang Yoon Lee, and Zhenan Bao. High-mobility field-effect transistors from large-area solution-grown aligned c60 single crystals. *Journal of the American Chemical Society*, 134(5):2760–2765, 2012.

[62] Hanying Li, Benjamin C-K Tee, Gaurav Giri, Jong Won Chung, Sang Yoon Lee, and Zhenan Bao. High-performance transistors and complementary inverters based on solution-grown aligned organic single-crystals. *Advanced Materials*, 24(19):2588–2591, 2012.

[63] LE Scriven. Physics and applications of dip coating and spin coating. In *MRS Proceedings*, volume 121, page 717. Cambridge Univ Press, 1988.

[64] Niranjan Sahu, B Parija, and S Panigrahi. Fundamental understanding and modeling of spin coating process: A review. *Indian Journal of Physics*, 83(4):493–502, 2009.

[65] David B Hall, Patrick Underhill, and John M Torkelson. Spin coating of thin and ultrathin polymer films. *Polymer Engineering & Science*, 38(12):2039–2045, 1998.

[66] Álvaro G Marín, Hanneke Gelderblom, Detlef Lohse, and Jacco H Snoeijer. Order-to-disorder transition in ring-shaped colloidal stains. *Physical review letters*, 107(8):085502, 2011.

[67] Yao Lin, Alexander Böker, Jinbo He, Kevin Sill, Hongqi Xiang, Clarissa Abetz, Xuefa Li, Jin Wang, Todd Emrick, Su Long, et al. Self-directed self-assembly of nanoparticle/copolymer mixtures. *Nature*, 434(7029):55–59, 2005.

[68] David Grosso. How to exploit the full potential of the dip-coating process to better control film formation. *Journal of Materials Chemistry*, 21(43):17033–17038, 2011.

[69] Hongta Yang and Peng Jiang. Large-scale colloidal self-assembly by doctor blade coating. *Langmuir*, 26(16):13173–13182, 2010.

[70] Hector A Becerril, Mark E Roberts, Zihong Liu, Jason Locklin, and Zhenan Bao. High-performance organic thin-film transistors through solution-sheared deposition of small-molecule organic semiconductors. *Advanced Materials*, 20(13):2588–2594, 2008.

[71] Wojciech Pisula, Anoop Menon, Michael Stepputat, Ingo Lieberwirth, Ute Kolb, Adam Tracz, Henning Sirringhaus, Tadeusz Pakula, and Klaus Müllen. A zone-casting technique for device fabrication of field-effect transistors based on discotic hexa-peri-hexabenzocoronene. *Advanced Materials*, 17(6):684–689, 2005.

[72] Shuhong Liu, Wechung Maria Wang, Alejandro L Briseno, Stefan CB Mannsfeld, and Zhenan Bao. Controlled deposition of crystalline organic semiconductors for field-effect-transistor applications. *Advanced Materials*, 21(12):1217–1232, 2009.

[73] Chun-Yu Chen, Hao-Wen Chang, Yu-Fan Chang, Bo-Jie Chang, Yuan-Sheng Lin, Pei-Siou Jian, Han-Cheng Yeh, Hung-Ta Chien, En-Chen Chen, Yu-Chiang Chao, et al. Continuous blade coating for multi-layer large-area organic light-emitting diode and solar cell. *Journal of Applied Physics*, 110(9):094501, 2011.

[74] Roar R Søndergaard, Markus Hösel, and Frederik C Krebs. Roll-to-roll fabrication of large area functional organic materials. *Journal of Polymer Science Part B: Polymer Physics*, 51(1):16–34, 2013.

[75] Yulia Galagan, Ike G de Vries, Arjan P Langen, Ronn Andriessen, Wiljan JH Verhees, Sjoerd C Veenstra, and Jan M Kroon. Technology development for roll-to-roll production of organic photovoltaics. *Chemical Engineering and Processing: Process Intensification*, 50(5):454–461, 2011.

[76] Ying Diao, Benjamin CK Tee, Gaurav Giri, Jie Xu, Do Hwan Kim, Hector A Becerril, Randall M Stoltenberg, Tae Hoon Lee, Gi Xue, Stefan CB Mannsfeld, et al. Solution coating of large-area organic semiconductor thin films with aligned single-crystalline domains. *Nature materials*, 12(7):665–671, 2013.

[77] Ossama Assad, Alexander M Leshansky, Bin Wang, Thomas Stelzner, Silke Christiansen, and Hossam Haick. Spray-coating route for highly aligned and large-scale arrays of nanowires. *ACS nano*, 6(6):4702–4712, 2012.

[78] Nga P Pham, Joachim N Burghartz, and Pasqualina M Sarro. Spray coating of photoresist for pattern transfer on high topography surfaces. *Journal of Micromechanics and Microengineering*, 15(4):691, 2005.

[79] Harminder Singh, TS Sidhu, and SBS Kalsi. Cold spray technology: future of coating deposition processes. *Fracture and Structural Integrity*, 28(22):69–84, 2012.

[80] Tatsuya Shimoda, Katsuyuki Morii, Shunichi Seki, and Hiroshi Kiguchi. Inkjet printing of light-emitting polymer displays. *MRS bulletin*, 28(11):821–827, 2003.

[81] Takeo Kawase, Soichi Moriya, Christopher J Newsome, and Tatsuya Shimoda. Inkjet printing of polymeric field-effect transistors and its applications. *Japanese journal of applied physics*, 44(6R):3649, 2005.

[82] Claudia N Hoth, Pavel Schilinsky, Stelios A Choulis, and Christoph J Brabec. Printing highly efficient organic solar cells. *Nano Letters*, 8(9):2806–2813, 2008.

[83] Thomas Boland, Tao Xu, Brook Damon, and Xiaofeng Cui. Application of inkjet printing to tissue engineering. *Biotechnology journal*, 1(9):910–917, 2006.

[84] Berend-Jan De Gans and Ulrich S Schubert. Inkjet printing of well-defined polymer dots and arrays. *Langmuir*, 20(18):7789–7793, 2004.

[85] Zijian Zheng, Keng-Hoong Yim, Mohammad SM Saifullah, Mark E Welland, Richard H Friend, Ji-Seon Kim, and Wilhelm TS Huck. Uniaxial alignment of liquid-crystalline conjugated polymers by nanoconfinement. *Nano letters*, 7(4):987–992, 2007.

[86] Matthew A Meitl, Zheng-Tao Zhu, Vipan Kumar, Keon Jae Lee, Xue Feng, Yonggang Y Huang, Ilesanmi Adesida, Ralph G Nuzzo, and John A Rogers. Transfer printing by kinetic control of adhesion to an elastomeric stamp. *Nature Materials*, 5(1):33–38, 2006.

[87] Shuguang Zhang. Molecular self-assembly: Another brick in the wall. *Nature nanotechnology*, 1(3):169–170, 2006.

[88] Bong Hoon Kim, Dong Ok Shin, Seong-Jun Jeong, Chong Min Koo, Sang Chul Jeon, Wook Jung Hwang, Sumi Lee, Moon Gyu Lee, and Sang Ouk Kim. Hierarchical self-assembly of block copolymers for lithography-free nanopatterning. *Advanced Materials*, 20(12):2303–2307, 2008.

[89] Paul J Ackerman, Jao van de Lagemaat, and Ivan I Smalyukh. Self-assembly and electrostriction of arrays and chains of hopfion particles in chiral liquid crystals. *Nature communications*, 6, 2015.

[90] Michael Strong. Protein nanomachines. *PLoS biology*, 2(3):e73, 2004.

[91] Bartosz A Grzybowski, Christopher E Wilmer, Jiwon Kim, Kevin P Browne, and Kyle JM Bishop. Self-assembly: from crystals to cells. *Soft Matter*, 5(6):1110–1128, 2009.

[92] Anna M Hiszpanski and Yueh-Lin Loo. Directing the film structure of organic semiconductors via post-deposition processing for transistor and solar cell applications. *Energy & Environmental Science*, 7(2):592–608, 2014.

[93] Ajay A Virkar, Stefan Mannsfeld, Zhenan Bao, and Natalie Stingelin. Organic semiconductor growth and morphology considerations for organic thin-film transistors. *Advanced Materials*, 22(34):3857–3875, 2010.

[94] George M Whitesides and Bartosz Grzybowski. Self-assembly at all scales. *Science*, 295(5564):2418–2421, 2002.

[95] Marek Grzelczak, Jan Vermant, Eric M Furst, and Luis M Liz-Marzán. Directed self-assembly of nanoparticles. *ACS nano*, 4(7):3591–3605, 2010.

[96] Wikipedia. Evaporation — wikipedia, the free encyclopedia, 2015. [Online; accessed 31-March-2015].

[97] Sun Choi, Stefano Stassi, Albert P Pisano, and Tarek I Zohdi. Coffee-ring effect-based three dimensional patterning of micro/nanoparticle assembly with a single droplet. *Langmuir*, 26(14):11690–11698, 2010.

[98] Hua Hu and Ronald G Larson. Evaporation of a sessile droplet on a substrate. *The Journal of Physical Chemistry B*, 106(6):1334–1344, 2002.

[99] Robert D Deegan, Olgica Bakajin, Todd F Dupont, Greg Huber, Sidney R Nagel, and Thomas A Witten. Contact line deposits in an evaporating drop. *Physical review E*, 62(1):756, 2000.

[100] J Ross Moffat, Khellil Sefiane, and Martin ER Shanahan. Effect of tio2 nanoparticles on contact line stick- slip behavior of volatile drops. *The Journal of Physical Chemistry B*, 113(26):8860–8866, 2009.

[101] RG Picknett and R Bexon. The evaporation of sessile or pendant drops in still air. *Journal of Colloid and Interface Science*, 61(2):336–350, 1977.

[102] R Alsan Meric and H Yildirim Erbil. Evaporation of sessile drops on solid surfaces: Pseudospherical cap geometry. *Langmuir*, 14(7):1915–1920, 1998.

[103] Nikolaĭ Nikolaevich Lebedev. *Special functions and their applications*. Courier Corporation, 1972.

[104] Meysam R Barmi and Carl D Meinhart. Convective flows in evaporating sessile droplets. *The Journal of Physical Chemistry B*, 118(9):2414–2421, 2014.

[105] Jianguo Zhang, Frédéric Leroy, and Florian Müller-Plathe. Influence of contact-line curvature on the evaporation of nanodroplets from solid substrates. *Physical review letters*, 113(4):046101, 2014.

[106] CV Sternling and LE Scriven. Interfacial turbulence: hydrodynamic instability and the marangoni effect. *AIChE Journal*, 5(4):514–523, 1959.

[107] LE Scriven and CV Sternling. The marangoni effects. *Nature*, pages 186–188, 1960.

[108] Hua Hu and Ronald G Larson. Marangoni effect reverses coffee-ring depositions. *The Journal of Physical Chemistry B*, 110(14):7090–7094, 2006.

[109] Anne-Marie Cazabat and Geoffroy Guéna. Evaporation of macroscopic sessile droplets. *Soft Matter*, 6(12):2591–2612, 2010.

[110] Hua Hu and Ronald G Larson. Analysis of the microfluid flow in an evaporating sessile droplet. *Langmuir*, 21(9):3963–3971, 2005.

[111] Tim Still, Peter J Yunker, and Arjun G Yodh. Surfactant-induced marangoni eddies alter the coffee-rings of evaporating colloidal drops. *Langmuir*, 28(11):4984–4988, 2012.

[112] Michael FL De Volder, Sameh H Tawfick, Ray H Baughman, and A John Hart. Carbon nanotubes: present and future commercial applications. *Science*, 339(6119):535–539, 2013.

[113] Liangbing Hu, David S Hecht, and George Gruner. Carbon nanotube thin films: fabrication, properties, and applications. *Chemical Reviews*, 110(10):5790–5844, 2010.

[114] Larry Lüer, Sajjad Hoseinkhani, Dario Polli, Jared Crochet, Tobias Hertel, and Guglielmo Lanzani. Size and mobility of excitons in (6, 5) carbon nanotubes. *Nature physics*, 5(1):54–58, 2009.

[115] JD Parsons. Nematic ordering in a system of rods. *Physical Review A*, 19(3):1225, 1979.

[116] Jürgen Küpfer and Heino Finkelmann. Nematic liquid single crystal elastomers. *Die Makromolekulare Chemie, Rapid Communications*, 12(12):717–726, 1991.

[117] Lars Onsager. The effects of shape on the interaction of colloidal particles. *Annals of the New York Academy of Sciences*, 51(4):627–659, 1949.

[118] Wenhui Song, Ian A Kinloch, and Alan H Windle. Nematic liquid crystallinity of multiwall carbon nanotubes. *Science*, 302(5649):1363–1363, 2003.

[119] Wilhelm Maier and Alfred Saupe. Eine einfache molekulare theorie des nematischen kristallinflüssigen zustandes. *Zeitschrift Naturforschung Teil A*, 13:564, 1958.

[120] Mathias Steiner, Michael Engel, Yu-Ming Lin, Yanqing Wu, Keith Jenkins, Damon B Farmer, Jefford J Humes, Nathan L Yoder, Jung-Woo T Seo, Alexander A Green, et al. High-frequency performance of scaled carbon nanotube array field-effect transistors. *Applied Physics Letters*, 101(5):053123, 2012.

[121] Aravind Vijayaraghavan, Frank Hennrich, Ninette Sturzl, Michael Engel, Marc Ganzhorn, Matti Oron-Carl, Christoph W Marquardt, Simone Dehm, Sergei Lebedkin, Manfred M Kappes, et al. Toward single-chirality carbon nanotube device arrays. *ACS nano*, 4(5):2748–2754, 2010.

[122] Leonid Shmuylovich, Amy Q Shen, and Howard A Stone. Surface morphology of drying latex films: multiple ring formation. *Langmuir*, 18(9):3441–3445, 2002.

[123] Suck Won Hong, Supratim Giri, Victor S-Y Lin, and Zhiqun Lin. Simple route to gradient concentric metal and metal oxide rings. *Chemistry of materials*, 18(22):5164–5166, 2006.

[124] MER Shanahan and K Sefiane. Kinetics of triple line motion during evaporation. *Contact angle, wettability and adhesion*, 6:19–31, 2009.

[125] Hugues Bodiguel, Frédéric Doumenc, and Béatrice Guerrier. Stick- slip patterning at low capillary numbers for an evaporating colloidal suspension. *Langmuir*, 26(13):10758–10763, 2010.

[126] Peter Atkins and Julio De Paula. *Elements of physical chemistry*. Oxford University Press, 2013.

[127] Hans-Jürgen Butt, Karlheinz Graf, and Michael Kappl. *Physics and chemistry of interfaces*. John Wiley & Sons, 2006.

[128] Oscar Giraldo, Jason P Durand, Harikrishnan Ramanan, Kate Laubernds, Steven L Suib, Michael Tsapatsis, Stephanie L Brock, and Manuel Marquez. Dynamic organization of inorganic nanoparticles into periodic micrometer-scale patterns. *Angewandte Chemie*, 115(25):3011–3015, 2003.

[129] Han Li, Tilman C Hain, Andreas Muzha, Friedrich Schöppler, and Tobias Hertel. Dynamical contact line pinning and zipping during carbon nanotube coffee stain formation. *ACS nano*, 8(6):6417–6424, 2014.

[130] Vijoya Sa and Konstantin G Kornev. Analysis of stability of nanotube dispersions using surface tension isotherms. *Langmuir*, 27(22):13451–13460, 2011.

[131] Friedrich Schöppler, Christoph Mann, Tilman C Hain, Felix M Neubauer, Giulia Privitera, Francesco Bonaccorso, Daping Chu, Andrea C Ferrari, and Tobias Hertel. Molar extinction coefficient of single-wall carbon nanotubes. *The Journal of Physical Chemistry C*, 115(30):14682–14686, 2011.

[132] Jun Xu, Jianfeng Xia, Suck Won Hong, Zhiqun Lin, Feng Qiu, and Yuliang Yang. Self-assembly of gradient concentric rings via solvent evaporation from a capillary bridge. *Physical review letters*, 96(6):066104, 2006.

[133] Peter J Yunker, Tim Still, Matthew A Lohr, and AG Yodh. Suppression of the coffee-ring effect by shape-dependent capillary interactions. *Nature*, 476(7360):308–311, 2011.

[134] Michael S Arnold, Jin Suntivich, Samuel I Stupp, and Mark C Hersam. Hydrodynamic characterization of surfactant encapsulated carbon nanotubes using an analytical ultracentrifuge. *ACS nano*, 2(11):2291–2300, 2008.

[135] Tobias Hertel, Sabine Himmelein, Thomas Ackermann, Dominik Stich, and Jared Crochet. Diffusion limited photoluminescence quantum yields in 1-d semiconductors: single-wall carbon nanotubes. *ACS nano*, 4(12):7161–7168, 2010.

[136] Melburne C LeMieux, Mark Roberts, Soumendra Barman, Yong Wan Jin, Jong Min Kim, and Zhenan Bao. Self-sorted, aligned nanotube networks for thin-film transistors. *Science*, 321(5885):101–104, 2008.

[137] Christian Dorrer and Jürgen Rühe. Advancing and receding motion of droplets on ultrahydrophobic post surfaces. *Langmuir*, 22(18):7652–7657, 2006.

[138] Wonjae Choi, Anish Tuteja, Joseph M Mabry, Robert E Cohen, and Gareth H McKinley. A modified cassie–baxter relationship to explain contact angle hysteresis and anisotropy on non-wetting textured surfaces. *Journal of colloid and interface science*, 339(1):208–216, 2009.

[139] Adam T Paxson and Kripa K Varanasi. Self-similarity of contact line depinning from textured surfaces. *Nature communications*, 4:1492, 2013.

[140] Yuri S Kivshar. Creation of nonlinear localized modes in discrete lattices. *Physical Review E*, 48(5):4132, 1993.

[141] Yuri S Kivshar and David K Campbell. Peierls-nabarro potential barrier for highly localized nonlinear modes. *Physical Review E*, 48(4):3077, 1993.

[142] AV Savin, GP Tsironis, and AV Zolotaryuk. Reversal effects in stochastic kink dynamics. *Physical Review E*, 56(3):2457, 1997.

[143] NK Adam and HK Livingston. Contact angles and work of adhesion. *Nature*, 1958.

[144] ABD Cassie. Contact angles. *Discuss. Faraday Soc.*, 3:11–16, 1948.

[145] E Matijević and BA Pethica. The properties of ionized monolayers. part 1.—sodium dodecyl sulphate at the air/water interface. *Transactions of the Faraday Society*, 54:1382–1389, 1958.

[146] Boualem Hammouda. Temperature effect on the nanostructure of sds micelles in water. *J. Res. Natl. Inst. Stand. Technol*, 118:151–167, 2013.

[147] Musa Kaleem Baloch, G Hameed, and A Bano. Effect of electrolyte concentration and temperature on cmc of surfactants. *Journal of the Chemical Society of Pakistan*, 24(2):77–86, 2002.

[148] Teresa M. Barnes, Jeffrey L. Blackburn, Jao van de Lagemaat, Timothy J. Coutts, and Michael J. Heben. Reversibility, dopant desorption, and tunneling in the temperature-dependent conductivity of type-separated, conductive carbon nanotube networks. *ACS Nano*, 2(9):1968–1976, 2008.

[149] Timothy J McDonald, Chaiwat Engtrakul, Marcus Jones, Garry Rumbles, and Michael J Heben. Kinetics of pl quenching during single-walled carbon nanotube rebundling and diameter-dependent surfactant interactions. *The Journal of Physical Chemistry B*, 110(50):25339–25346, 2006.

[150] Jeong-Yuan Hwang, Adrian Nish, James Doig, Sigrid Douven, Chun-Wei Chen, Li-Chyong Chen, and Robin J Nicholas. Polymer structure

and solvent effects on the selective dispersion of single-walled carbon nanotubes. *Journal of the American Chemical Society*, 130(11):3543–3553, 2008.

[151] Dimitri Janssen, Randy De Palma, Stijn Verlaak, Paul Heremans, and Wim Dehaen. Static solvent contact angle measurements, surface free energy and wettability determination of various self-assembled monolayers on silicon dioxide. *Thin Solid Films*, 515(4):1433–1438, 2006.

[152] Álvaro G Marín, Hanneke Gelderblom, Detlef Lohse, and Jacco H Snoeijer. Rush-hour in evaporating coffee drops. *Physics of Fluids*, 23(9):1111, 2011.

[153] Phaedon Avouris, Marcus Freitag, and Vasili Perebeinos. Carbon-nanotube photonics and optoelectronics. *Nature photonics*, 2(6):341–350, 2008.

[154] Brian J Landi, Ryne P Raffaelle, Stephanie L Castro, and Sheila G Bailey. Single-wall carbon nanotube–polymer solar cells. *Progress in photovoltaics: research and applications*, 13(2):165–172, 2005.

[155] J Frenkel. On the transformation of light into heat in solids. i. *Physical Review*, 37(1):17, 1931.

[156] Gregory H Wannier. The structure of electronic excitation levels in insulating crystals. *Physical Review*, 52(3):191, 1937.

[157] R Bruce Weisman and Sergei M Bachilo. Dependence of optical transition energies on structure for single-walled carbon nanotubes in aqueous suspension: an empirical kataura plot. *Nano Letters*, 3(9):1235–1238, 2003.

[158] Mildred S Dresselhaus, Gene Dresselhaus, Riichiro Saito, and Ado Jorio. Exciton photophysics of carbon nanotubes. *Annu. Rev. Phys. Chem.*, 58:719–747, 2007.

[159] Michael J O'connell, Sergei M Bachilo, Chad B Huffman, Valerie C Moore, Michael S Strano, Erik H Haroz, Kristy L Rialon, Peter J Boul, William H Noon, Carter Kittrell, et al. Band gap fluorescence from individual single-walled carbon nanotubes. *Science*, 297(5581):593–596, 2002.

[160] Gregory D Scholes and Garry Rumbles. Excitons in nanoscale systems. *Nature materials*, 5(9):683–696, 2006.

[161] Y Oyama, R Saito, K Sato, J Jiang, Ge G Samsonidze, A Grüneis, Y Miyauchi, S Maruyama, A Jorio, G Dresselhaus, et al. Photoluminescence intensity of single-wall carbon nanotubes. *Carbon*, 44(5):873–879, 2006.

[162] PH Tan, AG Rozhin, T Hasan, P Hu, V Scardaci, WI Milne, and AC Ferrari. Photoluminescence spectroscopy of carbon nanotube bundles: Evidence for exciton energy transfer. *Physical review letters*, 99(13):137402, 2007.

[163] Fuming Chen, Bo Wang, Yuan Chen, and Lain-Jong Li. Toward the extraction of single species of single-walled carbon nanotubes using fluorene-based polymers. *Nano letters*, 7(10):3013–3017, 2007.

[164] IB Mortimer and RJ Nicholas. Role of bright and dark excitons in the temperature-dependent photoluminescence of carbon nanotubes. *Physical review letters*, 98(2):027404, 2007.

[165] Ryusuke Matsunaga, Kazunari Matsuda, and Yoshihiko Kanemitsu. Observation of charged excitons in hole-doped carbon nanotubes using photoluminescence and absorption spectroscopy. *Physical review letters*, 106(3):037404, 2011.

[166] Catalin D Spataru, Sohrab Ismail-Beigi, Lorin X Benedict, and Steven G Louie. Excitonic effects and optical spectra of single-walled carbon nanotubes. *Physical Review Letters*, 92(7):077402, 2004.

[167] Maksim Grechko, Yumin Ye, Randy D Mehlenbacher, Thomas J McDonough, Meng-Yin Wu, Robert M Jacobberger, Michael S Arnold, and Martin T Zanni. Diffusion-assisted photoexcitation transfer in coupled semiconducting carbon nanotube thin films. *ACS nano*, 8(6):5383–5394, 2014.

[168] Huihong Qian, Carsten Georgi, Neil Anderson, Alexander A Green, Mark C Hersam, Lukas Novotny, and Achim Hartschuh. Exciton energy transfer in pairs of single-walled carbon nanotubes. *Nano letters*, 8(5):1363–1367, 2008.

[169] Jared J Crochet, Jay D Sau, Juan G Duque, Stephen K Doorn, and Marvin L Cohen. Electrodynamic and excitonic intertube interactions in semiconducting carbon nanotube aggregates. *ACS nano*, 5(4):2611–2618, 2011.

[170] Anni J Siitonen, Dmitri A Tsyboulski, Sergei M Bachilo, and R Bruce Weisman. Surfactant-dependent exciton mobility in single-walled carbon nanotubes studied by single-molecule reactions. *Nano letters*, 10(5):1595–1599, 2010.

[171] S Moritsubo, T Murai, T Shimada, Y Murakami, S Chiashi, S Maruyama, and YK Kato. Exciton diffusion in air-suspended single-walled carbon nanotubes. *Physical review letters*, 104(24):247402, 2010.

[172] Peter Peumans, Aharon Yakimov, and Stephen R Forrest. Small molecular weight organic thin-film photodetectors and solar cells. *Journal of Applied Physics*, 93(7):3693–3723, 2003.

[173] Denis E Markov, Emiel Amsterdam, Paul WM Blom, Alexander B Sieval, and Jan C Hummelen. Accurate measurement of the exciton diffusion length in a conjugated polymer using a heterostructure with a side-chain cross-linked fullerene layer. *The Journal of Physical Chemistry A*, 109(24):5266–5274, 2005.

[174] Omar N Torrens, Ming Zheng, and James M Kikkawa. Energy of k-momentum dark excitons in carbon nanotubes by optical spectroscopy. *Physical review letters*, 101(15):157401, 2008.

[175] Yoichi Murakami, Benjamin Lu, Said Kazaoui, Nobutsugu Minami, Tatsuya Okubo, and Shigeo Maruyama. Photoluminescence sidebands of carbon nanotubes below the bright singlet excitonic levels. *Physical Review B*, 79(19):195407, 2009.

[176] Vasili Perebeinos, J Tersoff, and Phaedon Avouris. Effect of exciton-phonon coupling in the calculated optical absorption of carbon nanotubes. *Physical review letters*, 94(2):027402, 2005.

[177] Yuhei Miyauchi and Shigeo Maruyama. Identification of an excitonic phonon sideband by photoluminescence spectroscopy of single-walled carbon-13 nanotubes. *Physical Review B*, 74(3):035415, 2006.

[178] J Lefebvre and Paul Finnie. Polarized photoluminescence excitation spectroscopy of single-walled carbon nanotubes. *Physical review letters*, 98(16):167406, 2007.

[179] Yoichi Murakami, Erik Einarsson, Tadao Edamura, and Shigeo Maruyama. Polarization dependence of the optical absorption of single-walled carbon nanotubes. *Physical review letters*, 94(8):087402, 2005.

# List of Figures

# List of Tables

# 9 Acknowledgments

There are many people who provided invaluable contributions to the work presented in this dissertation. First and foremost, I am very grateful to my supervisor Prof. Dr. **Tobias Hertel** for his support, inspiration and giving me the sufficient freedom to choose the research direction and explore my own ideas. His constant guidance and encouragement, from the profound and theoretical thinking on the research to the small and practical techniques in writing and drawing, are the most valuable harvesting during the years of my PhD.

I want to thank Dr. **Friedrich Schöppler** who has been a friend, a counselor and a collaborator. Results presented in this thesis would not have been possible without the numerously day-after-day discussion with him on almost every aspect of the research. Things were always easier and clearer after talking with him. Beyond the scientific research, many of his advice helped me adapt to the PhD life smoothly. I am deeply grateful for that.

The early discussion with **Andreas Muzha** provided a very good beginning of this work. Both **Andreas Muzha** and Dr. **Vladimir Stepanenko** from Prof. Würthner's group offered very kind help on the early training of SEM. During my first year in the group, I was lucky to work with Dr. **Kristin Kröker** on an interesting project about the interaction between cells and SWNT-DNA conjugates. I have learned lots of basics from her whose logical and mindful thoughts still show me an excellent model of research.

For the experiments of fluorescence microscopy and spectroscopy in this work, I really appreciate the help from Dr. **Tilman Hain** whose sophisticated experimental setup strongly facilitated the process of this project. His insightful suggestions on programming also benefited me a lot in my skills of IGOR and LaTeX.

I would like to thank Dr. **Timo Hefner** for the guidance of absorption spectroscopy, **Matthias Kastner** for the assistance of the CVD setup, **Felix Bergler** for the instruction of photolithography technique and the optical microscope, Dr. **Frank Brunecker** for the introduction of AFM and the tour of Labs during the first day I came.

In the past four years, my friendly and passionate colleagues make for a

great working atmosphere. It is my honor to share the offices with **Jinbo Pang**, **Thomas Stocker**, Dr. **Florian Späth**, Dr. **Nicolas Rühl** and **Imge Namal**. I will cherish these memories for the rest of my life. For Dr. **Holger Hartleb**, Dr. **Daniel Schilling**, Dr. **Christopher Mann** and **Sabine Stahl**, the bier we drank and the talk we had together will never fade away in my mind.

The experimental setup to some extent determines the quality and efficiency of the work. In that sense, I appreciate the contributions from all the technicians **Reiner Eck, Jürgen Zimmermann, Ralf Kohrmann, Wolfgang Liebler, Katharina Schreckling, Gerhard Bömmel** and **Peter Lang**. Their support on the heating setup, camera and other electronic devices strongly facilitated the research.

Also, I would like to thank **Sabine Walther** for all of the trivial but necessary paperworks about registrations, conferences and applications. I am thankful to **Belinda Böhm** for the assistance of experimental tools and **Sabine Fuchs** for the laser safety training. I especially appreciate the constant help from **Sabine Stahl** who acted as a problem solver and patient tutor offering lots of basic training and experimental materials. Further, I want thank all of the Bachelor and Master students who once worked with me on the projects of their practical training. Amongst them, **Klaus Eckstein**, **Melanie Achsnich** and **Kerstin Müller** as the new generation in Hertel's group have my best wishes for future success.

I acknowledge the scholarship granted by the China Scholarship Council. Without this financial supporting I cannot finish this work.

At last I am deeply indebted to my parents in China for their never ending support and encouragement that let me smile at each setback and difficulty in life and study over the last years. My wife, **Xuan Wang** was accompanying me when I wrote every word in this thesis. As a friend, a partner and a mentor, she endows me extraordinary enthusiasm and makes my life meaningful. This thesis is dedicated to her.